A 3-in-1 Approach to Evaluate Gas Hydrate Inhibitors

Une approche 3-en-1 pour évaluer les inhibiteurs d'hydrates gazeux

A Thesis Submitted to the Division of Graduate Studies
of the Royal Military College of Canada
by

Narendra Kumar

In partial fulfillment of the requirements of the degree of
Master of Applied Science in Chemical Engineering

August, 2016

Acknowledgement

First and foremost, I would like to express my sincere gratitude to my advisor Dr. Juan Beltran, for his continuous support, guidance, and motivation through the development of this work. I greatly appreciate the help provided by RMC Chemistry and Chemical Engineering Department. I am thankful to the past and present members of the RMC hydrate group. Finally, I express my profound gratitude to my parents, brothers and my fiancée for providing me with unfailing support and continuous encouragement.

Abstract

A novel method to screen crystal morphology, thermodynamics, and kinetic effects of gas hydrate inhibitors is presented. This method allowed tight control of the temperature at the crystallization surface irrespective of ambient conditions. New insights into the mechanisms of methane hydrate formation and dissociation in the presence of thermodynamic inhibitors (monoethylene glycol, sodium chloride), a kinetic inhibitor (polyvinylpyrrolidone) (PVP), and an antiagglomerant (tertbutylammoniumbromide) (TBAB) are provided. The methane hydrate formation/decomposition was investigated on a uniform temperature surface and a constant temperature gradient surface. Temperature-gradients were used to relate the hydrate morphology and growth rate to the driving force. The hydrate morphology and crystal growth behavior were found to vary significantly due to the presence of additives. The hydrate formed in the presence of PVP and TBAB were more stable than those formed with pure water. All of the systems studied showed hydrate propagation onto the sapphire surface outside the original water boundary. The presence of NaCl, EG, PVP, and TBAB significantly reduced the hydrate growth rate, however, massive hydrates were formed with TBAB at higher subcoolings. Hydrate phase equilibria were also studied. The presence of PVP and TBAB had no impact on methane hydrate phase equilibria at the concentrations used. Compared to traditional multi-trial methods, the main advantage of this method is that only a single experiment is required to (1) correlate the crystal growth behavior and hydrate morphology with respect to temperature, (2) the H-L-V equilibrium temperature at the experimental pressure, and (3) the change in hydrate growth velocity with respect to temperature. Thus, this novel 3-in-1 Approach effectively allows the assessment of crystal morphology, apparent kinetics and phase equilibria of gas hydrates in the presence of hydrate inhibitors.

Résumé

Une nouvelle méthode capable d'analyser la morphologie des cristaux ainsi que la thermodynamique et les effets cinétiques des inhibiteurs d'hydrates de gaz est présentée. Cette méthode permet un contrôle précis de la température de cristallisation indépendamment des conditions ambiantes. Des nouvelles perspectives sur les mécanismes de formation et de dissociation des hydrates de méthane en présence d'inhibiteurs thermodynamiques (mono éthylène glycol, chlorure de sodium), d'un inhibiteur cinétique (poly-vinylpyrrolidone, PVP) et d'un antiagglomérant (tertbutylammoniumbromide, TBAB) sont présentées. La formation ainsi que la décomposition des hydrates de méthane ont été étudiées sur une surface à température uniforme ainsi sur un gradient de température. Le gradient de température a été utilisé pour établir une corrélation entre la morphologie des hydrates, les taux de croissance et la force d'entrainement. Il a été démontré que le comportement de la morphologie des hydrates et de la croissance des cristaux varie considérablement en raison de la présence d'additifs. Les hydrates formés en présence de PVP et TBAB se sont révélés plus stables que ceux formés à partir de l'eau pure. De plus, tous les systèmes étudiés ont révélé la propagation d'hydrates dans la surface du saphir à l'extérieur du volume d'eau initial. La présence de NaCl, EG, PVP et TBAB a réduit significativement le taux de croissance des hydrates. Cependant, en présence de TBAB et une haute force d'entrainement des hydrates massifs se sont formés. L'équilibre des phases des hydrates a aussi été étudié. La présence de PVP et de TBAB n'a eu aucun impact sur l'équilibre des phases du méthane hydrate aux concentrations utilisées. Comparé aux méthodes traditionnelles de multi-essai, l'avantage principal de cette méthode est que seulement une expérience est requise pour évaluer : (1) la corrélation entre la croissance des cristaux et la morphologie des hydrates par rapport à la température (2) l'équilibre H-L-V de la température à la pression expérimentale (3) Le changement de vitesse dans la croissance des hydrates par rapport à la température. En conclusion, cette approche 3-en-1 permet d'évaluer efficacement la morphologie des cristaux, les propriétés cinétiques.

Contents

List of Tables

List of Figures

Nomenclature

AAs	anti-agglomerants
ΔT_{sub}	degree of subcooling
EG	ethylene glycol
l_{gap}	gap length between the constant temperature plates
r_{f}	hydrate film length
v	hydrate film velocity
H-L-V	hydrate-liquid-vapor
KHIs	kinetic hydrate inhibitors
PVCap	polyvinylcaprolactam
PVP	polyvinylpyrrolidone
x	position
p	pressure
THIs	thermodynamic hydrate inhibitors
TEC	thermoelectric cooler
T	temperature
g	temperature gradient
TBAB	tetra-n-butyl ammonium bromide
t	time

Superscripts/subscripts

I	solid-liquid interface
i,i+1	step i,i+1
exp	experimental value
eq	equilibrium value
sub	subcooling
L	low temperature side of the slide
H	high temperature side of the slide

Chapter 1

Introduction

Gas hydrates are non-stoichiometric, crystalline compounds where guest molecules (e.g., methane, ethane, propane, etc.) are trapped in a hydrogen bonded network formed by water molecules. Under suitable thermodynamic conditions, the crystal structure is stabilized by weak van der Waals forces between the guest molecules and the host cavities (Van der Waals and Platteeuw, 1959). All common natural gas hydrates belong to the three crystalline structures: cubic structure I, cubic structure II, and hexagonal structure H. The size of the guest molecules is the main determining factor for the type of hydrate structure formed. In particular, methane forms structure I hydrates (Sloan, 2003).

Gas hydrates are typically formed under low temperature and elevated pressure conditions (Koh, 2002), such as those encountered in deep-sea gas and oil pipelines (Sloan *et al.*, 2010; Urdahl *et al.*, 1995; Englezos, 1993). In petroleum exploration and production, the formation of gas hydrates can cause plugging of pipelines with subsequent loss of production and possibly safety concerns (Daraboina *et al.*, 2011b; Koh *et al.*, 2011). There is a significant cost (estimated US$220 million annually) associated with preventing plug formation in oil and gas pipelines (Sloan, 2003). Therefore, it is of interest to understand gas hydrates while interacting with different surfaces and additives. Specifically, fundamental studies on growth kinetics, crystal morphology, and thermodynamics of hydrates are necessary to improve current plugging prevention technologies and develop new inhibitor strategies.

Traditionally, gas hydrates are avoided by adding thermodynamic hydrate inhibitors (THIs) such as methanol, mono-ethylene glycol, and sodium chloride to the aqueous phase. These additives shift the hydrate stability zone (Lafond

et al., 2012; Sloan Jr and Koh, 2007; Urdahl *et al.*, 1995) so that hydrates are never formed in pipelines. For low temperature operations, high water cut operations, amounts in excess of 50% by volume of THI's may be required, which can increase the total cost of fossil fuel production significantly (Sloan Jr and Koh, 2007; Perfeldt *et al.*, 2014; Wu *et al.*, 2014). Although the application of THIs prevents hydrate formation, the requirement of large volumes of these additives, possible toxicity, and low recovery fractions have encouraged the development of alternative chemical approaches (Kelland *et al.*, 2006; Wu *et al.*, 2014; Zerpa *et al.*, 2010).

Over the past decade, there has been a transition towards low dosage hydrate inhibitors (LDHIs) ($w_{\text{LDHIs}} = 0.1 - 2\%$ in the aqueous phase) (Davenport *et al.*, 2011; Perfeldt *et al.*, 2014). These chemicals can be divided into two classes, kinetic hydrate inhibitors (KHIs) and anti-agglomerants (AAs). KHIs (e.g., polyvinylpyrrolidone) are generally believed to delay the nucleation and growth of hydrates. AAs (eg., quaternary ammonium salts) on the other hand, do not prevent hydrate formation, but instead restrict the agglomeration of hydrate particles in pipelines (Sloan Jr and Koh, 2007; Kelland *et al.*, 2006).

Various types of reactors have been designed to study the performance of gas hydrate inhibitors. Growth inhibition is often studied by measuring the lateral growth rate of a single tetrahydrofuran (THF) hydrate crystal (Walker *et al.*, 2015; Chua *et al.*, 2012; Larsen *et al.*, 1998) because it can be done at atmospheric pressure. Stirred tank reactors and autoclaves have been widely used to study formation/dissociation kinetics at the macro scale (Englezos *et al.*, 1987; Tohidi *et al.*, 2015; Bergeron *et al.*, 2010; Lederhos *et al.*, 1996), hydrate phase equilibria (Luna-Ortiz *et al.*, 2014; Bruusgaard *et al.*, 2008), and hydrate particle agglomeration (Huo *et al.*, 2001). Some stirred cells are made completely of sapphire (Del Villano and Kelland, 2011) or have windows for visual observations (Jensen *et al.*, 2010). The ball stop rig and rocker rig (Perfeldt *et al.*, 2014; Chua and Kelland, 2013), flow loops (Bishnoi, 2005), pipe wheels (Urdahl *et al.*, 1995) are examples of reactors that have been used to imitate pipeline conditions for measuring hydrate formation/dissociation kinetics, agglomeration of hydrate particles and plug formation. For crystallography and crystal morphology unstirred high pressure vessels have been used (Wu *et al.*, 2013; Beltran and Servio, 2010; Servio and Englezos, 2003).

Although the above mentioned reactors are effective, they are restricted to measuring one or two parameters at one time. DuQuesnay *et al.* (2015) designed a novel reactor which efficiently allowed for the assessment of crystal morphology, apparent kinetics and phase equilibria in a single experiment.

The design offered strict control of the crystallization substrate temperature, regardless of ambient conditions. To date, the use of this method to investigate the performance of hydrate inhibitors has not been explored.

The main objective of this work is to apply the method used by DuQuesnay *et al.* (2015) to systems containing gas hydrate inhibitors. Validation of this method is important since this method was found to cut experimentation time in addition to reducing multi-trial methods to a single experiment with simple methane hydrates (DuQuesnay *et al.*, 2015). Here, new insights into the mechanisms of methane hydrate formation and dissociation in the presence of thermodynamics inhibitors (monoethylene glycol, sodium chloride), a kinetic inhibitor (polyvinylpyrrolidone) and an antiagglomerant (tertbutylammoniumbromide) are presented. The effect of driving force on crystal morphology and apparent growth kinetics is shown. In addition, the phase behavior of methane hydrates in the presence of the above mentioned additives is investigated. Finally, the influence of additives on hydrate propagation onto surfaces is probed.

Chapter 2

Background

Aqueous clathrate hydrates, or gas hydrates, are non-stoichiometric crystalline compounds (Sloan, 2003) composed of approximately 85% water and 15% small volatile molecules (< 0.9 nm) on a molar basis (Freer *et al.*, 2001). When these small volatile molecules or 'guests' come in contact with water at suitable temperatures and pressures, hydrates form (Beltran and Servio, 2010). Clathrates are thermodynamically stable at a temperature close to the freezing point of water and moderate pressure (typically $T < 300$ K and $p > 0.6$ MPa) (Sloan, 2003). These crystals are known to be non-stoichiometric, due to the occurrence of unoccupied cages. Their composition varies with temperature, pressure, and fluid phase composition (Koh and Sloan, 2007). There are more than 100 species, which can combine with water and form gas hydrates (Englezos, 1993), but CH_4, C_2H_6, C_3H_8, H_2S, and CO_2 are most widely observed hydrate forming gas molecules. Naturally occurring gas hydrates in the earth (containing mostly methane) constitute an unconventional energy resource (Makogon, 2010).

2.1 History of gas hydrates

Hydrates were first described early in the nineteenth century by Sir Humphrey Davy (Englezos, 1993), they remained an academic curiosity for almost a century. In the nineteenth century, hydrates research was concerned with identification of hydrate forming chemical species and the thermodynamic conditions of hydrate crystallization (Englezos, 1993). The second period of gas hydrate studies began in 1934, when Hammerschmidt discovered that solid plugs of

natural gas pipelines were not due to ice formation, but a result of hydrate formation from natural gas (Englezos, 1993). As a result, intense research was started on hydrate-forming conditions to find ways to prevent their formation. The third and current phase of gas hydrate research began in 1965, when Makogon showed that natural gas hydrates exist in the earth's crust and represent a significant energy resource (Sloan Jr and Koh, 2007). Since then, the focus of gas hydrate research expanded to techniques to improve the technologies used to locate the natural gas hydrate deposits and recover energy from these gas hydrate deposits. Over 220 natural gas hydrate deposits have been discovered, both on land and off shore, around the world (Makogon *et al.*, 2007).

2.2 Gas hydrate structures

Gas hydrates are solid solutions of a volatile solute (guest) in a host lattice. The empty hydrate lattice formed by hydrogen bonded water molecules is thermodynamically unstable (Englezos, 1993). It is stabilized by inclusion of an appropriate size guest (gas molecules) which does not interfere with the hydrogen bonding of water molecules (Sloan, 2003). A single cavity occupied by a methane molecule is shown in Figure 2.1.

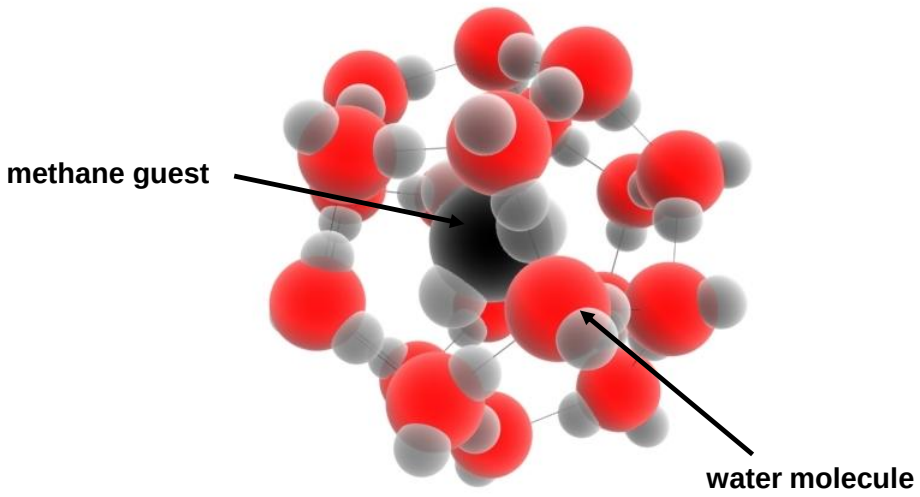

Figure 2.1 – A methane molecule within a cage of hydrogen-bonded water molecule (Beltran, 2009).

All common natural gas hydrates belong to the three crystal structures: cubic structure I (sI), cubic structure II (sII), and hexagonal structure H (sH) (Sloan Jr and Koh, 2007). All three structures consist of about 85% water on a molecular basis (Koh *et al.*, 2011).

A polyhedron with 12 pentagonal faces (5^{12}) is the basic building block for each of the three structures. Structure I gas hydrate is formed when these 5^{12} cavities arrange themselves by linking through their vertices (Englezos, 1993). These dodecahedra cavities are not able to pack together precisely. As a result new polyhedra with twelve pentagonal and two hexagonal faces are created (Englezos, 1993). The structure I unit cell consists of two 5^{12} cavities, plus six large $5^{12}6^2$ cavities (Sloan, 2003) (Figure 2.2). Structure I predominates in natural environments and is formed with molecules having a diameter of 4.2 to 6 Å, such as methane, ethane, and carbon dioxide (Sloan Jr and Koh, 2007). However, a combination of two simple sI hydrate formers, such as a methane-ethane mixture can result in sII hydrate formation depending on the composition and hydrate-forming conditions (Li *et al.*, 2014).

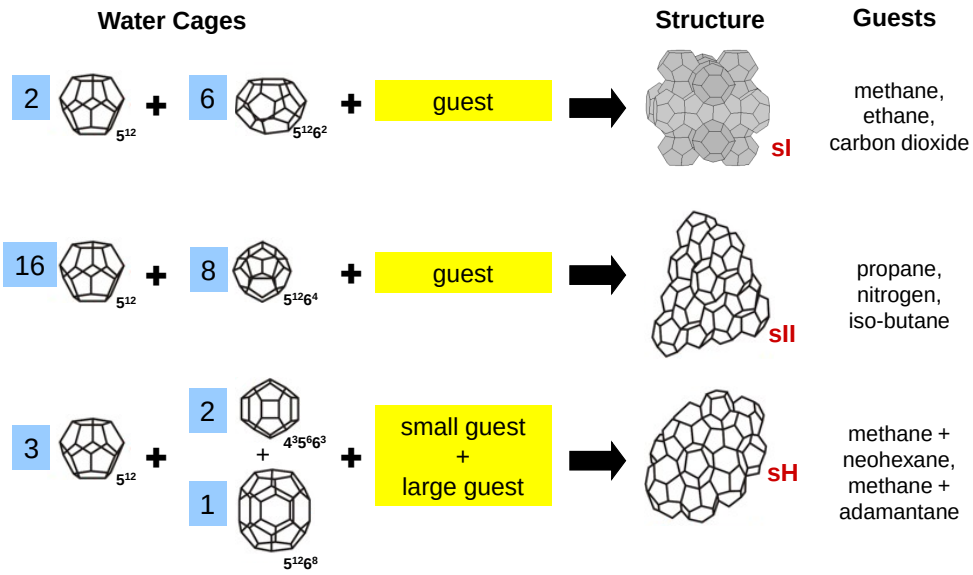

Figure 2.2 – A chart showing three common hydrate structures, and the type of cavities and guests that belong to each structure type (Beltran, 2009).

Structure II gas hydrates are formed when 5^{12} cavities link through their faces. As a result, a large cavity with twelve pentagonal and four hexagonal faces ($5^{12}6^4$) is created (Englezos, 1993). The structure II unit cell consists of

sixteen 5^{12} cavities plus eight $5^{12}6^4$ cavities (Figure 2.2). Structure II mostly occurs in man-made environments and is formed with small guest molecules having diameter < 4.2 Å, and larger molecules from 6 to 7 Å, such as propane and iso-butane (Sloan Jr and Koh, 2007).

Structure H gas hydrates are formed when 5^{12} cavities arrange themselves through face sharing in two dimensions. As a result, $5^{12}6^4$ and $4^3 5^6 6^3$ cavities are created (Sloan, 2003) (Figure 2.2). Structure H can be formed either in man-made or natural environments and it is formed with larger molecules having a diameter of 7 to 9 Å, such as iso-pentane or neo-hexane, accompanied by smaller molecules such as methane, hydrogen sulfide, or nitrogen (Sloan Jr and Koh, 2007).

As the ratio of guest molecules is variable, gas hydrates are also known as non-stoichiometric hydrates (Sloan, 2003; Koh and Sloan, 2007). In simple hydrates, for structure I and structure II, small molecules may fill up both cavities. Sometimes single guests are too large for the smaller cages: while occupying the larger cavity only, leaving the smaller cavity vacant. In contrast to structure I and II, Structure H requires both large and small cavities to be occupied. So, two types of guests are required to form structure H (Sloan Jr and Koh, 2007). Multiple hydrate guests can occupy a hydrate cavity, typically at very high pressures (e.g.; hydrogen in a structure II hydrate) (Sloan Jr and Koh, 2007).

2.3 Physical properties and implications

Gas hydrates may be viewed as a potential source of natural gas, a problem for flow assurance in oil and gas pipelines, as a medium for storage and transportation of natural gas and hydrogen (H_2), and a factor in climate change (Sum *et al.*, 2009; Sloan, 2003). Each of these applications is briefly discussed.

2.3.1 Flow assurance

Gas hydrates are a problem to the oil and gas industries as the conditions in which gas and oil are produced, processed, and transported are frequently suitable for gas hydrate formation (Englezos, 1993). For hydrate formation, four components are required (a) small volatile guest molecule (< 0.9 nm), (b) water in any physical state, (c) high pressure ($p > 0.6$ MPa) and (d) low temperature (typically close to the freezing point of water).

These four components are typically present in natural gas and oil production (Koh *et al.*, 2011). Oil and gas wells always produce undesired water with small hydrocarbons at high pressure. As the flowing fluid mixture cools down, hydrates are formed and plug pipelines. A four-step conceptual mechanism shown in Figure 2.3 for hydrate plug formation in oil-dominated pipelines consists of (1) entrainment of water droplet in the oil phase, (2) growth of hydrate shell on the water droplet at the water-oil interface, (3) agglomeration/deposition of hydrate particle, and (4) complete plugging of pipelines (Sum *et al.*, 2009). It has been estimated that the oil and gas industry spends over US$ 200 M annually to prevent hydrate formation (Sum *et al.*, 2009).

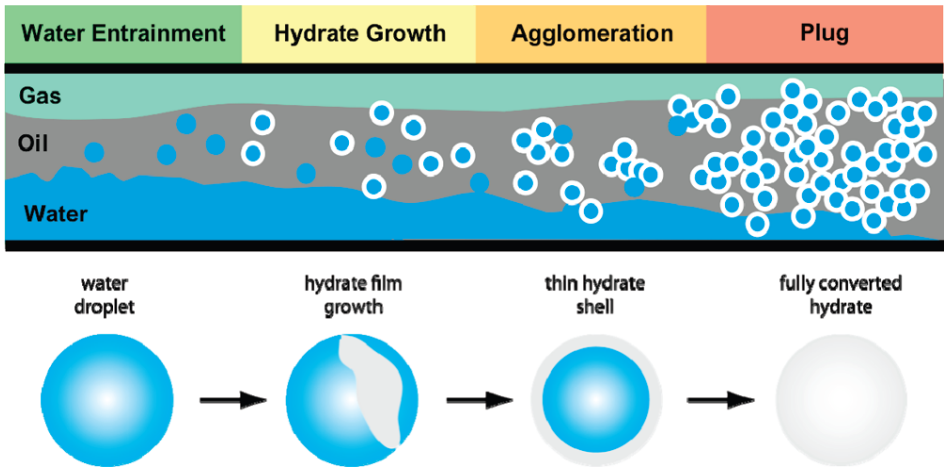

Figure 2.3 – Schematic conceptual depiction of hydrate formation in pipelines in multiphase flow. In addition, conversion of a water droplet into hydrate particle is also shown (Sum *et al.*, 2009).

Traditionally, gas hydrates are avoided by injecting a large quantity of thermodynamic inhibitors such as methanol and glycol. More recently, a new approach has been developed to prevent hydrate formation by injecting low-dosage hydrate inhibitors. These chemicals prevent hydrate formation by delaying nucleation and growth of hydrate crystals, and preventing agglomeration of hydrate particles in flow lines (Kelland *et al.*, 2006).

2.3.2 Energy recovery

Methane hydrates are abundant in oceanic sediment and arctic permafrost locations where both methane and water are present at low temperatures and

high pressures. A large fraction of the earth's fossil fuel energy is stored in gas (mostly methane) hydrate deposits (Koh and Sloan, 2007). Even the most conservative estimates suggest that the amount of energy stored in hydrates is at least twice that of all other fossil fuels combined (Figure 2.4) (Sum *et al.*, 2009; Koh and Sloan, 2007). Therefore, natural gas hydrates could serve as an unconventional source of energy (Makogon, 2010). Over 220 gas hydrate deposits have been found around the world both on land and offshore (Makogon *et al.*, 2007).

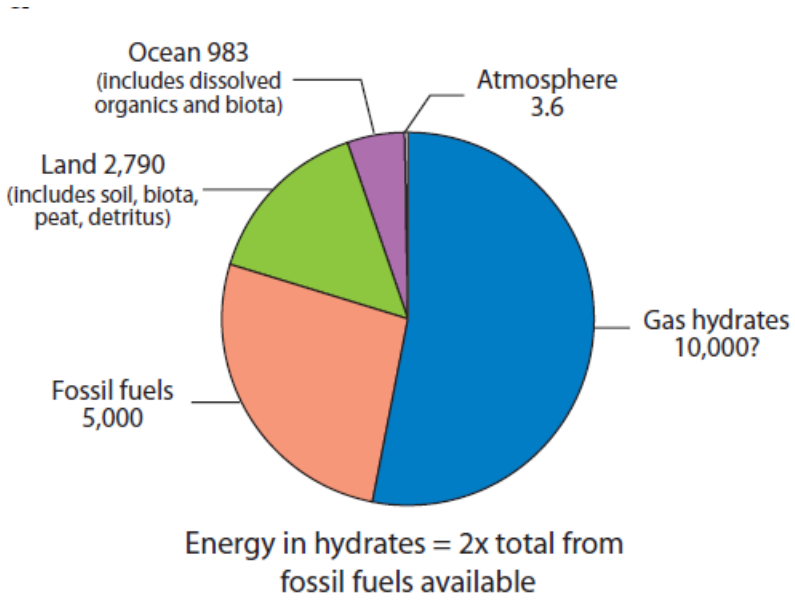

Figure 2.4 – A comparison of energies in conventional hydrocarbons and hydrates. The distribution of organic carbon in Earth reservoirs is shown in gigatons. 1 gigaton = 1.099 trillion m^3, at STP (Koh *et al.*, 2011).

2.3.3 Storage and transportation

Storage and transportation of natural gas as a hydrate is an appealing method, because gas hydrate energy density is comparable to that of highly compressed gas, but less than liquefied natural gas (Sloan Jr and Koh, 2007). Typically one volume of methane hydrate contains 164 volumes of methane at standard temperature and pressure. It has been suggested that it is economically feasible to transport natural gas in hydrate form rather than in liquefied natural

gas tanker, because hydrates require higher temperature and lower pressure conditions than that of compressed and liquefied natural gas (Sloan Jr and Koh, 2007). Hydrogen could be stored in pure hydrogen hydrate at high pressures ($\sim$ 200 MPa), but with a promoter molecule such as tetrahydrofuran pressure could be reduced by one order of magnitude at room temperature (Florusse *et al.*, 2004).

2.3.4 Climate change

Methane is roughly thirty times more potent than carbon dioxide as a greenhouse gas (Englezos, 1993) and it is estimated that more than 3000 Gton of carbon are trapped as natural gas hydrates ($\sim$ 50% of the organic carbon on earth) (Koh *et al.*, 2011). Thus, dissociation of naturally-occurring methane hydrates as a result of warming oceans could have a significant impact on climate change.

Researchers are also investigating the potential of gas hydrates for carbon dioxide sequestration. Carbon dioxide sequestration involves capturing of carbon dioxide from industrial or utility plant streams and removing it from the atmosphere by storing it as a hydrate in the ocean or replacing methane with carbon dioxide during energy recovery from natural gas hydrates (Koh *et al.*, 2011). This sequestration of CO_2 is possible because CO_2 hydrates are thermodynamically more stable than the methane hydrates, and because of this, the simultaneous sequestration of carbon dioxide and the extraction of methane could be feasible (Ota *et al.*, 2007).

2.4 Thermodynamics

Gas hydrate formation is a physical process where the host (water) and guest interact through weak van der Waals type dispersion forces. The temperature and pressure conditions will determine the phase in which host (water) and guest will exist (Holder *et al.*, 1988). Studies of gas hydrate thermodynamics are mainly concerned about measuring the pressure and temperature conditions at which three phases: hydrate, water and gas are all in equilibrium (Holder *et al.*, 1980). A schematic representation of the partial phase diagram for a sub-critical hydrate forming gas is shown in Figure 2.5.

If a pressure vessel containing gas (in excess) and water is compressed at a temperature lower than the upper quadruple point, Q_2, the pressure will even-

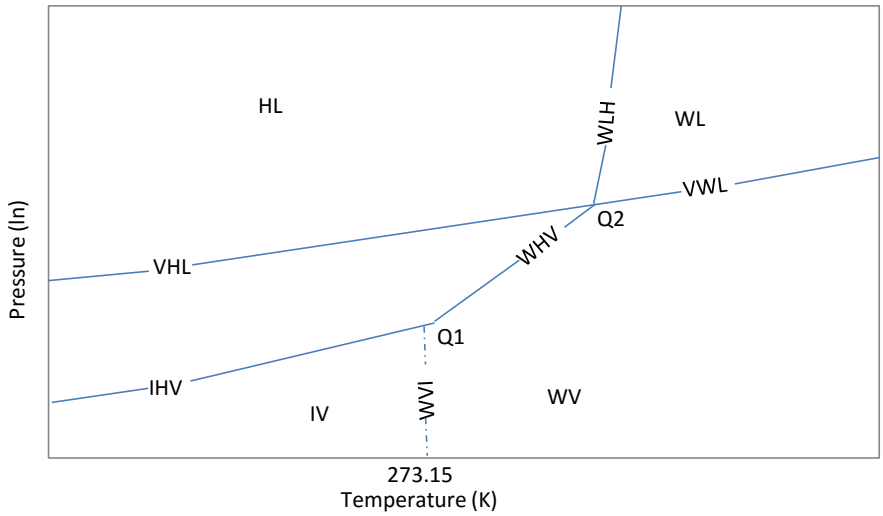

Figure 2.5 – Schematic representation of partial phase diagram for a subcritical hydrate forming gas. Gas in excess. Q_1: lower quadruple point refers to the WVIH, Q_2: upper quadruple point refers to the WVLH, W = water-rich liquid, I = ice, V = vapor, H = hydrate, L = liquid rich in hydrate former. Adapted from (Holder *et al.*, 1988).

tually reach a value where the gas and water will combine to form hydrates. At this pressure and temperature condition, gas water and hydrate phases coexist. If the system is compressed further, more hydrate will form until only two phases remain in the system (Holder *et al.*, 1988). If the two remaining phases are vapor and hydrate, the system can be compressed until the dew point of the vapor is reached. The pressure and temperature conditions where vapor, liquid rich in hydrate former and hydrate coexist, is known as the upper quadruple point. A similar principle applies to the temperature below the freezing point of water except ice replaces the liquid water. In this case, gas does not dissolve in the ice phase. No upper quadruple point exists for methane and nitrogen, due to their low critical temperature (191 K for methane, and 126 K for nitrogen) (Sloan Jr and Koh, 2007).

Gas hydrate phase equilibrium conditions are measured by using a pressurized reactor equipped with windows that allow the direct visual observation of the onset of hydrate formation and dissociation (Holder *et al.*, 1988). These pressurized reactors can be operated in isobaric, isothermal or isochoric modes. In addition to the visual method, on-line pressure measurement can be used to

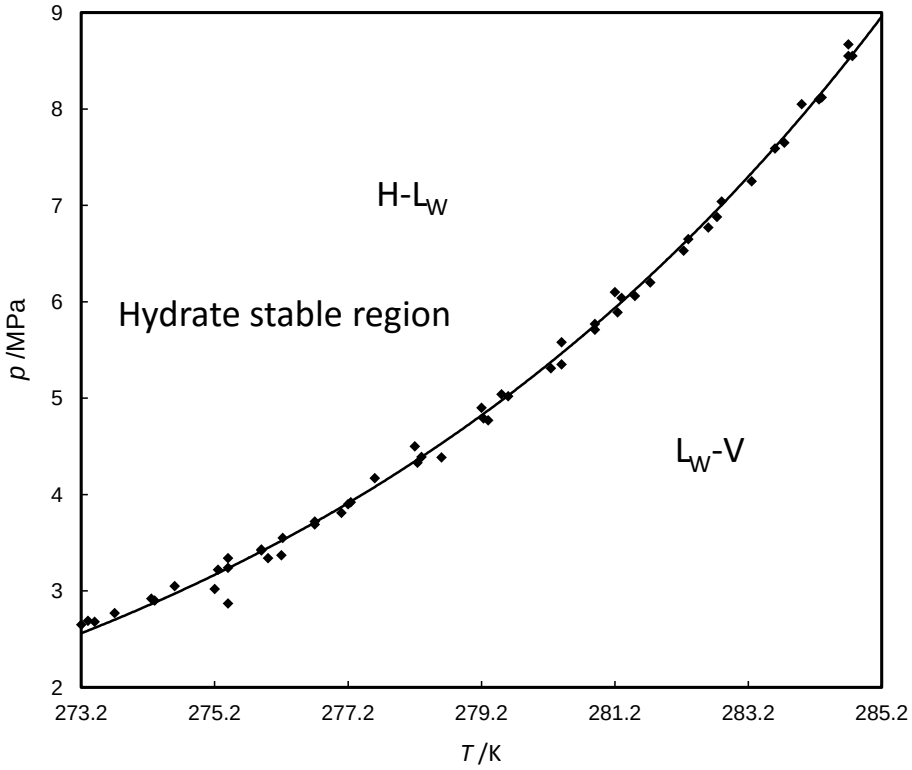

Figure 2.6 – Partial phase diagram for the system methane + water, in the hydrate region (Sloan Jr and Koh, 2007).

detect the onset of hydrate formation and dissociation through the significant change in pressure associated with hydrate formation and dissociation (Holder *et al.*, 1988). Typically, gas hydrates are formed by decreasing the temperature at constant pressure or increasing the pressure at constant temperature beyond the hydrate equilibrium conditions. The hydrates are then dissociated by increasing the temperature at a constant pressure or decreasing the pressure at a constant temperature. A gas hydrate phase equilibrium point can be measured by continuous or step-wise heating to increase the temperature at constant pressure and dissociate the hydrate.

Hydrate formation will occur at conditions well past hydrate equilibrium, due to meta-stability (Sloan Jr and Koh, 2007). However, metastability is observed only for hydrate formation.

A partial phase diagram for the methane + water system, above the freezing

point of water, is shown in Figure 2.6. The pressure and temperature of the HLV (hydrate-liquid-vapor) equilibrium curve mark the limit of hydrate formation. Above the equilibrium curve, hydrate and a liquid aqueous phase coexist while below the HLV equilibrium line vapor and liquid aqueous phase coexist (Sloan Jr and Koh, 2007).

2.5 Hydrate formation

There are three basic steps for any crystallization: supersaturation, nucleation, and growth of crystal (Mullin, 1961). Hydrate formation is analogous to crystallization (Sloan Jr and Koh, 2007). All these three steps of hydrate formation are schematically shown in Figure 2.7. This shows the consumption of gas during the crystallization process in a stirred tank reactor (Bishnoi, 2005).

The hydrate guest first dissolves into the liquid water until the system becomes saturated at a given temperature and pressure. Afterward, gas continues to dissolve in the aqueous phase, from point A to B in Figure 2.7, forming a supersaturated system. After point A, the system is in the hydrate stable region. However, this does not necessarily mean that hydrates will form due to metastability of the system. The time taken from point A to B is known as induction time. During this time interval, small hydrate nuclei form and dissociate until a critical radius size achieved. The time when stable nuclei is achieved is known as hydrate nucleation. These stable nuclei continue to grow resulting in macroscopically visible crystals and consumption of a detectable amount of gas. The time interval between the equilibrium and turbidity point is dominated by hydrate nucleation, a process that is not observable by macroscopic measurements (Sloan Jr and Koh, 2007). The temperature and pressure during induction time are within the hydrate stability region. After point B, fast uptake of gas is shown that is due to the rapid growth of crystal (Bishnoi, 2005). In hydrates, guest molecules are packed at a higher density than in the fluid phase resulting in a significant consumption of gas (Sloan Jr and Koh, 2007).

2.5.1 Supersaturation

Hydrate formation is analogous to crystallization so it requires supersaturation to occur (Bishnoi, 2005). The aqueous phase is considered supersaturated when it contains more dissolved gas (solute) than the solubility of the gas at

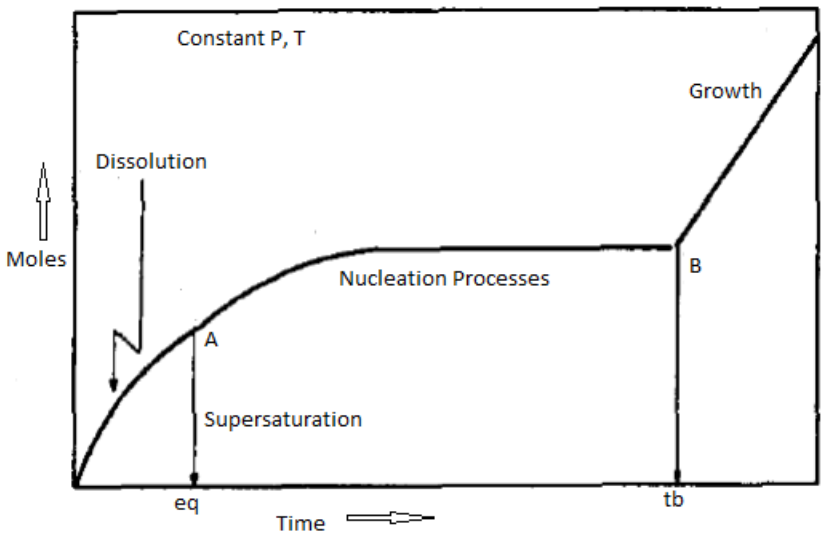

Figure 2.7 – Consumption of hydrate forming gas in a stirred reactor as time progresses. Adapted from Bishnoi (2005).

a given temperature and pressure (Mullin, 1961). The formation of a new phase requires a driving force, which corresponds to the deviation from the equilibrium condition (Sloan Jr and Koh, 2007). Deviation from equilibrium is described by the difference in chemical potential between the experimental conditions and the conditions at equilibrium. Supersaturation can be considered as a driving force for crystallization because it indicates deviation from equilibrium solubility, but most often subcooling is used as an indicator of driving force. The degree of subcooling is defined as $\Delta T_{\text{sub}} = T_{\text{eq}}$ - T_{exp}, where T_{eq} is the H-L-V equilibrium temperature and T_{exp} is the experimental temperature at a given pressure, Figure 2.8 (Kelland, 2006).

2.5.2 Nucleation

Nucleation is a stochastic process during which small clusters of water and guest grow and disperse in attempt to achieve critical size for continued growth (Sloan Jr and Koh, 2007). The time period before nucleation is called the induction time because crystal nuclei are not visible to macroscopic probes. The induction time can be described, in practice, as the time elapsed until the appearance of a detectable volume of hydrate phase (Bishnoi, 2005).

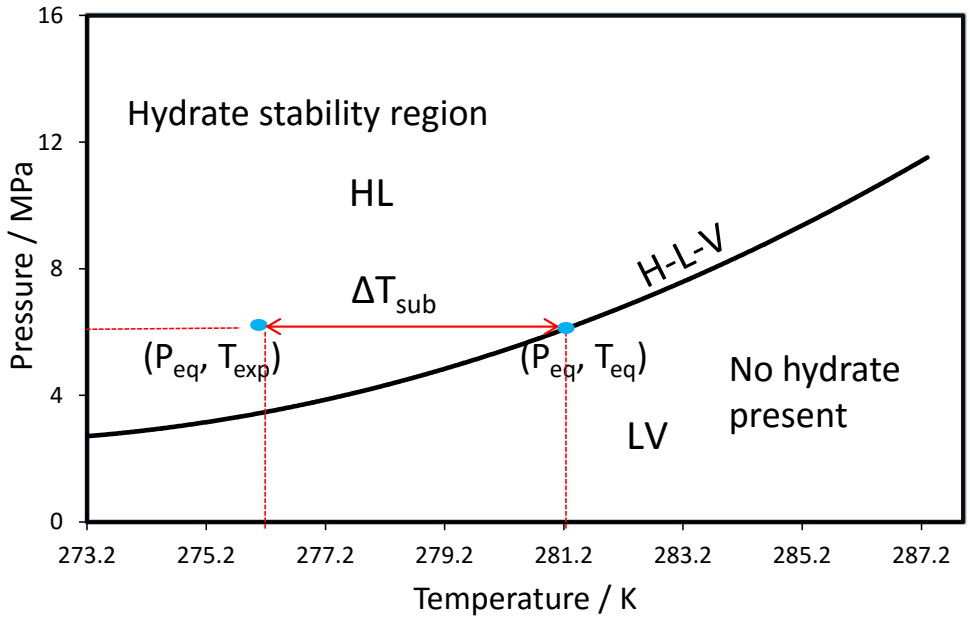

Figure 2.8 – Schematic representation of how a partial phase diagram could be used to determine subcooling.

Hydrate nucleation is stochastic and therefore unpredictable (Bishnoi, 2005), so induction times are very scattered. Induction time depends on several factors such as apparatus geometry, the degree of agitation, surface area of the system, rate of heat and mass transfer, history of water, the gas composition, and the presence of foreign particles (Sloan Jr and Koh, 2007). It is well-understood that the degree of subcooling (from the equilibrium temperature) or over pressurization (from equilibrium pressure) greatly affect the induction time for hydrate formation (shorter induction times are often observed for greater subcooling or over pressurization) (Sum *et al.*, 2009).

Nucleation may occur spontaneously or it may be induced artificially (Mullin, 1961). There are two types of nucleation: homogeneous nucleation, which occurs in the absence of any impurities, and heterogeneous nucleation, which occurs in the presence of foreign substances. The foreign substance lowers the energy barrier for hydrate nucleation, so heterogeneous nucleation is more frequent.

Hydrates preferentially form at the gas-water interface because of the large concentration gradient at the interface. The mutual solubility is lower in either phases than the required concentration for hydrate formation, water

mole fraction in the gas phase is typically around 0.05 and the mole fraction of guest in the water phase is lower than 0.001 (Sloan *et al.*, 2010). The low concentration of either the guest or the host in the bulk phases means that critical nuclei are unlikely; however, at the interface, there is a large concentration of both host and guest which makes the formation of a crystal of critical size more likely (Sloan Jr and Koh, 2007).

2.5.3 The memory effect

There are many factors that can affect induction time and hydrate growth, but one of the most easily controlled factor in a quiescent system is solution history. It is well known that forming hydrates using water that has been previously crystallized significantly reduces the induction time. This phenomenon is commonly called the memory effect. This solution memory appears to vanish when the system is heated sufficiently above the hydrate equilibrium conditions, or if it is left outside of the hydrate stability region for an extended time after dissociation.

There are two general theories to explain the memory effect. The first theory proposes that hydrate dissociation leaves crystallites in the liquid, providing a pre-existing surface upon which future nucleation may occur. The second theory adduces that the dissociation of hydrates leaves the bulk liquid with a higher concentration of guest than that which was initially present prior to hydrate formation (Sloan Jr and Koh, 2007).

2.5.4 Hydrate growth

Once hydrate nuclei reaches critical size, the hydrate crystal growth period begins. Hydrate crystal growth is characterized by the incorporation of significant amount of gas (at least two orders of magnitude greater than the gas solubility) into the hydrate phase (Sloan Jr and Koh, 2007). Thus, this process is limited by mass transfer between the bulk fluid phases and growing hydrate, in addition to the factors that affect nucleation (Davies *et al.*, 2010). Since the pre-formation concentration is higher near the water-guest interface, the hydrate crystal growth is most likely to occur into the water phase, near the interface, where there is a large supply of guest molecules available to move into the hydrate phase (Taylor *et al.*, 2007). In addition, hydrate formation is an exothermic process, so heat transfer rates can also control the rate of growth.

The lateral growth rate of the hydrate film at the water-guest interface has been theoretically and experimentally studied by several groups (Li *et al.*, 2015, 2013, 2014; Peng *et al.*, 2007; Kitamura and Mori, 2013). Intrinsic kinetics (Englezos *et al.*, 1987) and heat transfer limitations (Mochizuki and Mori, 2006; Peng *et al.*, 2007; Freer *et al.*, 2001) are generally regarded as rate controlling of hydrate film growth. Over time, however, the growth of the film is believed to transition to a process limited by the mass transfer of guests or water through the hydrate film (Taylor *et al.*, 2007; Mori and Mochizuki, 1997, 1996).

2.6 Morphology

Observational studies provide a physical picture of the phenomena that occur upon hydrate crystallization on the water surface (Beltran and Servio, 2010). The lateral growth of the hydrate film at the water-guest interface has been studied by several groups and recently reviewed by Sun *et al.* (2010). It is generally accepted that in quiescent systems, hydrate preferentially forms and grows as a thin film at the water-guest interface between both fluids until the interface is covered by a thin hydrate layer (Kitamura and Mori, 2013; Li *et al.*, 2013, 2014; Beltran and Servio, 2010; Servio and Englezos, 2003; Davies *et al.*, 2010; Sabase and Nagashima, 2009; Freer *et al.*, 2001; Kitamura and Mori, 2013; DuQuesnay *et al.*, 2015; Li *et al.*, 2015).

Servio and Englezos (2003), studied the morphology of carbon dioxide and methane hydrate crystals formed on nearly spherical water droplets. It was observed that when hydrates were formed at high driving force, the water droplets quickly became jagged and exhibited many needle like crystals extruding from the water droplets, whereas at low driving force the surface was smooth (Servio and Englezos, 2003). Furthermore, the type of hydrate forming gas did not have any effect on morphology. They observed that all the droplets nucleated at the same time, and speculated that this could be attributed to a bridge formed by minute water droplets between the original water droplets (Servio and Englezos, 2003). In almost all experiments, a collapse of the hydrate layer was seen to occur. The authors suggested that this collapse of hydrate layers surrounding the droplets showed that the water was still being converted to hydrate (Servio and Englezos, 2003).

Beltran and Servio (2010), studied the morphology of methane hydrate on a glass surface and reported that hydrate first nucleated on the periphery of the droplet and second nucleated within the water film with a different

morphology. This difference in morphology tended to disappear over time (Beltran and Servio, 2010). It was found that high driving forces showed a smoother surface than low driving force. Furthermore, a third hydrate layer that grew outside the original water boundary known as hydrate halo was observed (Beltran and Servio, 2010). The authors showed that the growing front could induce nucleation by creating a"bridge" between segregated water droplets (Beltran and Servio, 2010). Later, Esmail and Beltran (2016) showed that once the hydrate film had formed on the droplet surface, the liquid water underneath the hydrate layer was drawn by capillarity towards the water free surface and the hydrate film grew on the advancing water layer.

Davies *et al.* (2010) observed that the hydrate films formed at the gas-water interface are initially quite porous, exhibiting much higher transport rates than would be expected of a solid hydrate film. The mass transfer resistance increased as the hydrate aged, and it also depended on the hydrate forming condition of the film.

Taylor *et al.* (2007) studied hydrate film growth at the hydrocarbon-water interface for cyclo-pentane and methane, and reported that hydrate formation was initiated by the propagation of a thin porous film across the hydrocarbon-water interface (Taylor *et al.*, 2007). The thickening rate of the hydrate layer was found to be strongly dependent on guest solubility in the aqueous phase and the thickness of the hydrate layer increased with increasing ΔT_{sub} (Taylor *et al.*, 2007). Furthermore, it was suggested that the initial supply of guest species for hydrate growth came from the aqueous phase, followed by a vapor phase supply of guest during the thickening stage of hydrate film formation (Taylor *et al.*, 2007).

Freer *et al.* (2001) found that hydrate crystal morphology changed with the driving force. They observed that when the driving force was low, hydrate exhibited faceted morphology and at high driving force hydrate exhibited a polycrystalline hydrate layer. Heat transfer was considered to be the controlling process and mass transfer was assumed negligible (Freer *et al.*, 2001). The growth rate was found to be proportional to the subcooling, and crystallization was seen to proceed by a continuous growth mechanism at high ΔT_{sub} and step growth at low ΔT_{sub} (Freer *et al.*, 2001).

2.7 Hydrate inhibitors

Flow assurance is one of the major technical challenges in oil and gas production operations because the conditions at which oil and gas are produced, processed, and transported are frequently suitable for gas hydrate formation (Chua and Kelland, 2013).

A conceptual mechanism for hydrate plug formation in gas-dominated pipelines has been put forward (Zerpa *et al.*, 2012) and is shown in Figure 2.10. First, a water film accumulates at a pipe bend. Gas bubbles flow through the accumulated water and due to the heat transfer between the pipeline and colder surroundings hydrates are formed. Through thickening of the hydrate layer, an annulus is formed which is generally non-concentric with the pipe. Flowing liquid through the annulus causes sloughing of the annulus and plugging downstream.

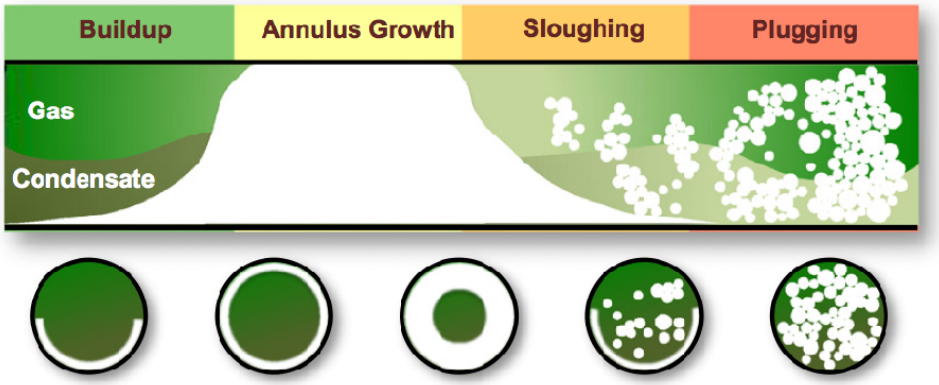

Figure 2.9 – Hydrate plug formation mechanism in gas dominated systems (Zerpa *et al.*, 2012).

Methods to prevent hydrate plugs include raising the temperature (by burying the pipelines, heat addition, and insulation) above the equilibrium temperature at a given pressure, lowering the pressure below the equilibrium pressure at a given temperature, removing the water and shifting the equilibrium for hydrate formation by adding anti-freeze chemicals (Sloan Jr and Koh, 2007; Kelland *et al.*, 2006).

2.7.1 Thermodynamic hydrate inhibitors

Traditionally, gas hydrates have been prevented by adding thermodynamic hydrate inhibitors (THIs) such as methanol, monoethylene glycol and sodium chloride to the aqueous phase. These chemicals work by shifting the hydrate equilibrium conditions to higher pressures and lower temperatures (Wu *et al.*, 2014; Luna-Ortiz *et al.*, 2014), (Lafond *et al.*, 2012; Sloan Jr and Koh, 2007; Urdahl *et al.*, 1995). The hydrate stability region in the presence of ethylene glycol is shown in Figure 2.10, with increasing THIs concentration in aqueous phase, hydrate stability region decreased.

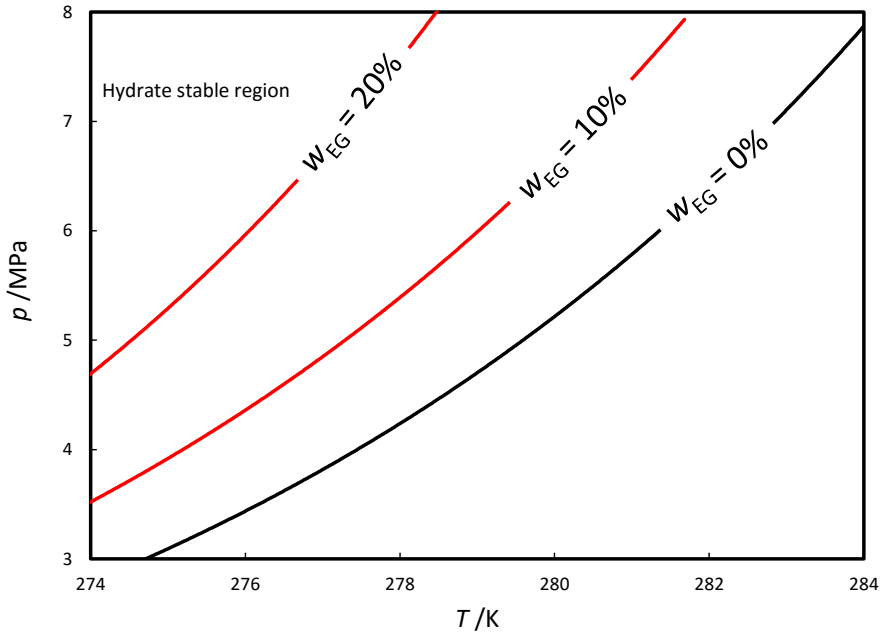

Figure 2.10 – Hydrate stability region in the presence of ethylene glycol. Data compiled by Sloan Jr and Koh (2007).

Salts readily dissolve into ions upon addition to water. Water molecules are tightly bound around the ions in the hydration layer through electrostatic interactions between the ions and water molecules (Cha *et al.*, 2015). This interaction between water molecules and salt ions also reduces the solubility of hydrate guest in the water (Sloan Jr and Koh, 2007). So hydrate equilibrium conditions are shifted into higher pressure and lower temperature conditions.

The study of hydrate formation in the presence of NaCl is important because naturally occurring water typically contains dissolved salts. Phase equilibria of the hydrate systems in the presence of NaCl have been studied extensively (Cha *et al.*, 2015; Jager *et al.*, 2002; Mohammadi and Richon, 2009a), (Østergaard *et al.*, 2005). Sodium chloride effectively decreases the hydrate stability region in a hydrate forming system phase diagram, and crystal growth rate decreases with increasing salt concentration (Peng *et al.*, 2009; Uchida *et al.*, 2002; Kishimoto *et al.*, 2012).

There are a few reports on the morphology of methane hydrate, (Makogon *et al.*, 2000) carbon dioxide hydrate, (Peng *et al.*, 2009) and cyclopentane hydrate (Kishimoto *et al.*, 2012; Sakemoto *et al.*, 2009) in the presence of NaCl or seawater. For cyclopentane hydrates it was observed that the size of individual hydrate crystal decreased with increasing subcooling. It was observed that salt concentration had little impact on hydrate morphology at a fixed subcooling (Kishimoto *et al.*, 2012; Sakemoto *et al.*, 2009).

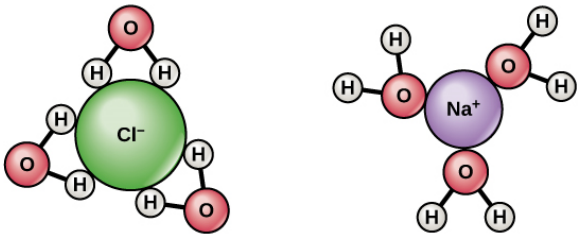

Figure 2.11 – Schematic illustration of electrostatic interaction between the NaCl ions and the water molecules, hence making those water molecules unavailable to hydrogen bond with other water molecules.

The inhibition capability of ethylene glycol is due to attractive nature of the oxygen atoms of ethylene glycol for neighboring water molecules. Each oxygen atom in the Figure 2.12 has two loan-pair of electrons, which provides two negative charges. The negative charges attract the positive charge on the hydrogen of a neighboring water molecule to form a hydrogen bond between EG and water molecule. This H-bonding between water molecules and EG acts as a competitor for the H-bonding in water molecules in hydrates, making it difficult for water molecules to participate in hydrate formation.

Several groups have studied phase equilibria of hydrate systems in the presence of ethylene glycol (EG) (Sloan Jr and Koh, 2007; Mohammadi and Richon, 2009b, 2010; Jager *et al.*, 2002; Mohammadi and Richon, 2009a; Østergaard *et al.*, 2005). The above mentioned studies concentrated on the performance of

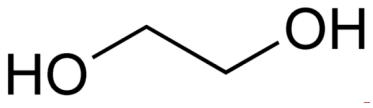

Figure 2.12 – Chemical structure of ethylene glycol.

EG as a thermodynamic inhibitor and did not investigate kinetics of hydrate formation or crystal morphology. Cha *et al.* (2013a) reported that the presence of EG in the aqueous phase delayed hydrate formation and lowered the crystal growth rate. They suggested that the kinetic inhibition performance of ethylene glycol should be included in the current hydrate inhibition strategy to avoid plug formation.

2.7.2 Low dosage hydrate inhibitors

Over the last two decades, low dosage hydrate inhibitors (LDHIs) have seen increasing use as alternatives to THIs (Kelland *et al.*, 2006). LDHIs are used in concentrations as low as 0.5 to 1% by weight. Clearly, such a large reduction in inhibitor dosage makes them a more cost effective inhibition method in comparison with traditional THIs.

Low dosage hydrate inhibitors are mainly divided into two groups: (1) kinetic hydrate inhibitors (KHIs), and (2) anti-agglomerants (AAs).

Kinetic hydrate inhibitors

KHIs act primarily as gas hydrate anti-nucleators, although most of them also delay the growth of gas hydrate crystals (Daraboina *et al.*, 2011c; Luna-Ortiz *et al.*, 2014). KHIs are generally water-soluble polymers. Low molecular weight polyvinylpyrrolidone (PVP), and polyvinylcaprolactam (PVCap) are the most commonly researched KHIs, both of them contain lactam ring structures (Kelland, 2006; Sloan Jr and Koh, 2007).

Both experimental and theoretical studies have been done to investigate the mechanism of hydrate growth inhibition at either the nucleation or hydrate growth stage (Anderson *et al.*, 2005; Posteraro *et al.*, 2015). A two-step mechanism by which KHIs work has been proposed involving (a) disruption of local

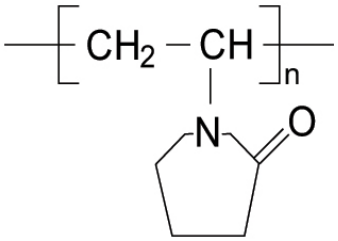

Figure 2.13 – Chemical structure of polyvinylpyrrolidone.

water order in liquid water and (b) inhibitor binding to the growing crystal surface with a polymer lactam ring as shown in Figure 2.13 (Davenport *et al.*, 2011; Wu *et al.*, 2014; Larsen *et al.*, 1998).

Recently, it has been observed that even though KHIs reduce hydrate growth rate, a breakthrough point occurs where rapid hydrate growth also known as catastrophic hydrate growth is observed (Sharifi *et al.*, 2014a,b; Cha *et al.*, 2013b; Lee and Englezos, 2006; Kumar *et al.*, 2008). The reason for the catastrophic growth is still unclear, although it has been proposed that the hydrate formed with KHIs might be more porous compared to the pure system. This increased porosity would allow capillary movement of guests across the hydrate film (Sharifi and Englezos, 2014; Lee and Englezos, 2006; Austvik *et al.*, 2000). Compared to the pure water system, thinner hydrate layers have been observed on the water-guest interface in the presence of PVP (Bruusgaard *et al.*, 2009; Wu *et al.*, 2013).

The effect of PVP on hydrate growth kinetics has been previously studied (Posteraro *et al.*, 2015; Daraboina *et al.*, 2011b; Perfeldt *et al.*, 2014; Jensen *et al.*, 2010). It was observed that the hydrate crystal growth rate decreased with increasing PVP concentration (Posteraro *et al.*, 2015).

KHIs are known to interact in a complex manner with hydrates. For example, multiple hydrate melting points have been observed for hydrates formed with KHIs such as PVP, whereas a single melting point was observed for the hydrate formed with the pure water system (Daraboina *et al.*, 2011a). Thus, hydrates formed with KHIs are more stable and can dissociate at higher temperatures than the hydrates formed with the pure system (Daraboina *et al.*, 2011a,b,c; Sharifi *et al.*, 2016; Bruusgaard *et al.*, 2009). Sharifi *et al.* (2016) showed that these multiple melting points are not due to crystalline structural changes, but rather to the interaction with kinetic inhibitors.

Anti-agglomerants

Anti-agglomerants (AAs) allow hydrate formation, but restrict hydrate particle agglomeration. As a result, transportable, nonsticky hydrate slurry forms (Kelland *et al.*, 2006, 2000). Quaternary ammonium surfactants are the most widely used AAs (Chua and Kelland, 2013). In these AAs, two or three of the four ammonium branches are short (n-butyl, n-pentyl, or isopentyl) that tend to attach to the hydrate crystal surface and one or two are long hydrophobic branches that might be soluble within the oil phase (Sloan Jr and Koh, 2007). The chemical structure of a widely studied AA, tetrabutyl ammonium bromide (TBAB) is shown in Figure 2.14. The butyl-ammonium end of TBAB is very attractive to water and hydrates, so that it remains firmly attached to either hydrate phase or water droplet, after the water droplet conversion into hydrate and the other butyl-ammonium branches stabilized the hydrate particles in liquid-hydrocarbon phase, so they will never accumulate (Sloan Jr and Koh, 2007).

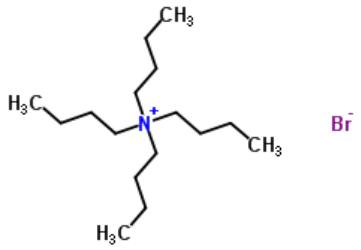

Figure 2.14 – Chemical structure of tetra-butyl ammonium bromide.

For high subcooling applications, AAs are more effective than KHIs for prevention of hydrate plug formation in oil and gas pipelines. In addition, it has been reported that performance of AAs can be improved by increasing salinity (Chua and Kelland, 2013; Kelland *et al.*, 2006).

Quaternary salts have been used in two ways for prevention of hydrate formation, as antiagglomerants when modified into surfactants (Chua and Kelland, 2013; Kelland *et al.*, 2006) and as synergist with KHI polymers (Chua *et al.*, 2012).

Quaternary salts such as tetrabutylammonium bromide (TBAB) do not inhibit sII gas hydrate nucleation instead they encourage hydrate formation (Kelland, 2006). A plausible mechanism for this promotion effect on hydrate formation is that these quaternary salts form hydrate structures of their own which have

some similarities with sII hydrates. Therefore, they act as a template for the initial hydrate formation (Kelland, 2006).

Phase equilibrium of methane + TBAB in aqueous solutions has been studied by several groups (Sangwai and Oellrich, 2014). The presence of TBAB in aqueous solutions shifts methane hydrate formation conditions to lower pressures and higher temperatures (Hashimoto *et al.*, 2008). Sangwai and Oellrich (2014) have reported two equilibrium points for TBAB hydrate dissociation: one corresponding to pure methane hydrate phase equilibria, while the second one corresponding to semiclathrates of methane. The presence of NaCl in aqueous TBAB solutions has been reported to inhibit semiclathrate formation at low concentrations of TBAB, and to promote semiclathrate formation at high concentrations of TBAB (Sangwai and Oellrich, 2014).

Various types of reactors have been used to study the performance of above mentioned gas hydrate inhibitors. Typically, the experimental temperature of the hydrate system is controlled though the pressure vessel by a coolant bath or coolant jacket. This leads to slow response times (in the order of minutes) for a change in set-point temperature. Generally hydrates apparatus are restricted to measure one or two parameters at one time.

DuQuesnay *et al.* (2015) designed a novel reactor which offered strict control of the crystallization substrate temperature, regardless of ambient conditions and efficiently allowed for the assessment of crystal morphology, apparent kinetics and phase equilibria in a single experiment. To date, the use of this method to investigate the performance of hydrate inhibitors has not been explored. The main objective of this work is to test this technique with thermodynamic and low doses hydrate inhibitors.

Chapter 3

Experimental

3.1 Materials

Table 3.1 reports the suppliers and purities of the materials used in this study. Aqueous solutions were prepared by gravimetric method using an analytical balance. Mass fraction standard uncertainties were estimated to be 0.001.

Table 3.1 – Specifications of the materials used in the experiments.

Chemical name	Source	Purity	Purity units
Ethylene glycol	Fisher Scientific, Canada	$\geq$ 99.80%	
Sodium chloride	Caledon Laboratory Ltd	$\geq$ 99.0%	
PVP10	Sigma-Aldrich Canada Co.	N/A	
TBAB	Sigma-Aldrich Canada Co.	$\geq$ 99.0%	
Methane	Air Liquide, QC Canada	99.999%	
Nitrogen	Air Liquide, QC Canada	99.999%	
Water	In-house	18	MΩ·cm

Polyvinylpyrrolidone with an average molecular weight of 10 kDa (PVP10) was obtained from Sigma-Aldrich in powder form. The purity of PVP10 was not available from the manufacturer.

3.2 Apparatus

A schematic of the experimental setup designed by DuQuesnay *et al.* (2015) is shown in Figure 3.1. A pressure vessel made of 316 stainless steel, housed a bilateral temperature control stage equipped with two thermoelectric coolers (TEC) (Figure 3.2). The cell had several ports for gas inlet, gas outlet, temperature probes, wiring and to communicate pressure to a pressure transducer. Sapphire windows (Rayotek, CA, USA) were affixed at the top and bottom of the reactor. The bottom window was used for illumination using a Schott KL2500 cold light source (Optikon, ON, Canada). The top window allowed sample observation. Video recording was done using a PCO.2000 camera (Optikon, ON, Canada) equipped with an infnity KC microscope objective (Optikon, On, Canada) or with an AF-Micro-Nikkor 60 mm lens (Optikon, ON, Canada).

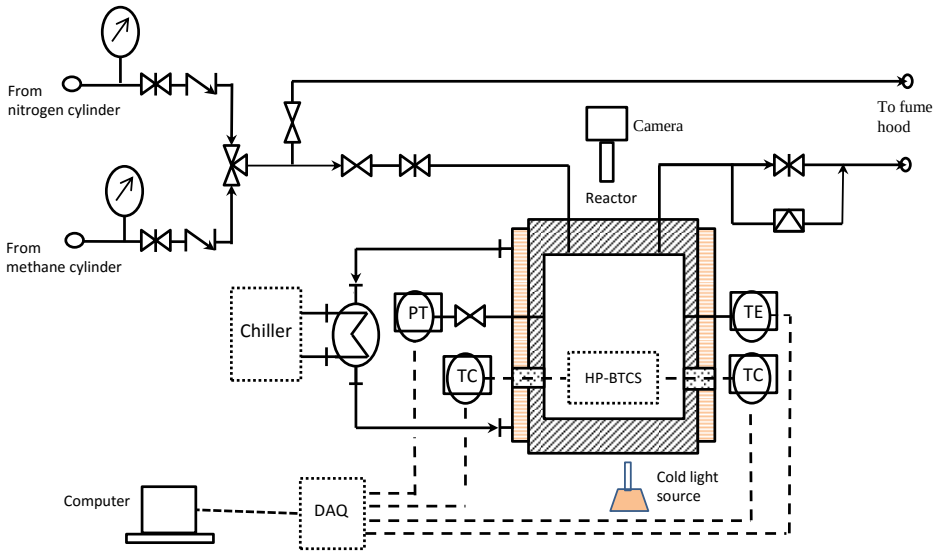

Figure 3.1 – Schematic of the complete experimental setup. TE: temperature element. PT: pressure transducer. TC: temperature controller. HP-BTCS: high pressure-bilateral temperature control stage. DAQ: data acquisition.

The pressure vessel was cooled with a Thermo AC200 chiller (Fisher Scientic, Canada) recirculating a mixture of ethylene glycol and water (50=50; V/V) through a copper coil wrapped around the exterior of the reactor. Temperature inside the crystallizer was measured with a Platinum RTD probe (± 0.32 K) (Omega Engineering, QC Canada) and pressure was monitored with a

Rosemount 3051s pressure transducer (± 0.025% of the span) (Laurentide Controls, QC, Canada).

The thermoelectric module (TEC) stage was used to independently control temperature on both sides of the sample slide. Figure 3.2 shows the stage assembly schematically. A pair of thermoelectric coolers (TEC) (TE Technology, MI, USA) installed on opposite sides of the stage transferred heat from the top to the bottom of the stage. Copper plates were fixed to the top and the bottom of each TEC to ensure uniform cooling. The body of the pressure vessel was used as a heat sink for the bottom of each TEC. Thermistor elements (± 1 K) (TE Technology, MI, USA) were used to measure the temperature of the copper plates. A sapphire slide was used to hold a sample droplet and to connect both ends of the stage. Two PID temperature controllers (TE Technology, MI, USA), with a resolution and a temperature control stability of ± 0.01 K, were used to control the TEC's. Wires, necessary to power the thermoelectric coolers and to connect to the PID controllers, were fed through Conax Technologies fittings (Electro-Meters, ON, Canada) attached to the vessel walls.

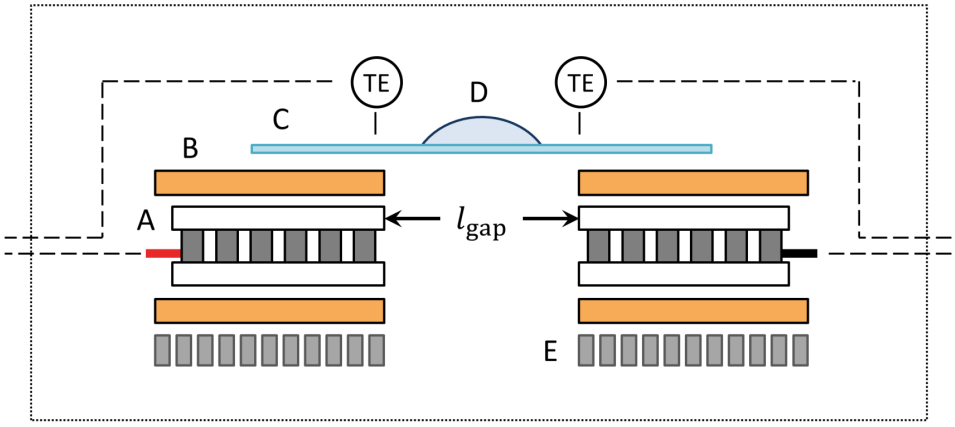

Figure 3.2 – Schematic of the High-Pressure Bilateral Temperature control stage. (A) Thermoelectric cooler module. (B) Copper plate. (C) Sapphire substrate. (D) Water droplet. (E) Heat sink (adapted from DuQuesnay *et al.* (2015)).

3.3 Methods

A clean sapphire slide was placed on the TEC stage, and a 20 “micro”L droplet of the sample solution was transferred to the slide with a micro-pipette. Subsequently, the vessel was sealed and purged with nitrogen. The crystallizer was then filled with methane and purged several times.

3.3.1 Crystal formation history

Before hydrate formation, the sample droplet was pre-treated to form ice and gas hydrates. The pretreatment sequence is shown in Figure 3.3. After purging with methane, the entire vessel was cooled to approximately 273.2 K while maintaining the pressure slightly above atmospheric pressure. The stage temperature was then dropped to 253.2 K to form ice. Once ice had formed, the pressure was increased to the experimental pressure. The vessel temperature was set to slightly above the hydrate-liquid-vapor (H-L-V) equilibrium temperature at the experimental pressure. Subsequently, the stage was heated just above 273.2 K, inducing gas hydrate formation. Finally, the stage temperature was increased just above the H-L-V at experimental pressure in order to dissociate the newly formed methane hydrate.

3.3.2 Hydrate formation

Following the pre-treatment of the sample droplet, the pressure and temperature surrounding the stage were maintained constant. The TEC stage was used to locally cool the sample droplet to the experimental temperature conditions. Hydrates were formed on a constant temperature gradient surface or a uniform temperature surface, but first both sides of the stage were cooled to near the H-L-V equilibrium temperature. For a uniform surface temperature, both sides of the stage were cooled at the same temperature below the H-L-V equilibrium temperature at the experimental pressure (Figure 3.4 (a)). For constant gradient temperature surface, one side was cooled to obtain a temperature difference of 4 K across the stage (Figure 3.4 (b)). The stage temperature conditions were held constant during hydrate formation.

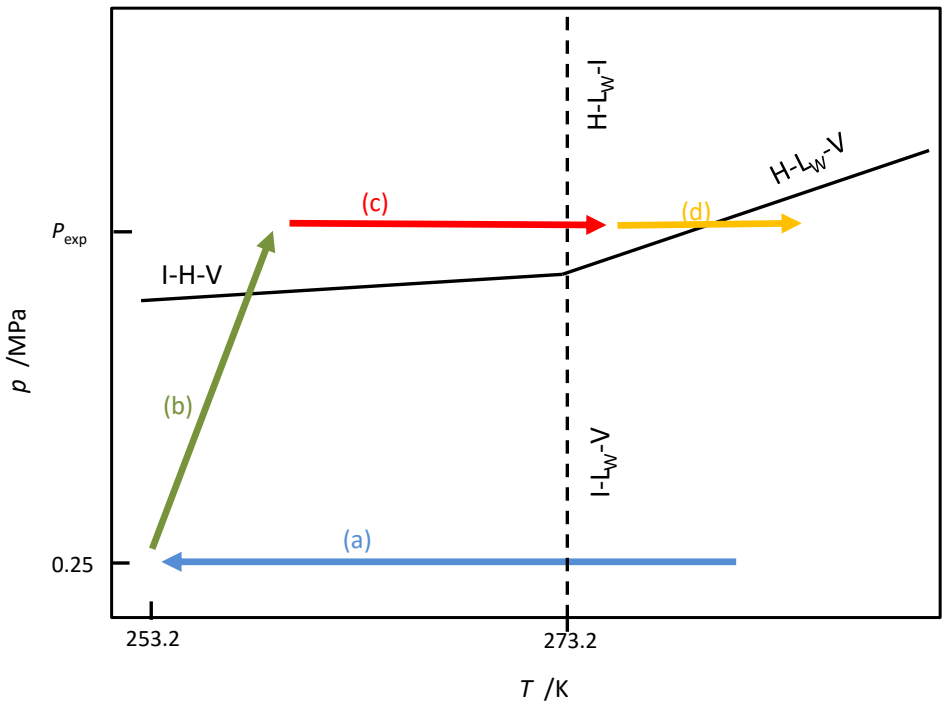

Figure 3.3 – Sample droplet pre-treatment before hydrate formation . (a) Ice formation. (b) Vessel pressurized to experimental pressure. (c) Hydrate formation from ice. (d) Hydrate dissociation. (Reproduced from DuQuesnay *et al.* (2015)).

3.3.3 Hydrate dissociation

The temperature and pressure surrounding the stage were maintained constant during hydrate dissociation. Similar to hydrate formation, the hydrate dissociation was also conducted on a constant temperature gradient surface and a uniform surface temperature.

For a constant temperature gradient dissociation, the high temperature on the TEC stage was set slightly above the H-L-V temperature and the low temperature was set to achieve a temperature difference of 4 K across the stage. Low and high set points were then increased simultaneously in 0.5 K increments. The temperature was held constant at both ends of the stage while the hydrate dissociated in the region of the stage above the H-L-V equilibrium temperature and the hydrate-water interface stabilized. For each step increment in the set point, the hydrate-water interface position moved

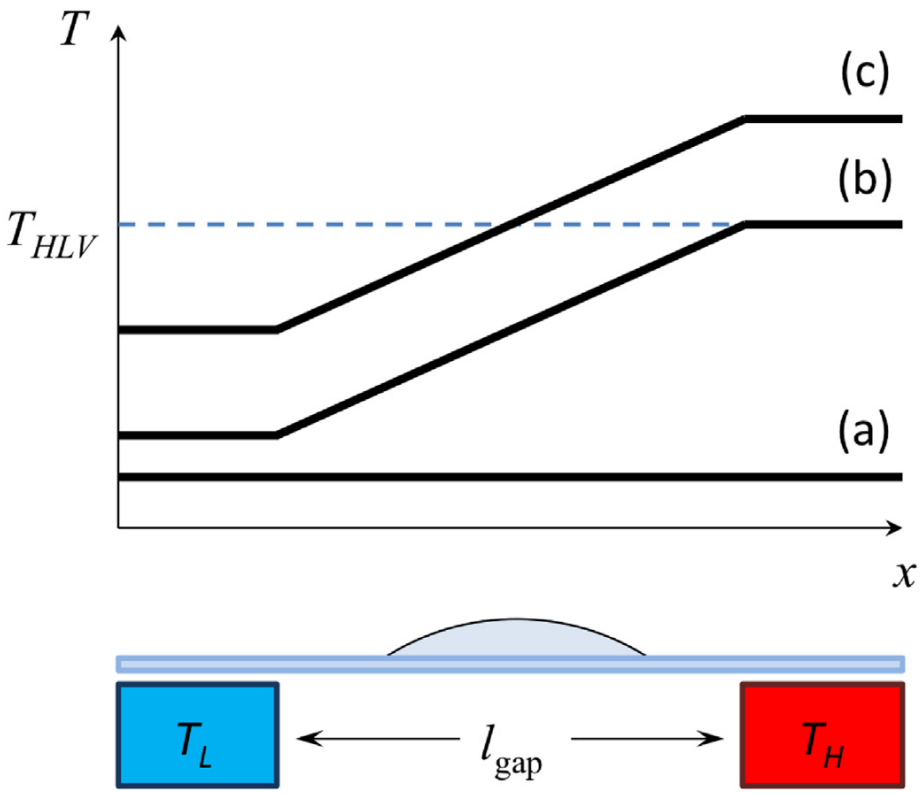

Figure 3.4 – Demonstration of the temperature profiles used in this work. (a) Uniform surface temperature. (b) Constant temperature gradient. (c) Constant temperature gradient where the temperature profile crosses the H-L-V equilibrium temperature. (adapted from DuQuesnay *et al.* (2015)).

towards the cold side of the stage (Figure 3.4 (c)).

For uniform surface temperature dissociation, a constant temperature below the H-L-V equilibrium temperature was set on both sides of the stage. Then, temperature was simultaneously increased on both sides of the stage in steps of 0.5 K. Temperature was maintained constant for 4 to 5 minutes at every step until the surface temperature was approximately 0.5 K below the expected H-L-V equilibrium temperature. From this point on, increments were reduced to 0.1 K and temperature was held for 20 minutes at every step until the complete hydrate dissociation occurred.

Chapter 4

Results

Hydrate formation and dissociation experiments were performed to assess the effect of adding gas hydrate inhibitors on hydrate crystal morphology, apparent kinetics, and phase equilibria. Hydrates were formed from quiescent water droplets, deposited on sapphire slides and immersed in a methane atmosphere. Tight, local temperature control was achieved as explained in Section 3.3.2 and shown in Figure 3.4. Two types of temperature profiles were used: uniform constant temperature and constant temperature gradient. Uniform temperature experiments maintained the same temperature across the slide. Constant temperature gradient experiments sustained a constant temperature on one side of the slide while maintaining a constant lower temperature at the other end of the slide. As a result, the driving force for hydrate formation increased across the length of the slide. The end of the slide with the higher temperature will be denoted as the low driving force end and the side of the slide with the lower temperature will be denoted as the high driving force end.

In order to shorten the induction time for hydrate nucleation, all the hydrate formation experiments were performed with water droplets that had undergone previous clathrate formation (Section 3.3.1). I performed a minimum three experimental runs at each experimental condition for all systems used in this study and confirmed the reproducibility of the observed crystal growth behavior, film velocity, and phase equilibria. Methane hydrate formation from pure water has been studied previously using the same apparatus as in this work (DuQuesnay *et al.*, 2015). In this study, the focus is on water with inhibitors; however, new information is added with respect to the pure system.

The degree of subcooling (ΔT_{sub}) will be used as a measure of the driving force

for hydrate formation. The degree of subcooling is defined as $\Delta T_{\text{sub}} = T_{\text{eq}} - T_{\text{exp}}$, where T_{eq} is the hydrate-liquid-vapor (H-L-V) equilibrium temperature and T_{exp} is the experimental temperature at a given pressure.

4.1 Hydrate formation

4.1.1 Water + CH_4

Uniform surface temperature

Figure 4.1 depicts the sequence of hydrate formation on a water droplet completely immersed in a methane atmosphere at uniform surface temperature. Nucleation of methane hydrate was observed at the random points in the droplet. After nucleation, the initial growth points floated to the center of the droplet. A polycrystalline hydrate film then advanced towards the boundary of the droplet and eventually covered the entire surface of the water droplet. Following complete coverage of the droplet surface by the hydrate film, a thin film of hydrate propagated onto the sapphire substrate outside the original water boundary. Clathrate propagation outside of the original water boundary has been referred to previously as a "hydrate halo" (Beltran and Servio, 2010).

Figure 4.2 presents magnified views of methane hydrate morphology on a water droplet maintained at uniform surface temperature. The large single crystal that can be seen in the hydrate film is representative of large crystals that formed occasionally and on random locations across the droplet. These large crystals floated towards the center of the droplet, but they did not attach to the main growth front initially. Instead, these almost translucent large crystals grew ahead of the main hydrate interface. Eventually, large crystals became evident near the surface of the droplet and attached to the main growth front Figure 4.3.

Constant temperature gradient

Figure 4.3 presents the sequence of methane hydrate formation on a water droplet while a temperature gradient was applied along the sapphire slide. The initial hydrate growth occurred in the same way as hydrate growth on the constant temperature surface, where hydrate nucleated at the random points in the droplet and subsequently floated to the center of the droplet.

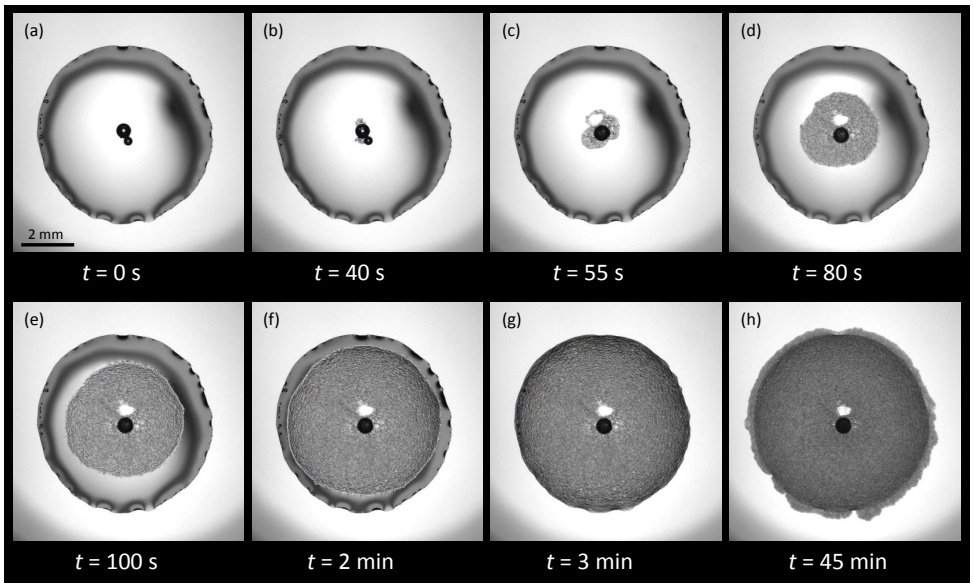

Figure 4.1 – Methane hydrate formation and growth on a water droplet at constant temperature. $p = 4$ MPa, $T = 275.5$ K ($\Delta T_{\mathrm{sub}} = 2$ K). (a) Water droplet before hydrate formation. (b) Initials growth points floated to the center of the droplet. (c-f) Continued growth from the droplet center. (g) Droplet is completely covered by hydrate. (h) Hydrate propagation outside the droplet boundary.

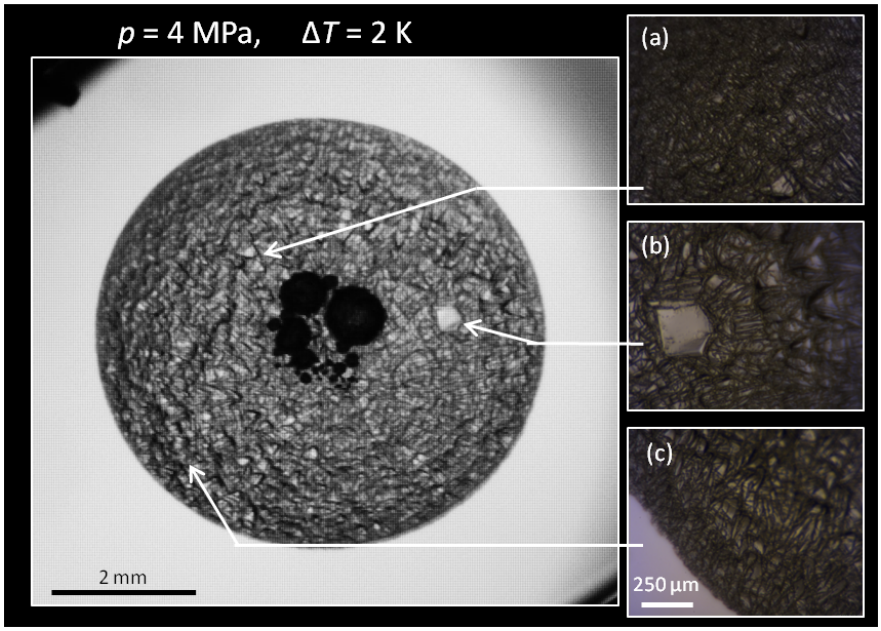

Figure 4.2 – Methane hydrate formed at uniform surface temperature. p = 4 MPa, T = 275.5 K (ΔT_{sub} = 2 K). (a) Granular crystals. (b) Large single crystals in the hydrate crust. (c) Boundary between the water droplet and the sapphire slide.

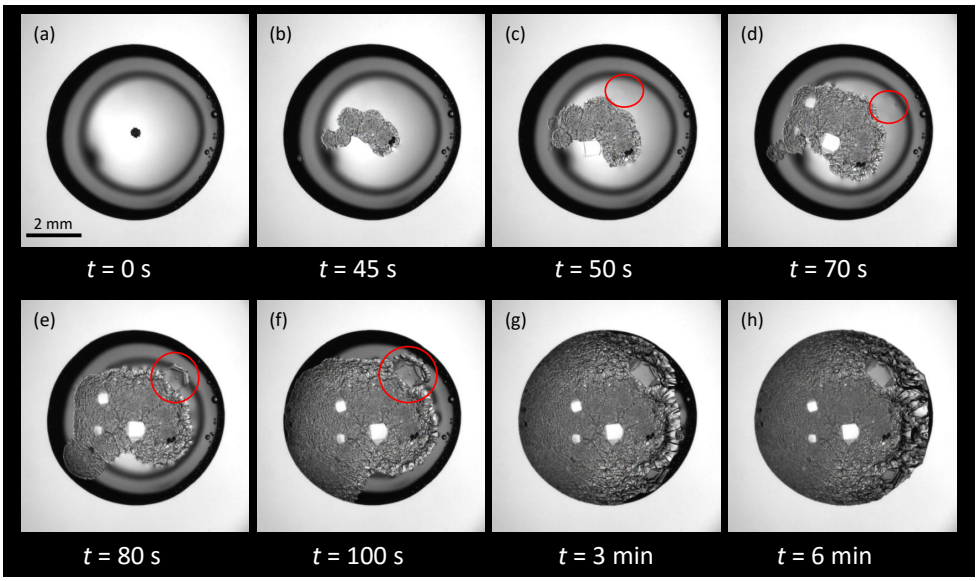

Figure 4.3 – Methane hydrate formation and growth on a water droplet with a temperature gradient. The temperature gradient increased from $T_{\mathrm{L}} = 273.7$ K (left) to $T_{\mathrm{H}} = 277.7$ K (right). $p = 4$ MPa, $T_{\mathrm{HLV}} = 277.5$ K. (a) Water droplet before hydrate formation. (b) Initial growth points floated to the center of the droplet. (c-d) Continued growth of hydrate film, red circles show formation of single crystals ahead of the growth front inside the water phase. (e) The single crystal attached to the polycrystalline hydrate film growth front. (f) Hydrate film reaches to the high driving force end side of the droplet boundary. (g) Continued hydrate growth towards the low driving force end. (h) Droplet is completely covered by hydrate.

The hydrate growth-front then advanced rapidly towards the high driving force end and slowly towards the low driving force end. Once the hydrate film reached the periphery of the droplet on the high driving force end, the crystal started to propagate onto the sapphire substrate outside the original water boundary (halo). This halo effect on the high driving force end occurred before the droplet was completely covered with hydrate.

Hydrate crystal size decreased with the increasing subcooling. Figure 4.4 shows the relationship between the driving force and the crystal morphology. The crystal habit transitioned from small tightly packed grains near the high driving force end to large faceted crystals as the driving force decreased towards the low driving force end.

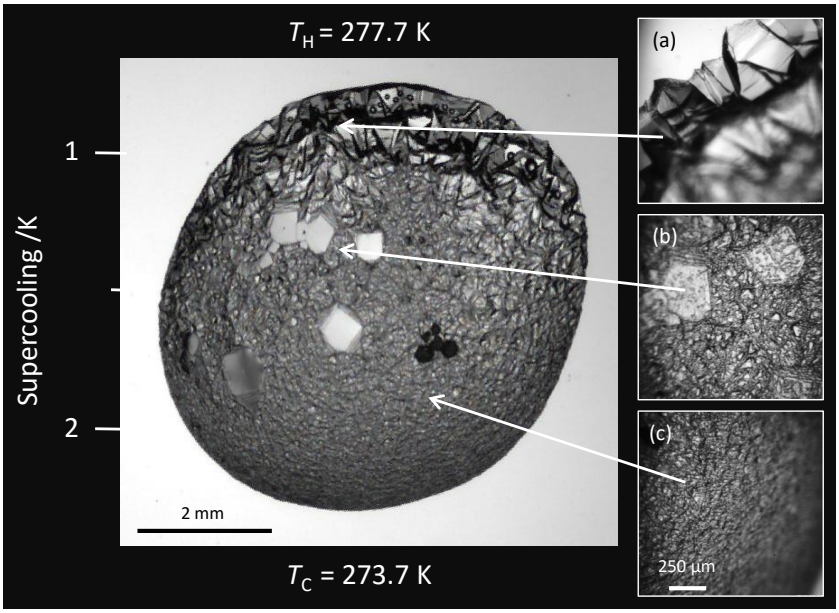

Figure 4.4 – Details of methane hydrate morphology on a water droplet with an applied temperature gradient. $p = 4$ MPa, $T_{\mathrm{L}} = 273.7$ K, $T_{\mathrm{H}} = 277.7$ K, and $T_{\mathrm{HLV}} = 277.5$ K. (a) Big faceted crystals. (b) Crystal granules and large single crystals in the film. (c) Smaller crystal granules and a smoother hydrate film.

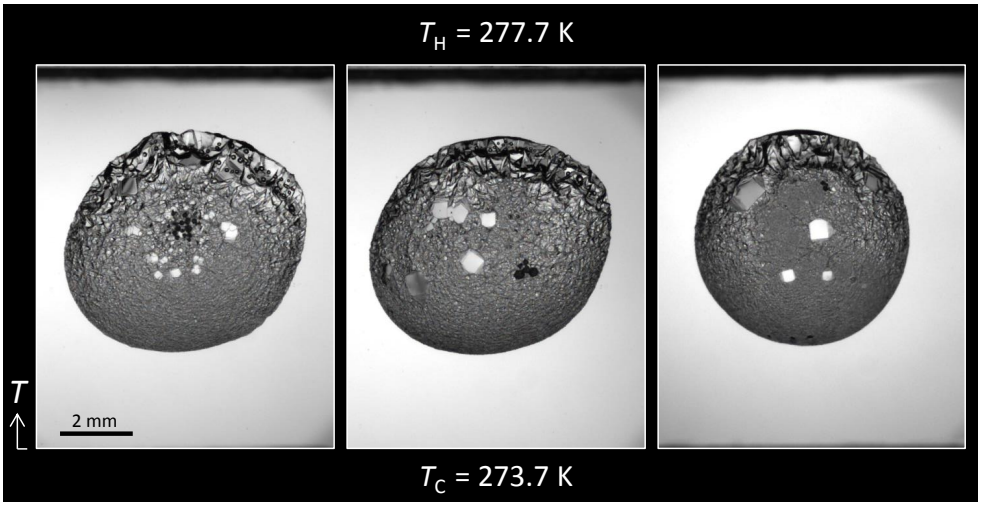

Figure 4.5 – Replicates of methane hydrate formed on a water droplet with an applied temperature gradient. $p = 4$ MPa, $T_C = 273.7$ K, $T_H = 277.7$ K, and $T_{HLV} = 277.5$ K.

Figure 4.5 shows the reproducibility for methane hydrate crystal habit when formed under a constant temperature gradient.

4.1.2 Water + CH_4 + ethylene glycol ($w_{EG} = 10\%$)

Uniform surface temperature

Figure 4.6 shows a hydrate formation sequence, at uniform surface temperature, from an aqueous solution containing a mass fraction of 10% ethylene glycol (EG). Hydrate nucleated at random points in the droplet and subsequently floated to the center of the droplet. These initial growth points grew into a polycrystalline hydrate crust that covered the entire surface of the droplet. After complete coverage of the droplet surface by the crystal, a smooth and thin hydrate film started to propagate outside the original water boundary (halo). As the halo advanced away from the center of the droplet, the crystal habit transitioned to a polygonal morphology.

Figure 4.7 presents magnified views of hydrate morphology formed in the presence of ethylene glycol at uniform surface temperature. Higher driving forces produced smaller grains (Figure 4.8) than lower driving forces.

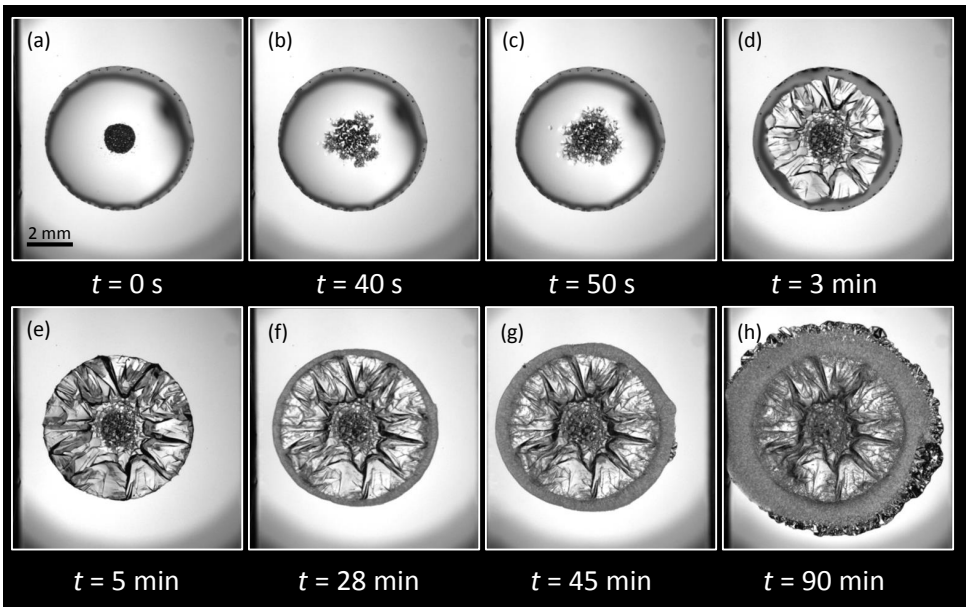

Figure 4.6 – Methane hydrate formation and growth on an aqueous EG solution droplet at constant temperature. w_{EG} = 10%, p = 5.99 MPa, T = 276.8 K (ΔT_{sub} = 2.9 K). (a) Water droplet before hydrate formation. (b) Initial growth points floating towards to the center of the droplet. (c-d) Continued growth from initial growth points. (e) Droplet is completely covered by hydrate film. (f-g) Halo propagating radially outside of the droplet boundary. (g) A transition in halo crystal growth behavior.

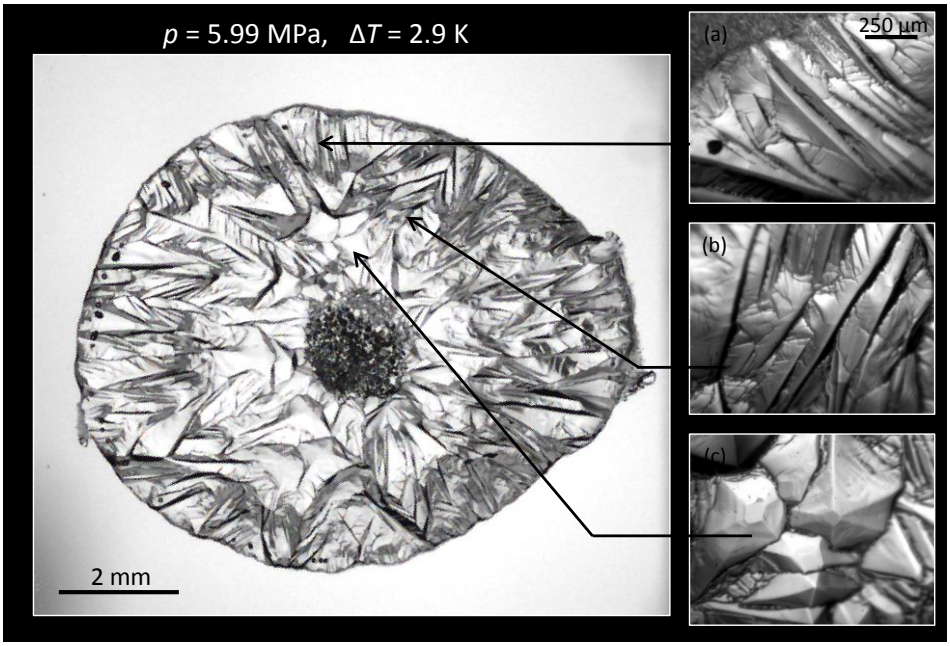

Figure 4.7 – Methane hydrate formed on an aqueous EG solution droplet at uniform surface temperature. $w_{\mathrm{EG}} = 10\%$, $p = 5.99$ MPa, $T = 276.8$ K ($\Delta T_{\mathrm{sub}} = 2.9$ K). (a) Halo propagation from the droplet boundary. (b) Crystal growth inside the droplet boundary, but far from initial growth points. (c) Individual crystal geometry grown from initial growth points.

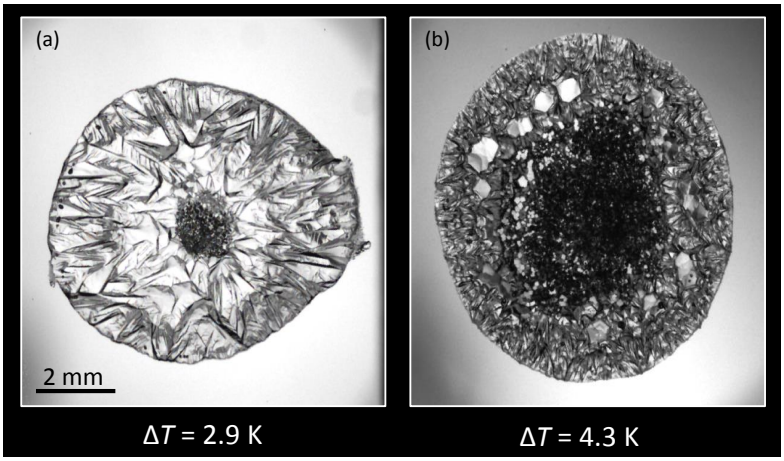

Figure 4.8 – Methane hydrate formed on an aqueous EG solution droplet at uniform surface temperature. (a) $w_{\mathrm{EG}} = 10\%$, $p = 5.99$ MPa, $T = 276.8$ K ($\Delta T_{\mathrm{sub}} = 2.9$ K). (b) $w_{\mathrm{EG}} = 10\%$, $p = 6.53$ MPa, $T = 276.2$ K ($\Delta T_{\mathrm{sub}} = 4.3$ K).

Constant temperature gradient

A sequence of methane hydrate growth on an aqueous EG solution droplet, subject to a temperature gradient, is shown in Figure 4.9. The crystal nucleated at random points within the droplet and moved towards the center of the droplet. The hydrate growth-front advanced faster toward the high driving force end than toward the low driving force end of the slide. Halo growth started from the high driving force end of the slide after the hydrate front had reached the droplet boundary, but before complete coverage of the droplet by the hydrate layer. The halo crystal habit transitioned from smooth to polygonal morphology as the halo advanced away from the center of the droplet. Furthermore, the size of hydrate crystals in the hydrate halo decreased with increased subcooling (Figure 4.9 and Figure 4.10).

Figure 4.10 shows details of the effect of driving force on hydrates formed from aqueous EG solutions. The hydrate film transitioned from a feather-like appearance near the high driving force end to a faceted morphology towards the low driving force end. Halo growth occurred from both low and high driving force sides of the slide. Dark channels were observed between grain boundaries across the hydrate film.

The reproducibility of the observed crystal growth behavior and hydrate mor-

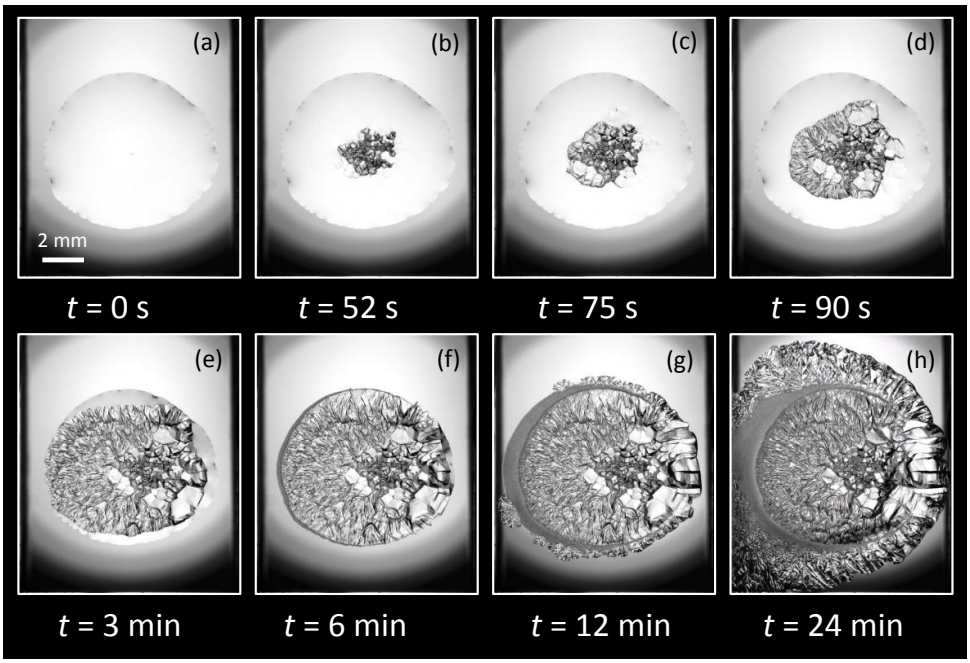

Figure 4.9 – Methane hydrate formation and growth on an aqueous EG solution droplet subject to a temperature gradient. The temperature gradient increased from $T_{\mathrm{L}} = 275.0$ K (left) to $T_{\mathrm{H}} = 279.0$ K (right). $w_{\mathrm{EG}} = 10\%$, $p = 5.99$ MPa, $T_{\mathrm{HLV}} = 279.7$ K. (a) Aqueous EG solution droplet before hydrate formation. (b) Initial growth points moving to the center of the droplet. (c-d) Continued growth of hydrate film. (e) Hydrate film reaches the high driving force end side of the droplet boundary. (f) Initial hydrate halo propagation from the high driving force end of the droplet boundary. (g) Polygonal hydrate halo and halo propagation toward the low driving force end. (h) Droplet is completely covered by hydrate.

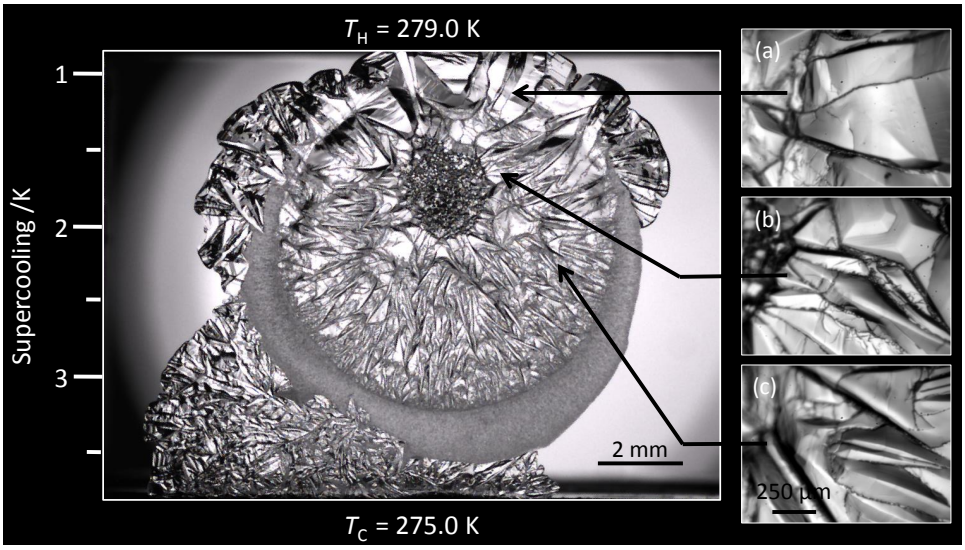

Figure 4.10 – Detail of methane hydrate morphology on an aqueous EG solution droplet subject to a temperature gradient. $w_{\mathrm{EG}} = 10\%$, $p = 5.99$ MPa, $T_{\mathrm{L}} = 275.0$ K, $T_{\mathrm{H}} = 279.0$ K, and $T_{\mathrm{HLV}} = 279.7$ K. (a) Large faceted crystals at the droplet boundary. (b) Small faceted crystals inside the droplet. (c) Smaller crystals.

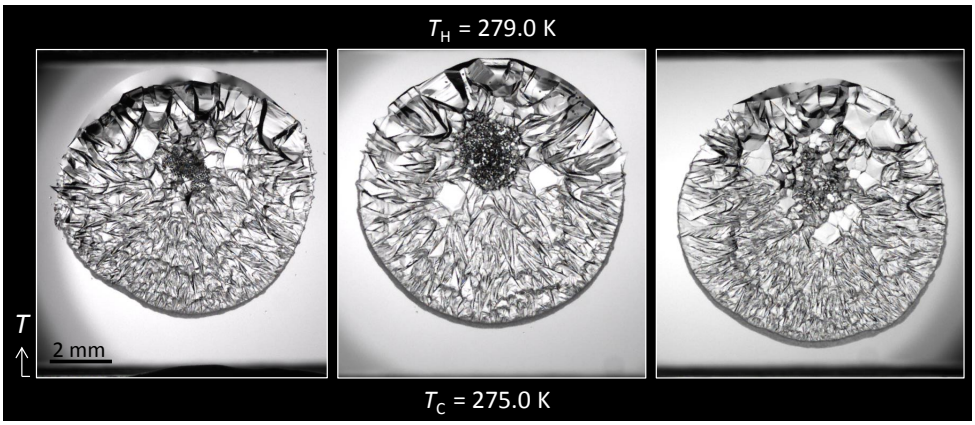

Figure 4.11 – Replicates of methane hydrate formation from an aqueous EG solution droplet subject to a temperature gradient. $w_{\mathrm{EG}} = 10\%$, $p = 5.99$ MPa, $T_{\mathrm{C}} = 275.0$ K, $T_{\mathrm{H}} = 279.0$ K, and $T_{\mathrm{HLV}} = 279.7$ K.

phology is shown in Figure 4.11.

4.1.3 Water + CH_4 + sodium chloride ($w_{\mathrm{NaCl}} = 5.44\%$)

Uniform surface temperature

Figure 4.12 shows a hydrate formation sequence, at uniform surface temperature, from an aqueous solution containing a mass fraction of 5.44% NaCl. Initial crystallites appeared at random locations within the droplet, and subsequently floated towards the center of the droplet. These initial growth points grew into a polycrystalline hydrate film that covered the entire surface of the droplet. After complete hydrate coverage of the droplet surface, a thin halo started to form outside the original water boundary. Approximately an hour after complete hydrate coverage of the droplet, hydrate dissociation was observed at random points inside the droplet boundary.

As shown in Figure 4.13 the hydrate film smoothed out with increasing driving force. Figure 4.14 and Figure 4.15 show magnified views of hydrate morphology at two different driving forces. As the hydrate film advanced away from the center of the droplet, a small increment in the size of individual hydrate crystals was observed. Lower driving force produces bigger grains of hydrate than high driving force. Large crystals were evident in the hydrate film.

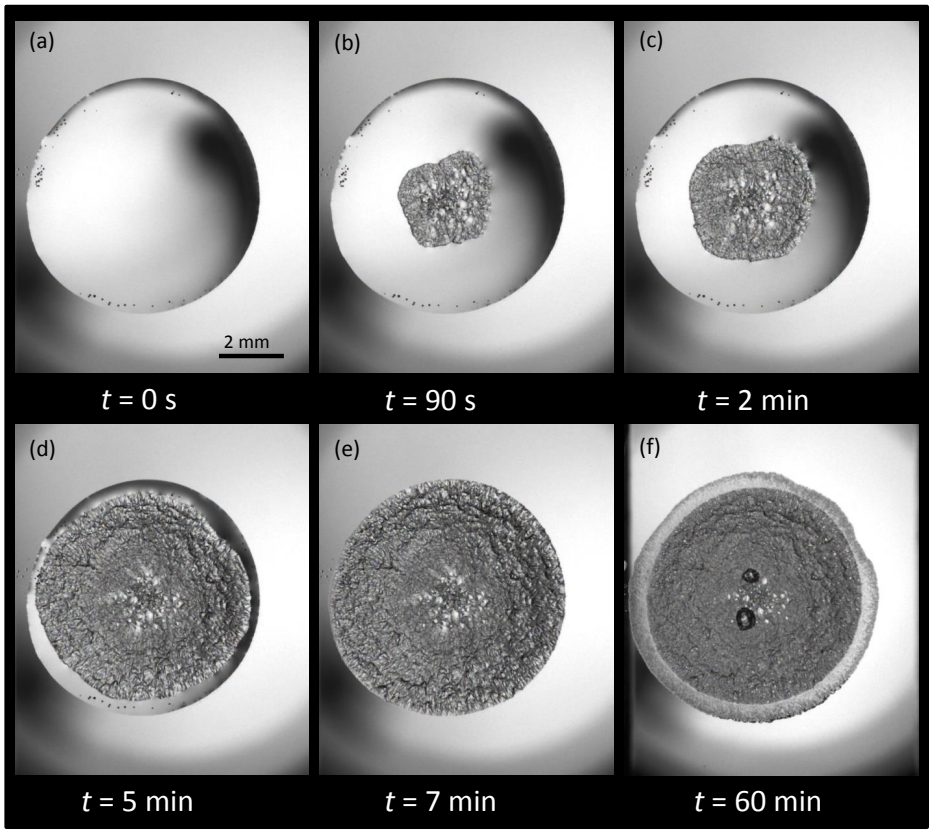

Figure 4.12 – Methane hydrate formation from an aqueous NaCl solution droplet maintained at uniform constant temperature. $w_{\mathrm{NaCl}} = 5.44\%$, $p = 5.39$ MPa, $T = 275.5$ K ($\Delta T_{\mathrm{sub}} = 2.1$ K). (a) Before hydrate formation. (b) Hydrate growth after nucleation. (c-d) Continued growth from the droplet center. (e) Droplet is completely covered by the hydrate film. (f-g) Halo propagation outside the droplet boundary and partial hydrate dissociation inside the droplet boundary

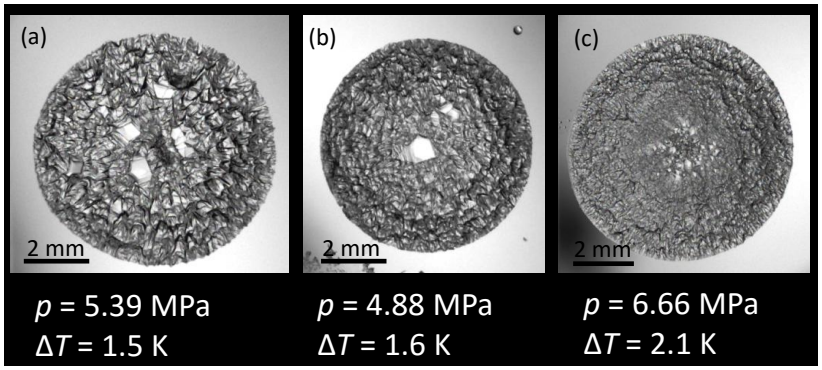

Figure 4.13 – Methane hydrate formed from an aqueous NaCl solution droplet maintained at uniform surface temperature. (a) $w_{\mathrm{NaCl}} = 5.44\%$, $p = 5.39$ MPa, $T = 276.1$ K ($\Delta T_{\mathrm{sub}} = 1.5$ K). (b) $w_{\mathrm{NaCl}} = 5.44\%$, $p = 4.88$ MPa, $T = 275.1$ K ($\Delta T_{\mathrm{sub}} = 1.6$ K). (c) $w_{\mathrm{NaCl}} = 5.44\%$, $p = 6.66$ MPa, $T = 277.1$ K ($\Delta T_{\mathrm{sub}} = 2.1$ K).

Constant temperature gradient

Figure 4.16 presents a typical sequence of hydrate formation on an aqueous NaCl solution droplet with a temperature gradient. Initially, crystallites grew into a hydrate film that advanced rapidly towards the high driving force end and slowly towards the low driving force end. Once the hydrate film reached the droplet boundary near the high driving force end, a halo started to propagate outside of the original water boundary.

Crystal size increased toward the low driving force side. Unexpectedly, crystal size also increased toward the periphery of the droplet along an isotherm (red circles in Figure 4.16). Furthermore, crystal growth eventually stopped completely and a section of the droplet remained in the liquid state.

Figure 4.17 shows the effect of driving force on gas hydrates formed on a droplet subject to a temperature gradient. The hydrate appearance transitioned from a granular film near the high driving force end to faceted crystals towards the low driving force end. The size of the hydrate crystals also decreased with increasing ΔT_{sub}.

Figure 4.18 shows the reproducibility of the crystal growth behavior and hydrate morphology.

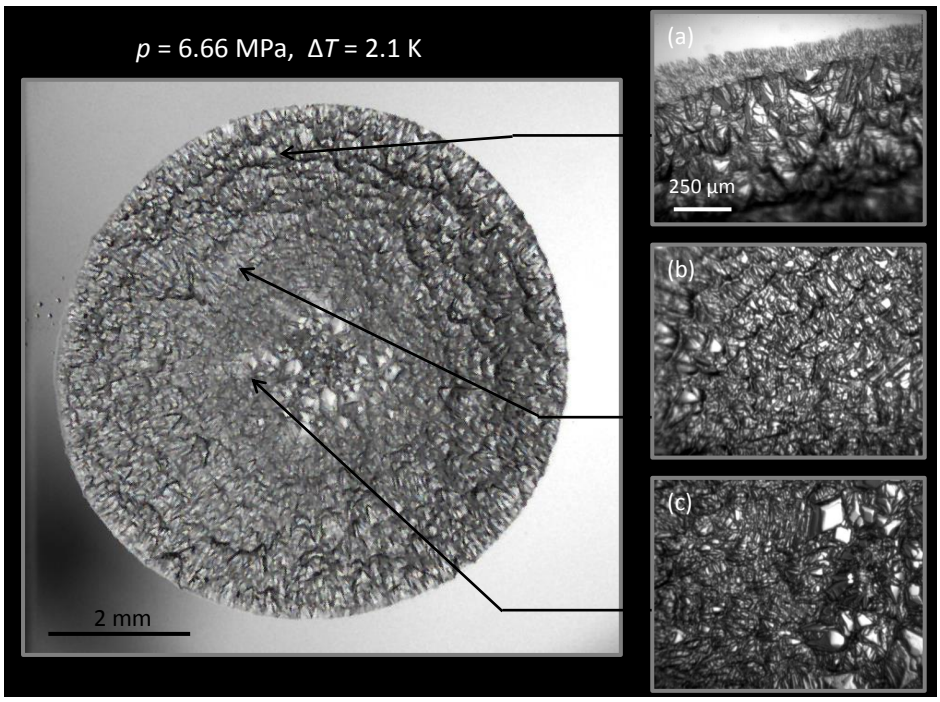

Figure 4.14 – Methane hydrate formed from an aqueous NaCl solution droplet maintained at uniform surface temperature. $w_{\mathrm{NaCl}} = 5.44\%$, $p = 6.66$ MPa, $T = 277.1$ K ($\Delta T_{\mathrm{sub}} = 2.1$ K). (a) Halo propagation from the droplet boundary. (b) Crystal growth inside the droplet boundary. (c) Large single crystals in the hydrate film.

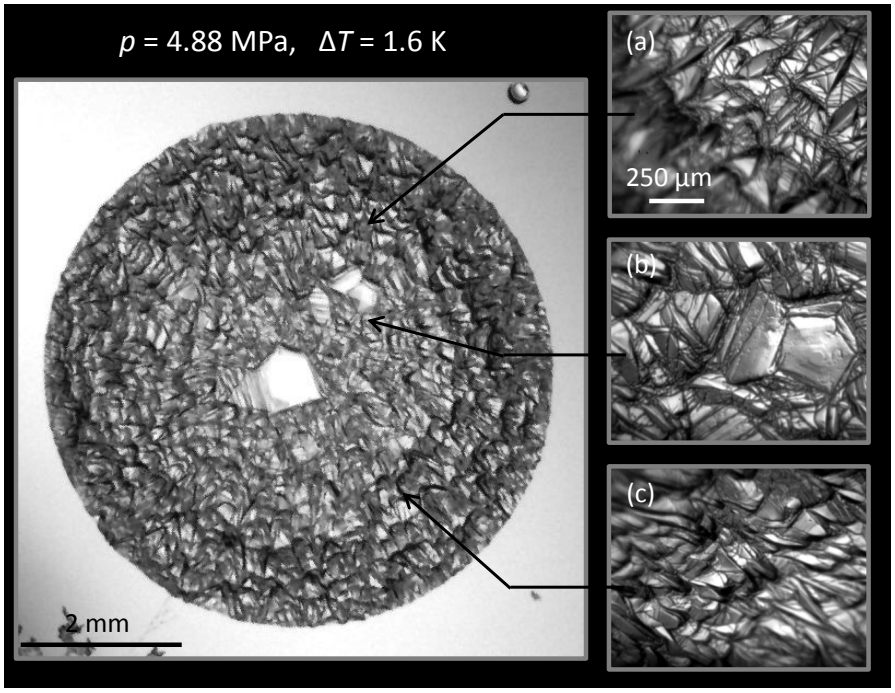

Figure 4.15 – Methane hydrate formed from an aqueous NaCl solution droplet maintained at uniform surface temperature. $w_{\mathrm{NaCl}} = 5.44\%$, $p = 4.88$ MPa, $T = 275.1$ K ($\Delta T_{\mathrm{sub}} = 1.6$ K). (a) Granular crystals. (b) Large single crystals in the hydrate film. (c) Granular crystals.

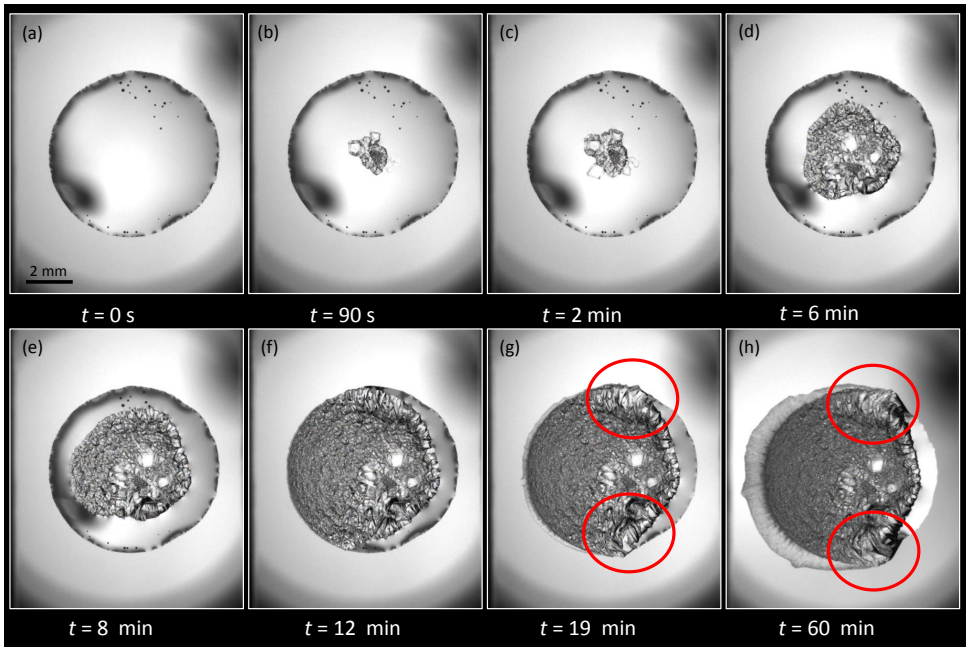

Figure 4.16 – Methane hydrate formation from an aqueous NaCl solution droplet, subject to a temperature gradient. The temperature gradient increased from $T_{\mathrm{L}} = 274.4$ K (left) to $T_{\mathrm{H}} = 278.4$ K (right). $w_{\mathrm{NaCl}} = 5.44\%$, $p = 5.39$ MPa, $T_{\mathrm{HLV}} = 277.6$ K. (a) Aqueous NaCl solution droplet before hydrate formation. (b) Initial growth points moving towards the center of the droplet. (c-e) Continued growth from the center of the droplet. (f) Hydrate film reaches the high driving force end of the droplet. (g) Hydrate halo propagation from the high driving force end of the droplet. (h) A section of the droplet does not convert to hydrate. Red circles highlight the change in crystal size after the hydrate reached the periphery of the droplet.

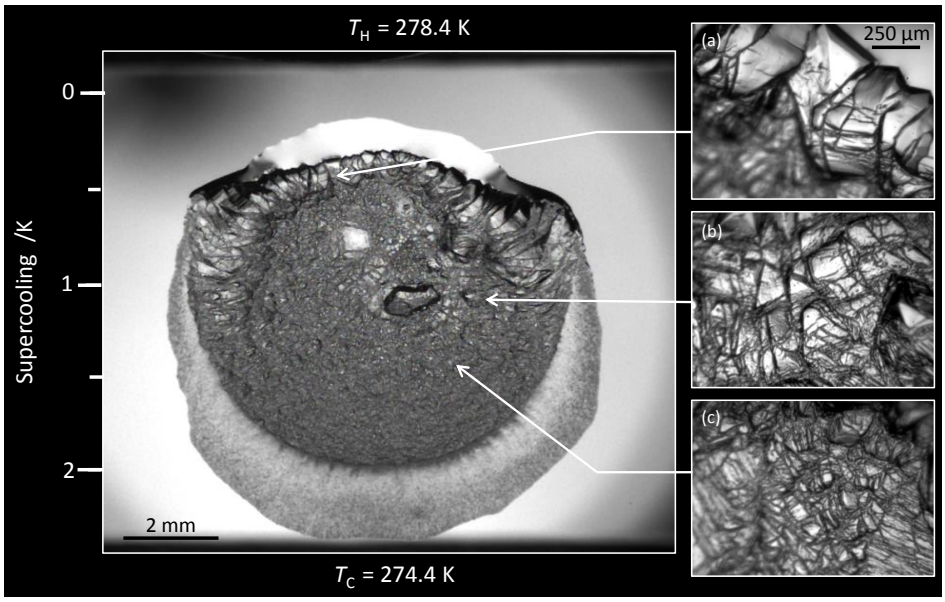

Figure 4.17 – Detail of methane hydrate morphology on an aqueous NaCl solution droplet, subject to a temperature gradient. $w_{\mathrm{NaCl}} = 5.44\%$, $p = 5.39$ MPa, $T_{\mathrm{L}} = 274.4$ K, $T_{\mathrm{H}} = 278.4$ K, and $T_{\mathrm{HLV}} = 277.6$ K. (a) Big faceted crystals. (b) Granular crystals. (c) Smaller granular crystals.

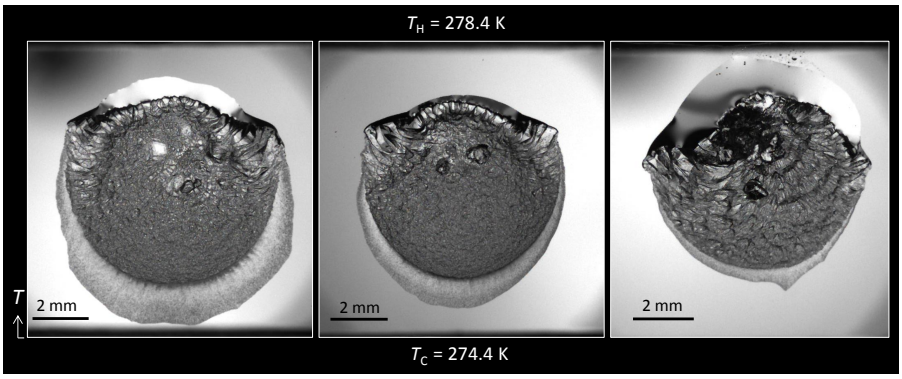

Figure 4.18 – Replicates of methane hydrate formed on an aqueous NaCl solution droplet, subject to a temperature gradient. $w_{\mathrm{NaCl}} = 5.44\%$, $p = 5.39$ MPa, $T_{\mathrm{C}} = 274.4$ K, $T_{\mathrm{H}} = 278.4$ K, and $T_{\mathrm{HLV}} = 277.6$ K.

4.1.4 Water + CH_4 + polyvinylpyrrolidone ($w_{PVP} = 0.1\%$)

Uniform surface temperature

Figure 4.19 shows a hydrate formation sequence, at uniform surface temperature, from an aqueous solution containing a mass fraction of 0.1% polyvinylpyrrolidone (PVP). The hydrate nucleated on the droplet surface and grew as a thin film covering the water surface. Once the hydrate film covered the droplet surface, an almost imperceptible halo propagated outside of the original droplet boundary. As time progressed, the hydrate appeared to thicken and became wrinkled. Under high magnification, spherulites composed of radiating little beads were observed (Figure 4.20).

Constant temperature gradient

Figure 4.21 presents a sequence of hydrate formation from an aqueous PVP solution droplet, subject to a temperature gradient. Initial growth points appeared at random locations on the surface of the droplet. Hydrates grew radially from the initial growth points until the whole droplet surface was covered with a clathrate film. The hydrate front advanced rapidly towards the high driving force end and slowly towards the low driving force end. Once hydrate film covered the entire droplet surface, a thin hydrate halo extends outside of the original water boundary. Inside the droplet, a thin and smooth hydrate layer covered the droplet surface. This hydrate layer thickened with time (based on translucency) and developed a wrinkled appearance.

Figure 4.22 shows magnified views of hydrate formed from aqueous PVP solution, subject to a temperature gradient. Surprisingly, driving force appeared to have no effect on the clathrate crystal habit. A wrinkled surface composed of spherulites was observed across the entire droplet surface.

Replicates of methane hydrate morphology, crystallized from aqueous PVP solution droplets subject to a temperature gradient are shown in Figure 4.23.

4.1.5 Water + CH_4 + Tetra-n-butylammonium bromide ($w_{TBAB} = 0.5\%$)

At low pressure ($p = 4$ MPa)

Uniform surface temperature

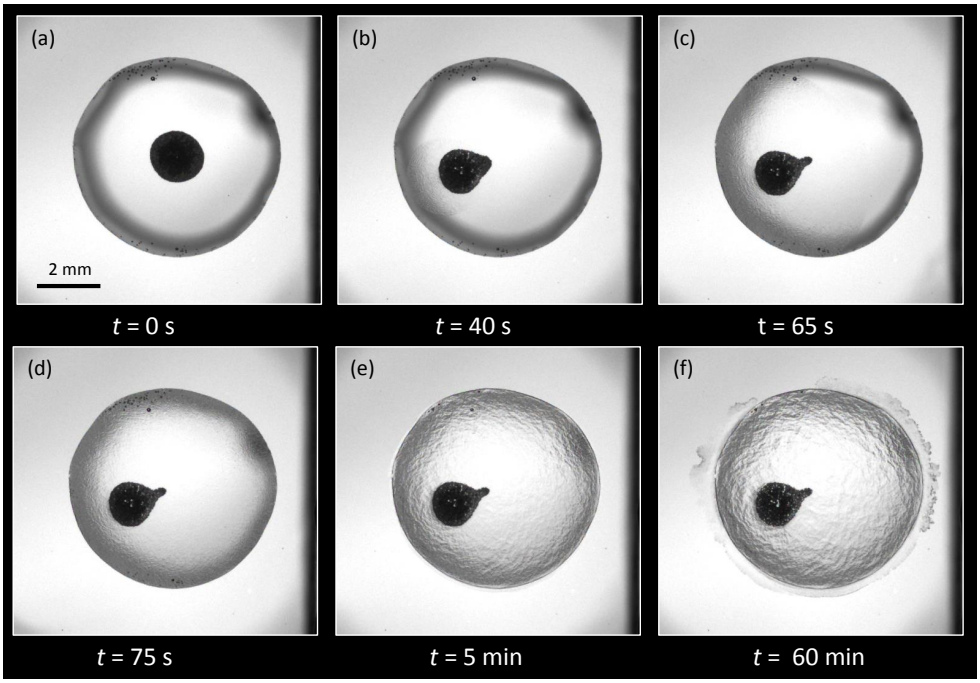

Figure 4.19 – Methane hydrate formation and growth on an aqueous PVP solution droplet at constant temperature. $w_{\mathrm{PVP}} = 0.1\%$, $p = 6.13$ MPa, $T = 275.2$ K ($\Delta T_{\mathrm{sub}} = 6.2$ K). (a) Aqueous PVP solution droplet before hydrate formation. (b) Initial hydrate growth. (c) Continued hydrate film growth. (d) Droplet is completely covered by a thin and smooth hydrate film. (e) Halo propagation outside of the original water boundary. (f) Continued halo propagation outside the droplet and wrinkled hydrate film inside the droplet boundary.

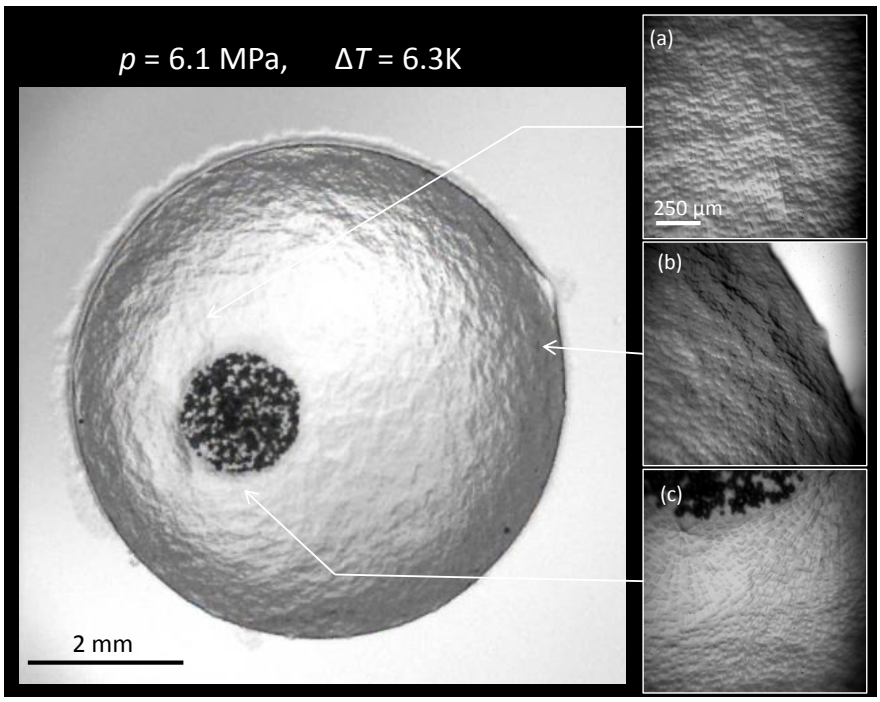

Figure 4.20 – Methane hydrate formed on an aqueous PVP solution droplet at uniform surface temperature. $w_{\mathrm{PVP}} = 0.1\%$, $p = 6.10$ MPa, $T = 275.5$ K ($\Delta T_{\mathrm{sub}} = 6.2$ K). (a) Hydrate growth in middle of the droplet. (b) Boundary between the water droplet and the sapphire slide. (c) Spherulitic Hydrate growth from initial growth points.

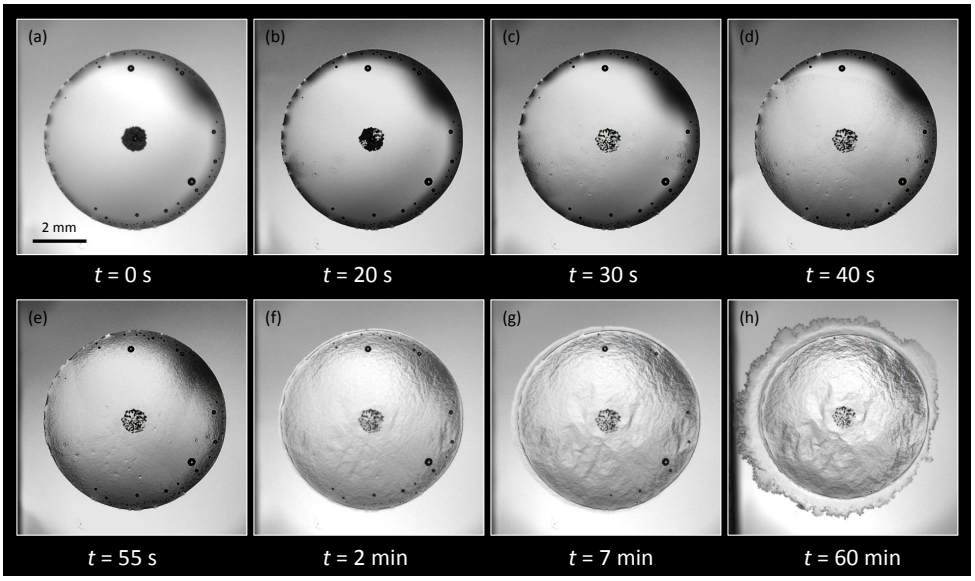

Figure 4.21 – Methane hydrate formation on an aqueous PVP solution droplet subject to a temperature gradient. The temperature gradient increased from $T_{\mathrm{L}} = 273.7$ K (left) to $T_{\mathrm{H}} = 277.7$ K (right). $w_{\mathrm{PVP}} = 0.1\%$, $p = 6.13$ MPa, $T_{\mathrm{HLV}} = 281.4$ K. (a) Aqueous PVP solution droplet before hydrate formation. (b) Initial growth points. (c) Hydrate film reaches the high driving force end of the droplet boundary. (d) Continued hydrate film growth towards low driving force end of the droplet boundary. (e) Droplet is completely covered by thin and smooth hydrate film. (f) Initial halo propagation. (g) Continued halo propagation. (h) Wrinkled hydrate film inside the droplet boundary.

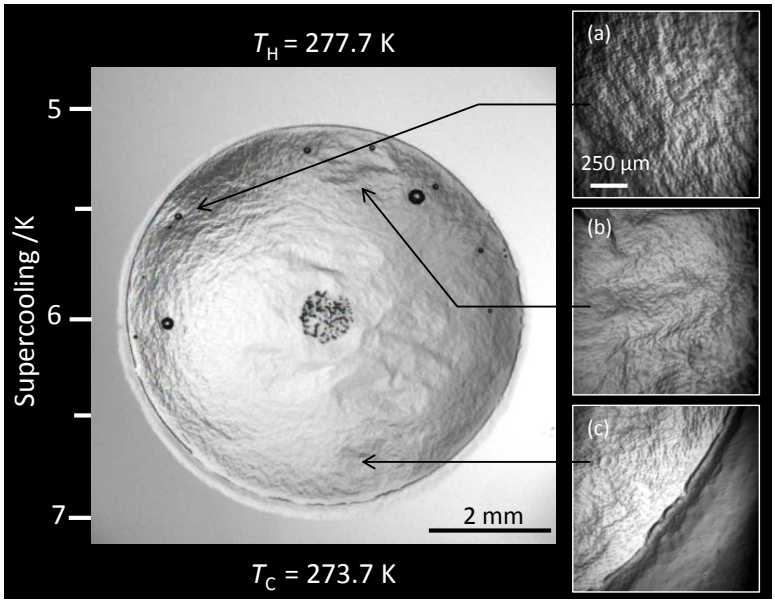

Figure 4.22 – Detail of methane hydrate morphology from an aqueous PVP solution droplet with an applied temperature gradient. $w_{\mathrm{PVP}} = 0.1\%$, $p = 6.13$ MPa, $T_{\mathrm{L}} = 273.7$ K, $T_{\mathrm{H}} = 277.7$ K, and $T_{\mathrm{HLV}} = 281.4$ K. (a-b) Wrinkled hydrate film. (c) Boundary between the aqueous solution droplet and the sapphire substrate.

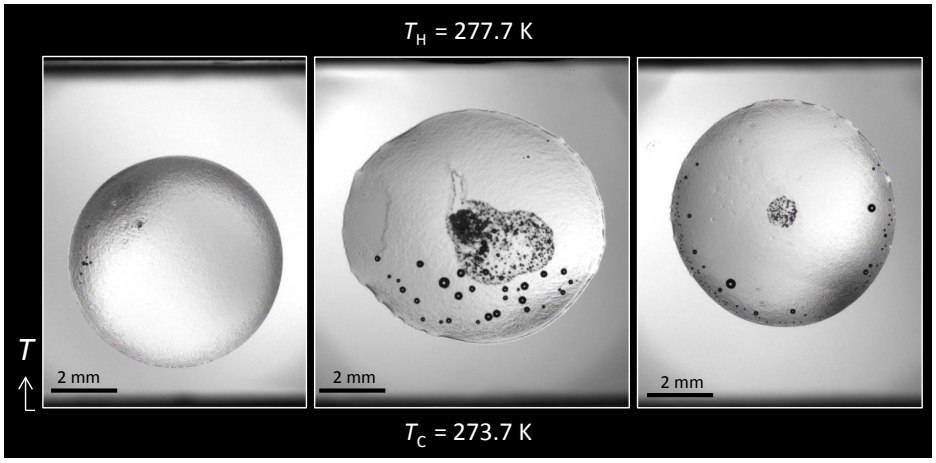

Figure 4.23 – Replicates of methane hydrate formed from an aqueous PVP solution droplet with an applied temperature gradient. $w_{\mathrm{PVP}} = 0.1\%$, $p = 6.13$ MPa, $T_{\mathrm{C}} = 273.7$ K, $T_{\mathrm{H}} = 277.7$ K, and $T_{\mathrm{HLV}} = 281.4$ K.

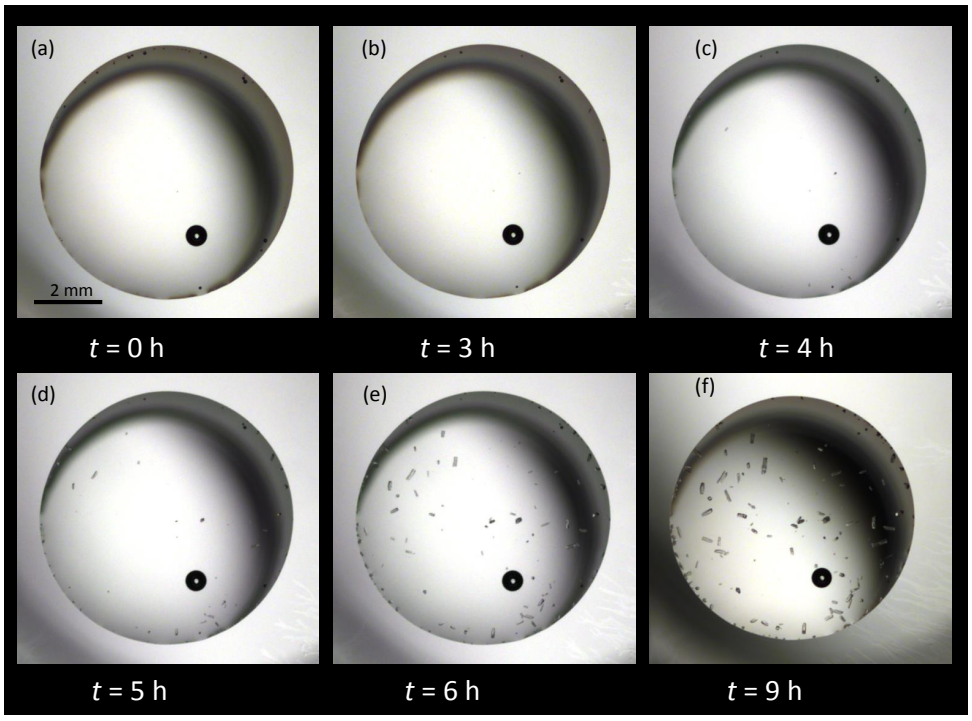

Figure 4.24 – Methane hydrate formation and growth on an aqueous TBAB solution droplet at constant temperature. $w_{\mathrm{TBAB}} = 0.5\%$, $p = 4.0$ MPa, $T = 274.5$ K. (a) Aqueous TBAB solution droplet before hydrate formation. (b-c) Initial hydrate growth points. (d-f) Continued growth from the initial growth points and more initial growth points appearing.

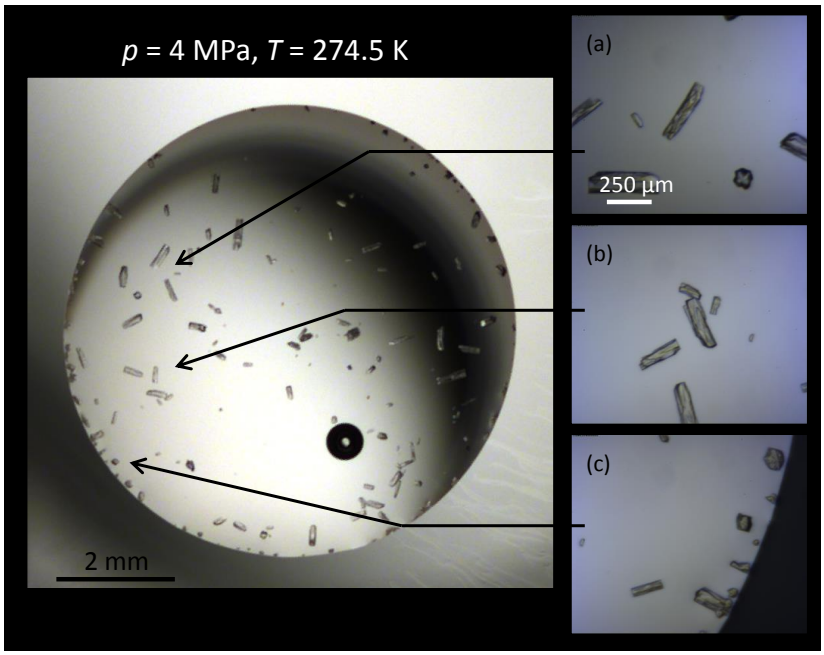

Figure 4.25 – Methane hydrate formed on an aqueous TBAB solution droplet at uniform surface temperature. $w_{\mathrm{TBAB}} = 0.5\%$, $p = 4.0$ MPa, $T = 274.5$ K. (a-b) Hydrate crystals within the droplet. (c) Hydrate crystals at the periphery of the droplet.

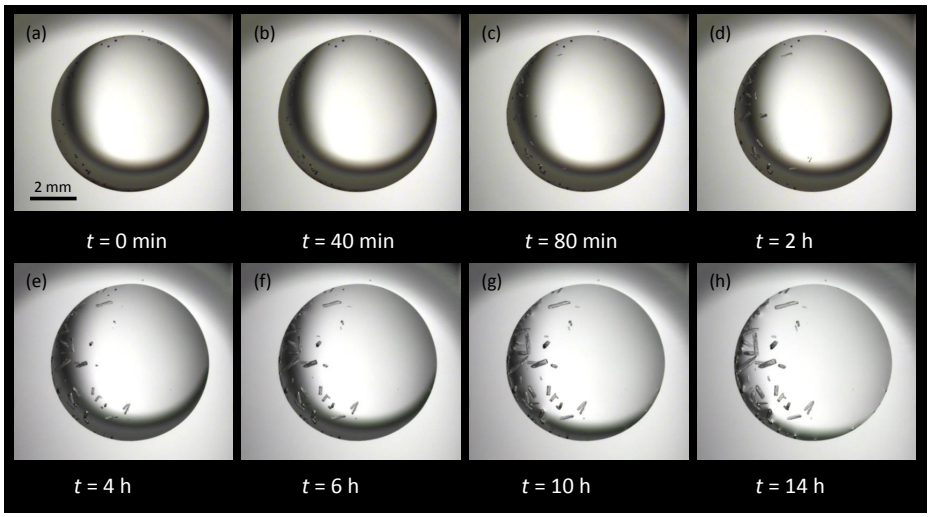

Figure 4.26 – Methane hydrate formation on an aqueous TBAB solution droplet, subject to a temperature gradient. The temperature gradient increased from $T_{\mathrm{L}} = 273.7$ K (left) to $T_{\mathrm{H}} = 277.7$ K (right). $w_{\mathrm{TBAB}} = 0.5\%$, $p = 4.0$ MPa. (a) Aqueous TBAB solution droplet before hydrate formation. (b-c) Initial hydrate growth points towards the high driving force end of the droplet boundary. (d-h) Continued growth from the initial growth points and more initial growth points appearing.

Figure 4.24 presents a sequence of hydrate formation on a Tetra-n-butylammonium bromide (TBAB) aqueous solution droplet kept at 4 MPa, and maintained at constant temperature. Initial growth points appeared at random points on the water droplet, and grew to form polygonal columnar crystals. These columnar crystals did not migrate from the initial growth location, and no agglomeration was observed. The number of crystals and their respective size increased with time. However, after approximately 10 hours no growth was observed. Figure 4.25 presents a detailed view of the hydrate crystals. The hydrate crystals on the surface of the droplet have polygonal columnar shape and large granular shape crystals on the periphery of the droplet.

Constant temperature gradient

Figure 4.26 presents sequential images of hydrate formation on an aqueous solution droplet containing a mass fraction of 0.5% TBAB. A temperature gradient was applied along the sapphire slide and maintained constant throughout the experiment. Initial growth was observed at arbitrary points but seemed to concentrate toward the colder side of the droplet. These crystallites grew

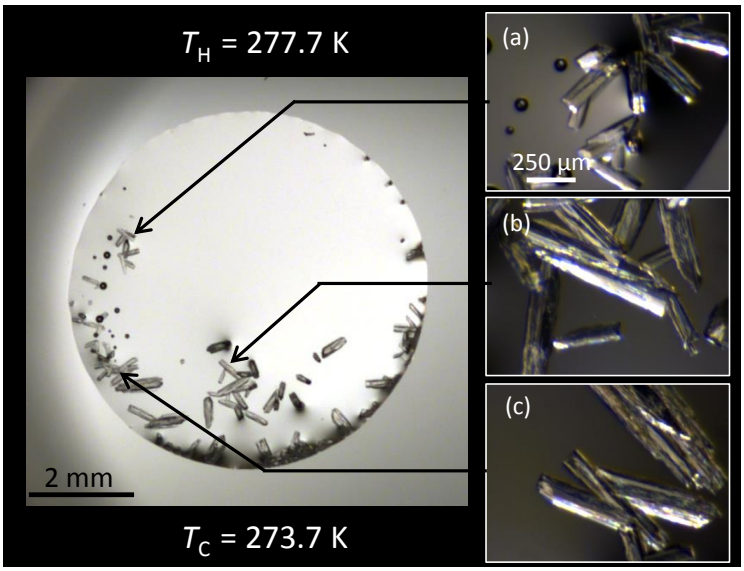

Figure 4.27 – Detailed view of methane hydrate morphology formed from aqueous TBAB solution droplet with an applied temperature gradient. w_{TBAB} = 0.5%, p = 4.0 MPa, T_{L} = 273.7 K, T_{H} = 277.7 K. (a-c) Enlarged view of columnar polygonal hydrate crystals.

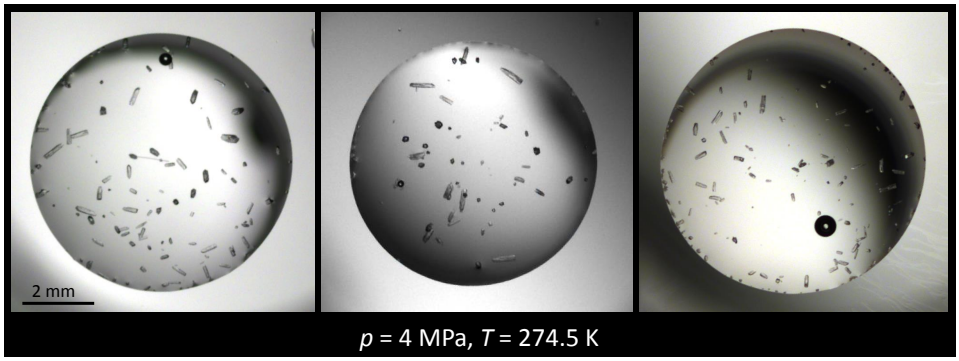

Figure 4.28 – Replicates of methane hydrate formed from aqueous TBAB solution droplets at 4 MPa, and maintained at uniform surface temperature. $w_{\mathrm{TBAB}} = 0.5\%$, $p = 4.0$ MPa, $T = 274.45$ K.

into polygonal columnar crystals. The number of crystals and their respective size decreased with decreasing driving force. No growth was observed above 275.5 K ($\Delta T_{\mathrm{sub}} = 2.2$ K measured with respect to simple methane hydrate). No hydrate agglomeration was observed, growth seemed to stop altogether 10 h after initial growth.

Replicates of semiclathrate hydrate of methane morphology, crystallized from aqueous TBAB solution droplet, subject to a uniform surface temperature are shown in Figure 4.28.

At high pressure ($p = 6.6$ MPa)

Uniform surface temperature

Figures 4.29 to 4.32 show sequences of hydrate formation from aqueous solution droplets containing a mass fraction of 0.5% TBAB. The surface temperature was uniform across the slide and maintained constant for the duration of the experiment. Initial growth points were observed at random points within the droplet. Dendritic crystals were observed in all sequences, but the overall aspect of the droplet was not found to be reproducible. Hydrate dendrites advanced on all the water surfaces until complete coverage of the original droplet was achieved. However, the time required for complete coverage of the droplet varied from 30 minutes (Figure 4.32) to 120 minutes (Figure 4.30).

Figures 4.29, 4.30 and 4.32 show the liquid phase being drawn toward the newly formed solid hydrate. The original water boundary can still be dis-

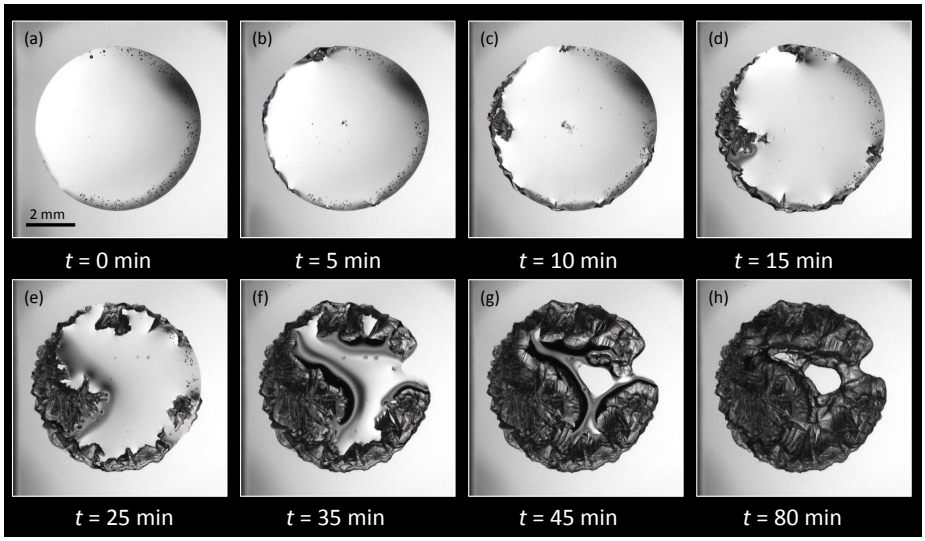

Figure 4.29 – Methane hydrate formation and growth on an aqueous TBAB solution droplet at constant temperature. $w_{\mathrm{TBAB}} = 0.5\%$, $p = 6.63$ MPa, $T = 275.2$ K. (a) Aqueous TBAB solution droplet before hydrate formation. (b-c) Initial hydrate growth points at the periphery and the center of the droplet. (c-g) Continued growth of hydrate from the initial growth points. (h) Complete droplet converted to hydrate.

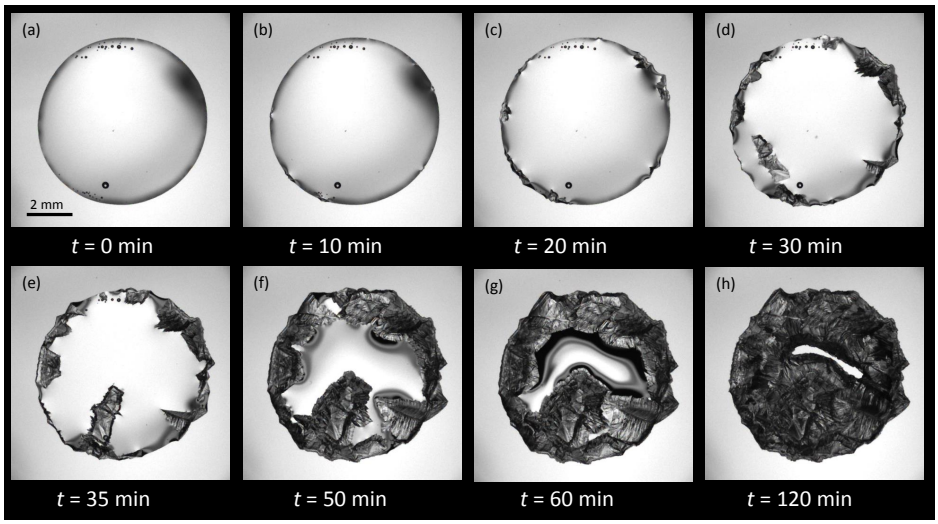

Figure 4.30 – Methane hydrate formation and growth on an aqueous TBAB solution droplet at constant temperature. $w_{\mathrm{TBAB}} = 0.5\%$, $p = 6.63$ MPa, $T = 275.2$ K. (a) Aqueous TBAB solution droplet before hydrate formation. (b) Initial hydrate growth points at the periphery of the droplet. (c-g) Continued dendritic growth of hydrate from the initial growth points towards the center of the droplet. (h) Complete droplet converted to hydrate.

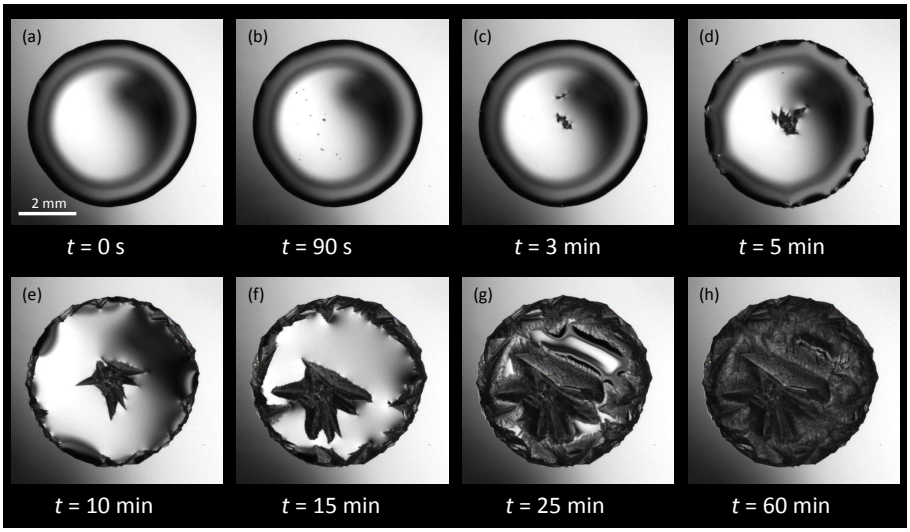

Figure 4.31 – Methane hydrate formation and growth on an aqueous TBAB solution droplet at constant temperature. $w_{\mathrm{TBAB}} = 0.5\%$, $p = 7.1$ MPa, $T = 275.2$ K. (a) Aqueous TBAB solution droplet before hydrate formation. (b) Initial hydrate growth points moving towards the center of the droplet. (c-d) More initial growth points at the periphery of the droplet. (e-g) Continued growth of hydrate from the initial growth points. (h) Complete droplet converted to hydrate.

cerned in Figure 4.29 and Figure 4.30, but was unnoticeable by the end of the sequence shown in Figure 4.32. No liquid movement was observed in one of the sequences (Figure 4.31). Magnified views of the crystals are shown in Figure 4.33.

The hydrate halo started to propagate on the sapphire surface, outside the original water boundary, after complete formation of the hydrate. Small dendritic halo growth after 5 h of complete hydrate formation is shown in Figure 4.34.

Constant temperature gradient

Figure 4.35 shows a sequence of hydrate formation from an aqueous solution containing a mass fraction of 0.5% TBAB. A temperature gradient was applied and maintained constant throughout the duration of the experiment. Nucleation occurred at random points within the droplet and at the periphery. Crystals that nucleated at the periphery of the droplet appeared to remain static, while those that began growth within the droplet tended to float to

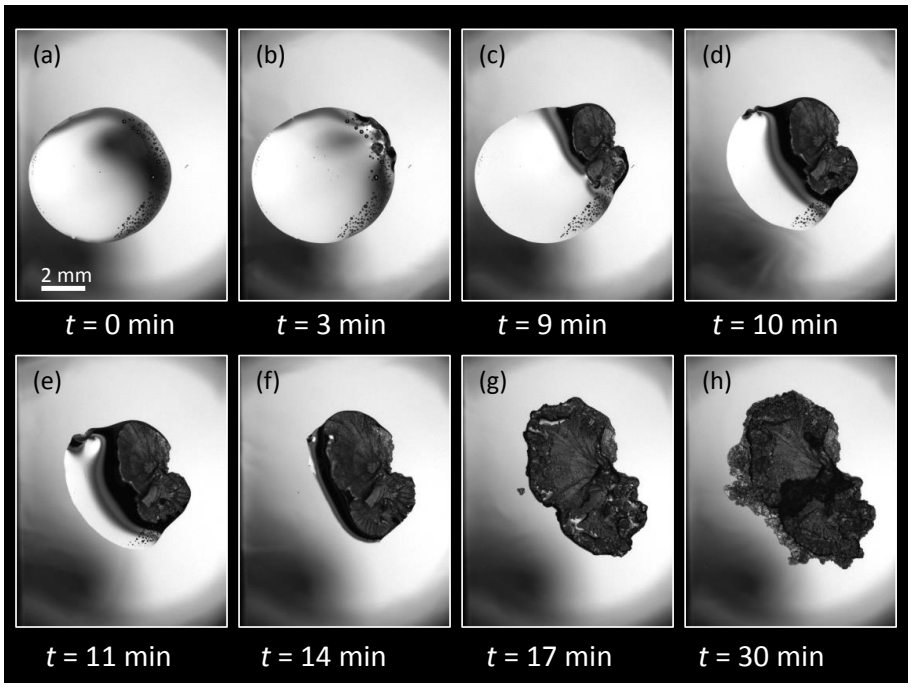

Figure 4.32 – Methane hydrate formation on an aqueous TBAB solution droplet at constant temperature. $w_{\mathrm{TBAB}} = 0.5\%$, $p = 6.63$ MPa, $T = 275.2$ K. (a) Aqueous TBAB solution droplet before hydrate formation. (b-c) Initial hydrate growth points only one side at the periphery of the droplet. (c-g) Continued dendritic growth, water is drawn to the growing crystal. (h) Complete droplet converted to hydrate.

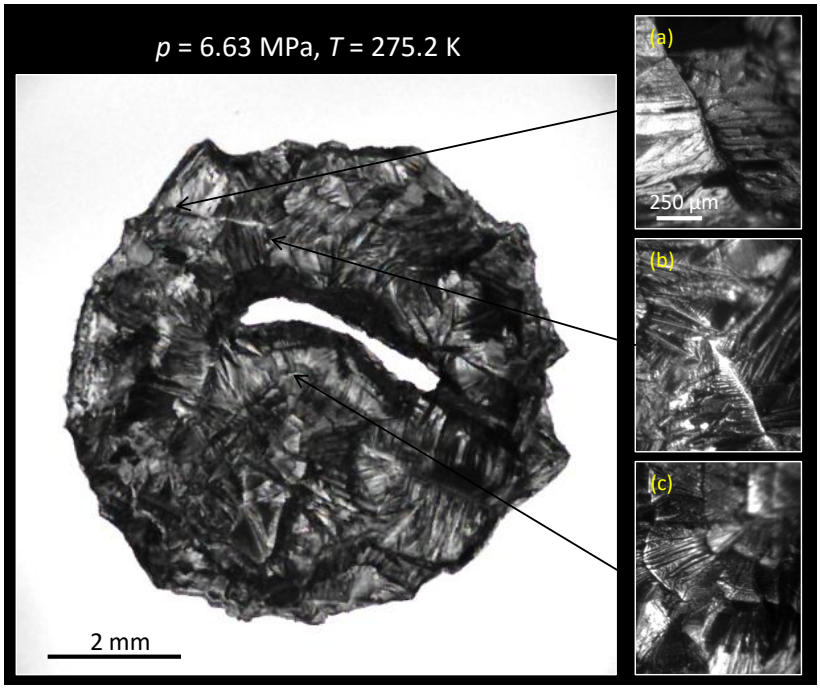

Figure 4.33 – Methane hydrate formed from an aqueous TBAB solution droplet at uniform surface temperature. $w_{\mathrm{TBAB}} = 0.5\%$, $p = 6.63$ MPa, $T = 275.2$ K. (a-c) Enlarged view of dendritic hydrates.

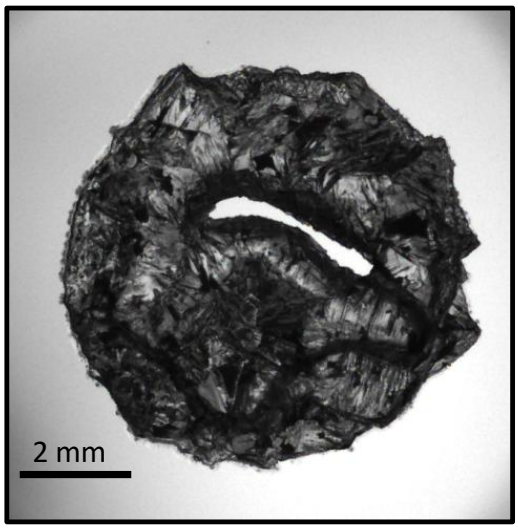

Figure 4.34 – Methane hydrate formed from an aqueous solution droplet containing TBAB ($w_{\mathrm{TBAB}} = 0.5\%$). The image was taken 5 h after complete coverage of the droplet by hydrate. An almost imperceptible halo appears on the periphery. $p = 6.63$ MPa, $T = 275.2$ K.

the center of the droplet. Water was found to be drawn toward the growing crystal, until the whole droplet converted to hydrate.

Figure 4.36 shows a detailed view of hydrate morphology under a temperature gradient. There appeared to be no significant change in crystal habit as a function of subcooling.

Figure 4.37 shows replicates of methane hydrate formed from aqueous TBAB solution droplets. Images correspond to the time of complete hydrate coverage of the droplet. Neither crystal morphology, nor rate of growth was reproducible. Formation sequences are not shown except for Figure 4.35. Similar to the uniform surface temperature experiments (Figures 4.29 to 4.32) the growth mechanism was unpredictable except for the fact that water seemed to be drawn toward the growing crystal.

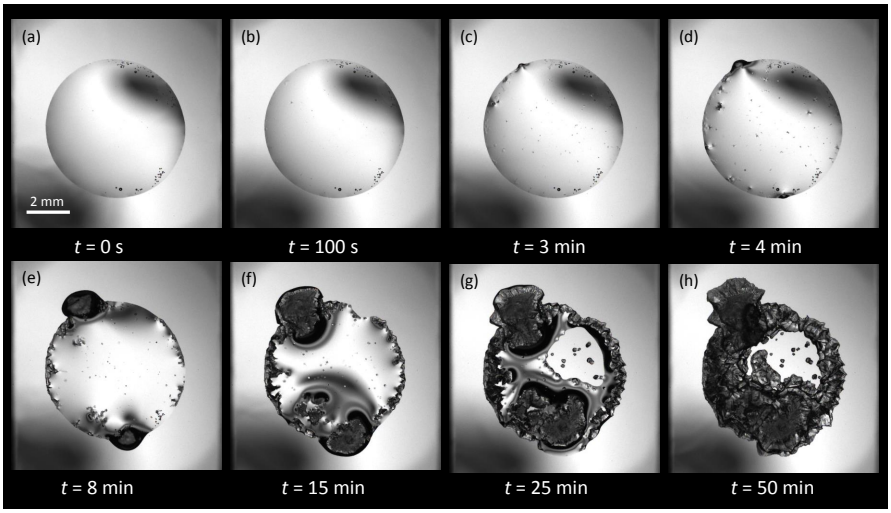

Figure 4.35 – Methane hydrate formation on an aqueous TBAB solution droplet, subject to a temperature gradient. The temperature gradient increased from $T_{\mathrm{L}} = 273.7$ K (left) to $T_{\mathrm{H}} = 277.7$ K (right). $w_{\mathrm{TBAB}} = 0.5\%$, $p = 6.63$ MPa. (a) Aqueous TBAB solution droplet before hydrate formation. (b-c) Initial hydrate growth points on the surface and at the periphery of the droplet. (d-g) Continued growth, water is drawn to the growing crystal. (h) Droplet completely converted into hydrate.

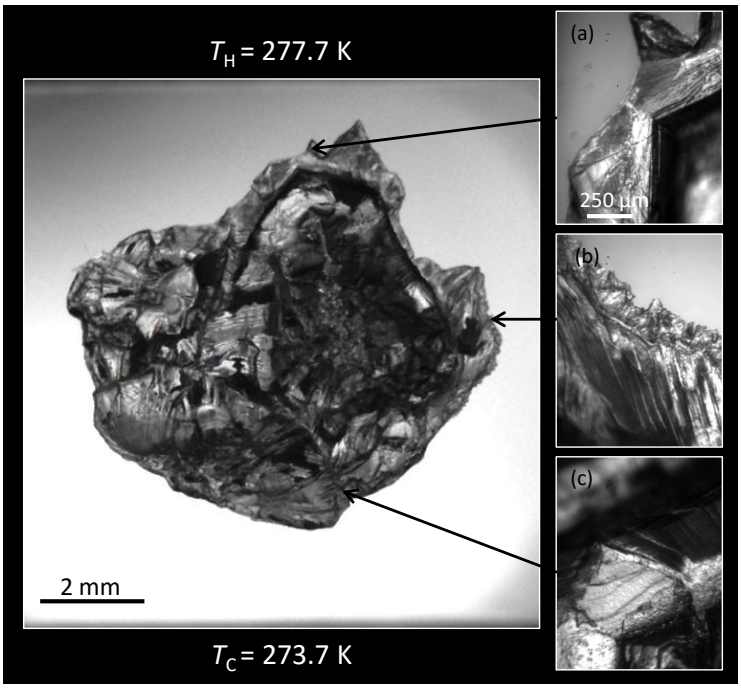

Figure 4.36 – Detailed view of methane hydrate morphology formed from an aqueous TBAB solution droplet with an applied temperature gradient. w_{TBAB} = 0.5%, p = 6.63 MPa, T_{L} = 273.7 K, T_{H} = 277.7 K. (a-b) Hydrate crystal at the periphery of the droplet. (c) Enlarged view of hydrate surface inside the droplet boundary.

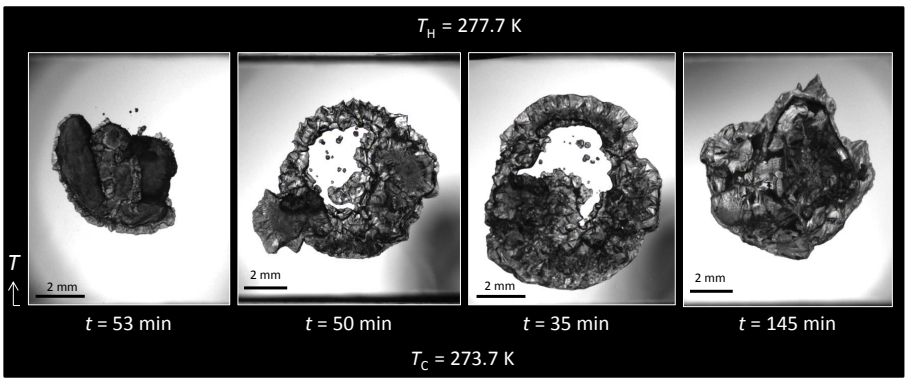

Figure 4.37 – Replicates of methane hydrate formed from aqueous TBAB solution droplets, subject to a temperature gradient. $w_{\mathrm{TBAB}} = 0.5\%$, $p = 6.63$ MPa, $T_{\mathrm{C}} = 273.7$ K, $T_{\mathrm{H}} = 277.7$ K.

4.2 Hydrate dissociation

4.2.1 Water + CH_4

Figure 4.38 shows a typical dissociation sequence of methane hydrate formed from pure water, using a temperature gradient along the slide at 4 MPa. The controlled hydrate dissociation method is described in Section 3.3.3. Before hydrate dissociation, the temperature gradient was set such that the hot side of the gradient was below the H-L-V equilibrium temperature at the experimental pressure. Afterward, the temperature on both sides of the stage was increased simultaneously with equal increments. Each step increase in temperature on both sides of the stage moved the position of H-L-V equilibrium temperature towards the cold side of the gradient (Figure 3.4 (c)). As a result, the hydrate was dissociated only in the region of the stage that was above the H-L-V equilibrium temperatures which enabled the observation of the H-L-V equilibrium interface on the surface of the droplet. The temperature on both sides of the gradient was maintained constant until the hydrate-water interface was stabilized. The interface was stabilized in less than 5 minutes for the hydrate formed from pure water. This procedure allowed us to obtain multiple H-L-V equilibrium points with a single experiment.

As hydrate dissociated, a clear interface between the water and the hydrate can be seen in Figure 4.38 (b-c). When the position of the interface corresponded to the position of the large size crystals in the hydrate film, the latter would dissociate completely, leaving dents in the interface corresponding to the size of the large crystals (Figure 4.38 (b)). And when the position of the interface corresponded to the position of smaller size grains in the hydrate film, as almost straight interface was observed (Figure 4.38 (c)).

4.2.2 Water + CH_4 + polyvinylpyrrolidone ($w_{PVP} = 0.1\%$)

Figure 4.39 shows a dissociation sequence of methane hydrate formed from an aqueous solution containing a mass fraction of 0.1% PVP using a temperature gradient, at 6.13 MPa. The hydrate-liquid phase interface shown in Figure 4.39 (b-c) was stabilized in 6.5 h. Remnant crystals were observed in the liquid phase region above the H-L-V equilibrium temperature, but as time progressed these remnant crystals dissociated. As can be seen in Figure 4.39 (b-c), these remnant crystals were only stable near the hydrate-liquid interface.

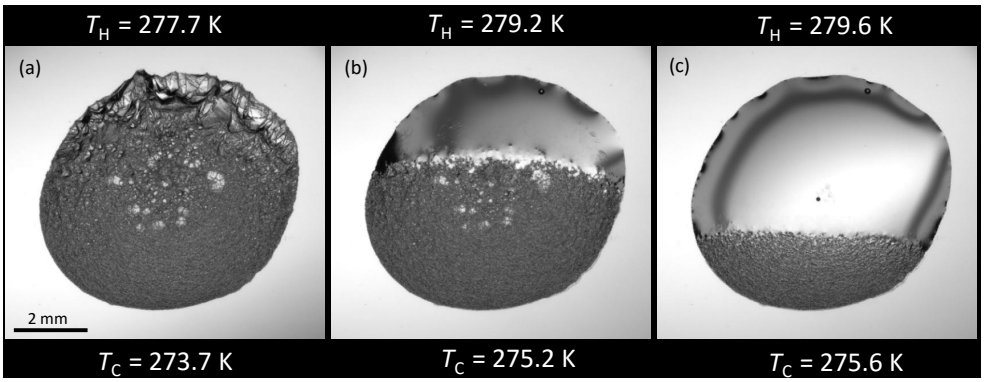

Figure 4.38 – Controlled dissociation sequence of a methane hydrate formed from pure water, with applied temperature gradient. $p = 4.0$ MPa, $T_{\mathrm{HLV}} = 277.5$ K. (a) Before hydrate dissociation. (b-c) The hydrate-water interface appears as a straight line marking the H-L-V temperature.

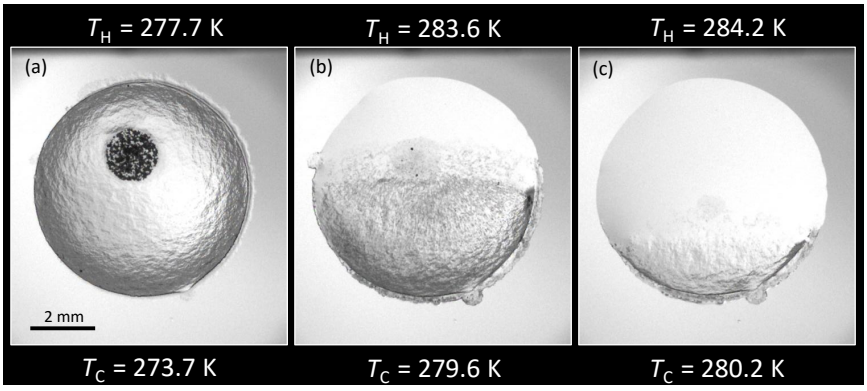

Figure 4.39 – Controlled dissociation sequence of a methane hydrate formed from an aqueous PVP solution, with applied temperature gradient. $w_{\mathrm{PVP}} = 0.1\%$, $p = 6.13$ MPa, $T_{\mathrm{HLV}} = 281.4$ K. (a) Before hydrate dissociation. (b-c) The hydrate-water interface appears as a straight line, hydrate crystals stable in the region above the equilibrium temperature.

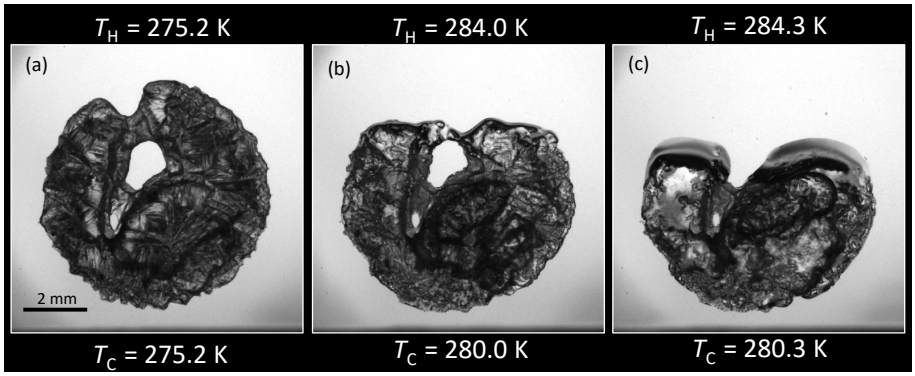

Figure 4.40 – Controlled dissociation sequence of a methane hydrate formed from an aqueous TBAB solution, with applied temperature gradient. w_{TBAB} = 0.5%, p = 6.87 MPa, T_{HLV} = 282.32 K. (a) Before hydrate dissociation. (b-c) Irregular hydrate-liquid phase interface, aqueous solution driven towards the hydrate phase.

4.2.3 Water + CH_4 + Tetra-n-butylammonium bromide (w_{TBAB} = 0.5%)

A dissociation sequence of methane hydrate formed from an aqueous solution containing a mass fraction of 0.5% TBAB, using a temperature gradient, at 6.87 MPa is shown in Figure 4.40. With each dissociation step the liquid phase was drawn towards the hydrate phase in the hydrate stable region (the region below the H-L-V temperature)(Figure 4.40 (b-c)). In Figure 4.40 (b), the liquid phase appeared to have been imbibed by the hydrate phase, while in Figure 4.40 (c), both liquid and hydrate phases are present. When the position of the H-L-V equilibrium temperature was close to the boundary of the hydrate, a small amount of liquid phase was present (Figure 4.40 (b)). The hydrate-liquid phase interface shown in Figure 4.40 (b-c) was stabilized in 5 h and an irregular interface was observed.

4.2.4 Water + CH_4 + ethylene glycol (w_{EG} = 10%)

Figure 4.41 shows a dissociation sequence of methane hydrate formed from an aqueous solution containing a mass fraction of 10% EG using a temperature gradient, at 5.99 MPa. The observed hydrate-liquid phase interface was not clear. In Figure 4.41 (b-c) it could be seen that hydrate dissociated towards the hot side of the gradient but also in several other regions on the slide. No

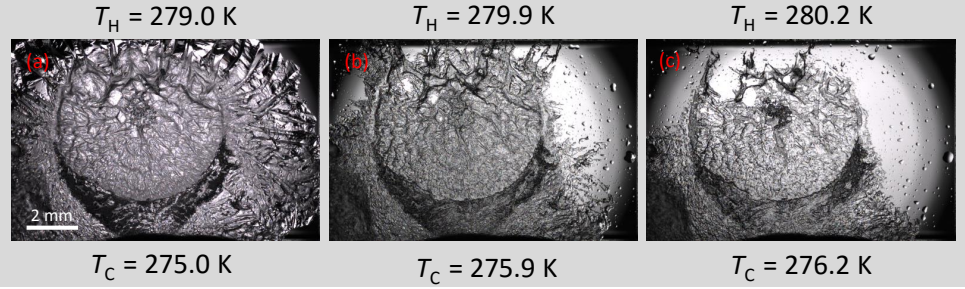

Figure 4.41 – Dissociation sequence of a methane hydrate formed from an aqueous EG solution, with applied temperature gradient. $w_{\mathrm{EG}} = 10\%$, $p = 5.99$ MPa, $T_{\mathrm{HLV}} = 279.7$ K. (a) Before hydrate dissociation. (b-c) Irregular pattern of hydrate dissociation.

clear pattern of hydrate dissociation was observed on the temperature gradient experiments. Therefore, hydrate dissociation for systems with EG was carried out using uniform surface temperature.

Figure 4.42 shows the sequence of hydrate dissociation using a uniform surface temperature, at 6.53 MPa. The hydrate dissociation with a uniform surface temperature is described in Section 3.3.3. Hydrate dissociation started from the boundary of the droplet around 0.6 K below the H-L-V equilibrium. As the temperature increased the dissociation continued towards the center of the droplet. The hydrate dissociation pattern followed the opposite path of its formation, Figure 4.6. Complete dissociation was observed at 280.6 K (Figure 4.42 (f)).

4.2.5 Water + CH_4 + sodium chloride ($w_{\mathrm{NaCl}} = 5.44\%$)

Figure 4.43 shows a dissociation sequence of methane hydrate formed from an aqueous solution containing a mass fraction of 5.44% NaCl using uniform surface temperature, at 5.39 MPa. Hydrate dissociation mainly started at the droplet boundary but lesser amounts of dissociation were also observed through the interior of the droplet. Hydrate started to dissociate around 1 K below the methane hydrate equilibrium temperature for the given aqueous NaCl solution. With increasing temperature, dissociation continued and eventually the complete hydrate dissociation was observed at 277.6 K.

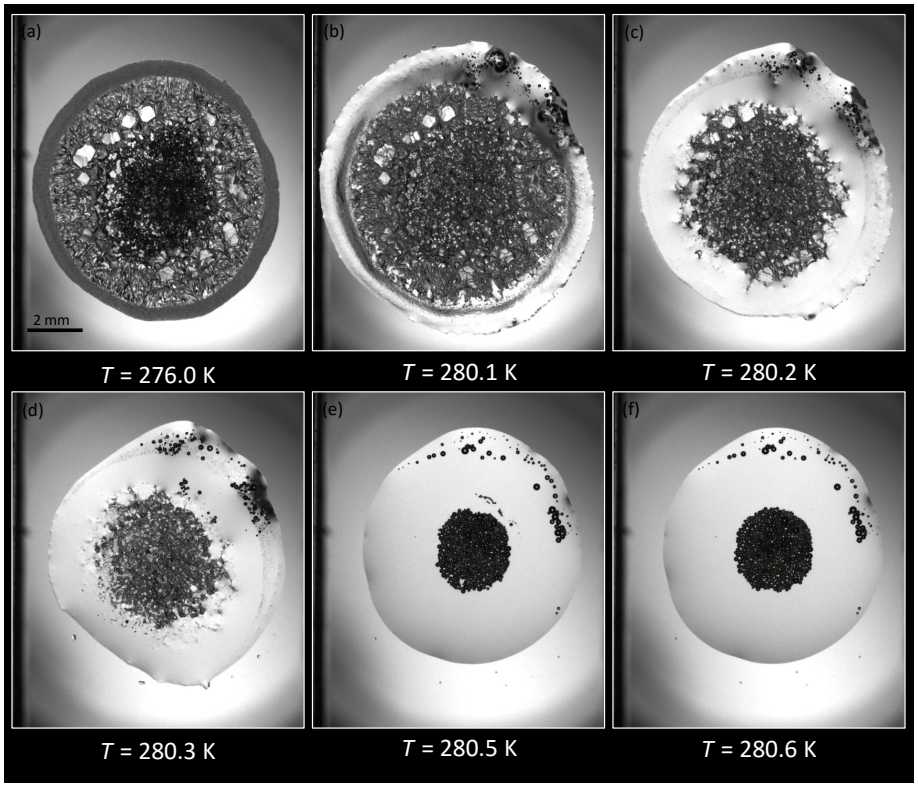

Figure 4.42 – Dissociation sequence of a methane hydrate formed from an aqueous EG solution, with uniform surface temperature. $w_{\mathrm{EG}} = 10\%$, $p = 6.53$ MPa, $T_{\mathrm{HLV}} = 280.5$ K. (a) Before hydrate dissociation. (b) Hydrate started to dissociate at the periphery of the droplet. (c-e) Continued dissociation towards the center of the droplet. (f) Complete hydrate dissociation.

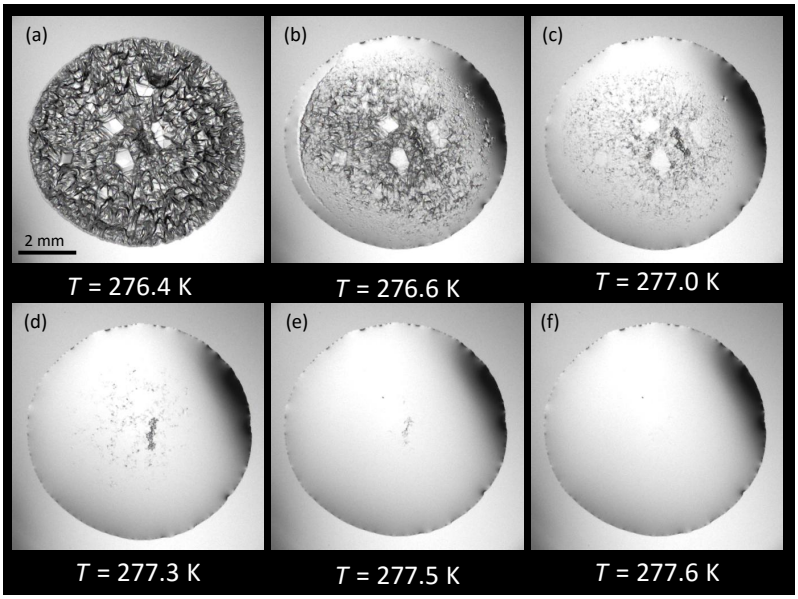

Figure 4.43 – Dissociation sequence of a methane hydrate formed from an aqueous NaCl solution, with uniform surface temperature. $w_{\mathrm{NaCl}} = 5.44\%$, $p = 5.39$ MPa, $T_{\mathrm{HLV}} = 277.6$ K. (a) Before hydrate dissociation. (b) The hydrate started to dissociate mainly at the periphery of the droplet. (c-e) Continued hydrate dissociation. (f) Complete hydrate dissociation.

4.3 Phase equilibria

The dissociation experiments were used to determine the equilibrium temperature at the system pressure for inhibited and uninhibited systems. For the systems: water + CH_4, water + PVP ($w_{\mathrm{PVP}} = 0.1\%$) + CH_4, and water + TBAB ($w_{\mathrm{TBAB}} = 0.5\%$ + CH_4) the equilibrium temperature was determined with using Equation (4.1).

$$T_{HLV} = gx_{I,i} + T_{C,i} \tag{4.1}$$

Where T_{HLV} is the hydrate-liquid-vapor equilibrium temperature, g is the temperature gradient, x_I is the position of the interface from the cold side of the stage and T_C is the temperature on the cold side of the gradient at step i. The gradient calculation is described in DuQuesnay *et al.* (2015).

For the systems: water + NaCl ($w_{\mathrm{NaCl}} = 5.44\%$) + CH_4, and water + EG ($w_{\mathrm{EG}} = 10\%$) + CH_4 the equilibrium temperature was determined by averaging the temperature at which the last hydrate crystal was observed and the temperature at which the complete hydrate dissociation was achieved. For example, for a system inhibited with NaCl, the equilibrium temperature was calculated by taking the average of temperatures corresponding to Figure 4.43 (e and f), at 5.39 MPa. Figure 4.42 illustrates H-L-V determination in the presence of ethylene glycol at 6.53 MPa, where the equilibrium temperature was taken as an average of temperatures corresponding to frames Figure 4.42 (e) and Figure 4.42 (f).

The results of phase equilibrium measurements for the dissociation data are summarized in Figure 4.44. The H-L-V values for the systems: water + CH_4, water + PVP ($w_{\mathrm{PVP}} = 0.1\%$) + CH_4, and water + TBAB ($w_{\mathrm{TBAB}} = 0.5\%$) + CH_4 fall within a 95% prediction interval, regressed from H-L-V data for the system water + CH_4 compiled by Sloan Jr and Koh (2007). The presence of either NaCl or EG shifted the hydrate equilibrium conditions to higher pressures and lower temperatures.

From a single formation experiment, gradient dissociation allowed multiple phase equilibrium data acquisition, whereas uniform surface temperature dissociation required complete dissociation and reformation for each replicate. Each marker on Figure 4.44 has an associated error bar corresponding to standard uncertainty. Some of the error bars are not visible because they are too small compared to the marker size. Standard uncertainty for H-L-V temperature was found to be less than 0.25 K, except for systems inhibited with

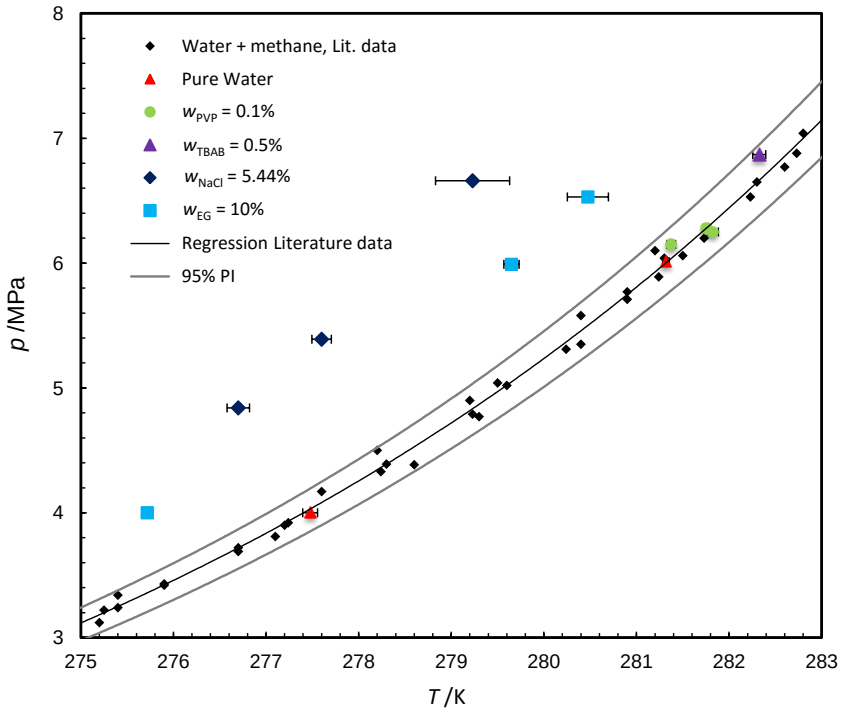

Figure 4.44 – Hydrate-liquid-vapor equilibrium for the system water + CH_4, water + PVP ($w_{PVP} = 0.1\%$) + CH_4, water + TBAB ($w_{TBAB} = 0.5\%$) + CH_4, water + NaCl ($w_{NaCl} = 5.44\%$) + CH_4, and water + EG ($w_{EG} = 10\%$) + CH_4. Error bars correspond to one standard deviation. Literature data compiled by Sloan Jr and Koh (2007) are also shown for water + CH_4. The black curve represents the best fit to literature data. The gray curves represent a 95% prediction interval for the literature data.

NaCl and EG at higher pressures, where standard deviation was in the order of 0.4 K.

Hydrate-liquid-vapor equilibrium data for the system water + EG ($w_{EG} = 10\%$) + CH_4 are shown in Figure 4.45. The measured HLV temperatures from this work are slightly higher ($\delta \leq 0.4$ K) than literature values, and CSMGem's prediction. The contrary occurred with the system water + NaCl ($w_{NaCl} = 5.44\%$) + CH_4, Figure 4.46, where this work's HLV temperatures were slightly lower than literature values and CSMGem's prediction.

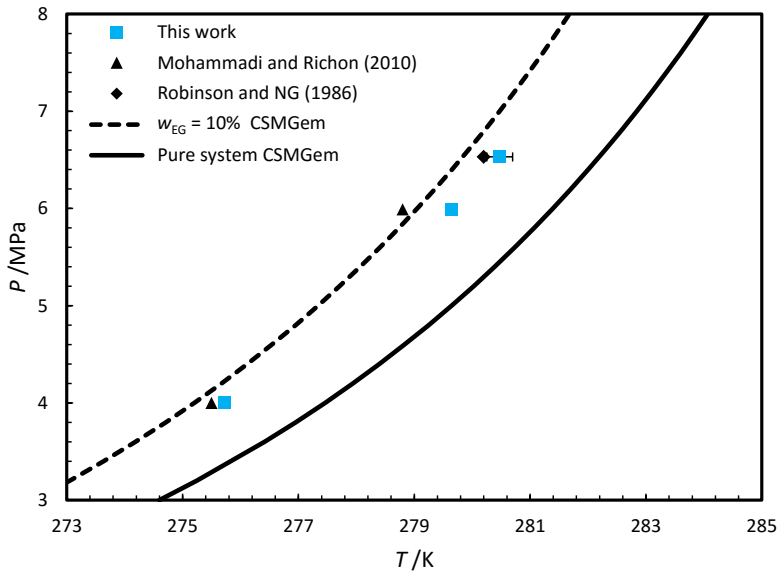

Figure 4.45 – Hydrate-liquid-vapor equilibrium for the system water + EG ($w_{\mathrm{EG}} = 10\%$) + CH_4. Error bars correspond to one standard deviation. Literature data are also shown (Mohammadi and Richon, 2010; Robinson, 1986; Sloan and Koh, 2007). Continuous lines show phase equilibrium modeling from CSMGem.

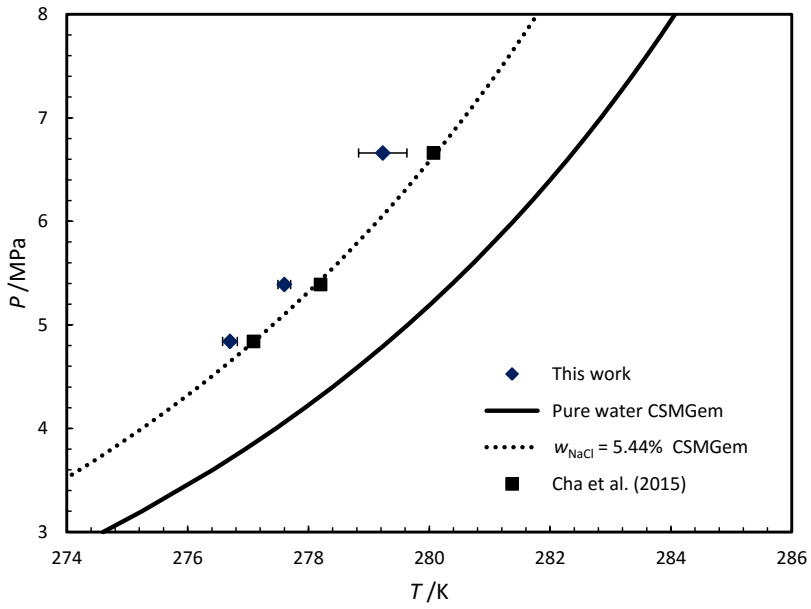

Figure 4.46 – Hydrate-liquid-vapor equilibria for the system water + NaCl ($w_{\mathrm{NaCl}} = 5.44\%$) + CH_4. Error bars correspond to one standard deviation. Literature data are also shown (Cha *et al.*, 2015; Sloan and Koh, 2007). Continuous lines show phase equilibrium modeling from CSMGem.

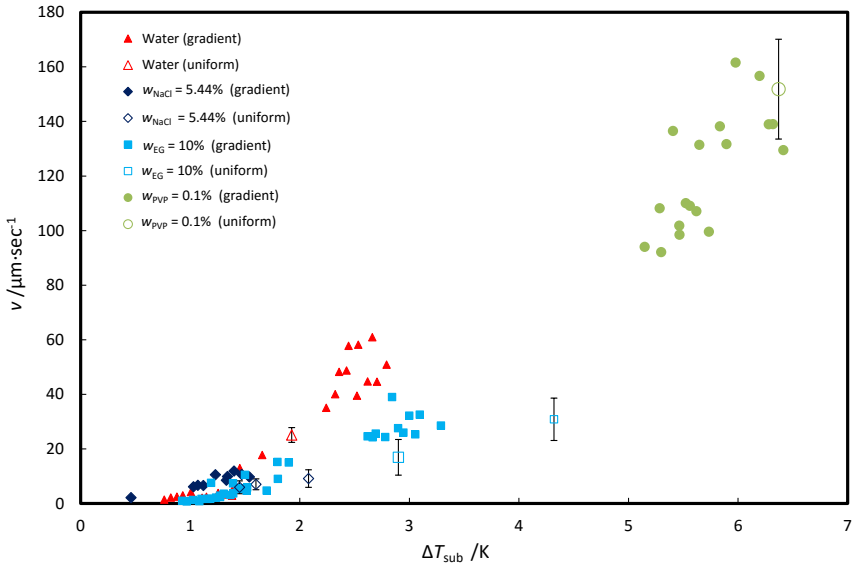

Figure 4.47 – Film velocity as a function of supercooling for methane hydrate formed on quiescent water droplets with and without inhibitors. Data for hydrates formed under uniform constant temperature and a constant temperature gradient are shown. Error bars correspond to one standard deviation.

4.4 Apparent kinetics

4.4.1 Hydrate film growth velocities

Methane hydrate film velocities were obtained by measuring the position of the growth front with respect to time. The instantaneous film velocity was approximated by the ratio of change in position of the interface to the time interval in which the change was observed (Equation (4.2)).

$$v_{f,i,i-1} = \frac{r_{f,i} - r_{f,i-1}}{t_i - t_{i-1}} \tag{4.2}$$

Where $v_{f,i,i-1}$ is the average hydrate film velocity from step $i-1$ to i, $r_{f,i} - r_{f,i-1}$ is the change in interface position in the direction of growth from step $i-1$ to i and $t_i - t_{i-1}$ is the elapsed time from step $i-1$ to i.

Figure 4.47 shows the relationship between film velocity and degree of subcooling (ΔT_{sub}) for inhibited and uninhibited systems. With increasing ΔT_{sub},

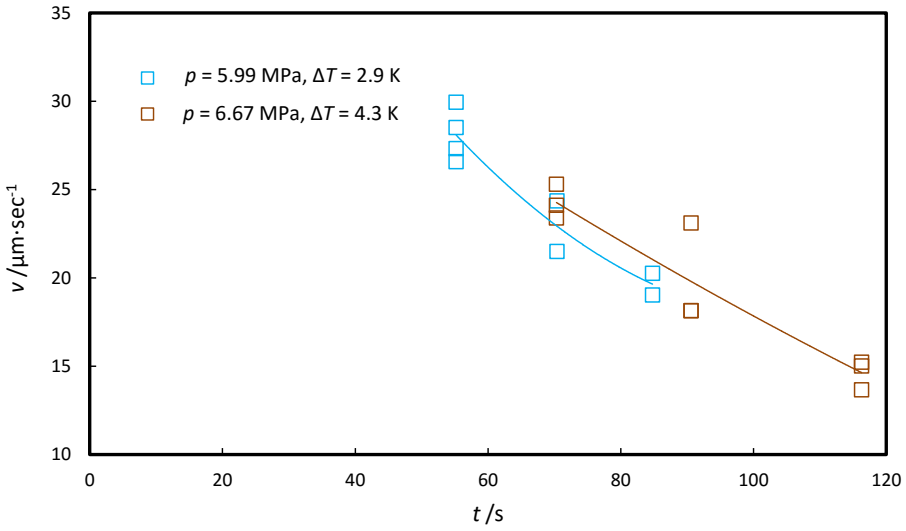

Figure 4.48 – Methane hydrate film velocity versus time for the system water + EG ($w_{\mathrm{EG}} = 10\%$) + CH_4 at uniform surface temperature. Continuous lines are drawn to increase the readability of the graph, but do not represent a modeling effort.

hydrate film velocity increased in all systems. Multiple measurements were taken for each experiment, as shown in Figure 4.47. A single gradient experiment allowed continuous measurement of velocities with respect to driving force, whereas a single velocity datum was obtained for a uniform temperature experiment. When $\Delta T_{\mathrm{sub}} < 2$ K, rates appeared to be almost confounded for systems with and without inhibitors. However, for $\Delta T_{\mathrm{sub}} \geq 2$ K it became evident that the addition of either sodium chloride or ethylene glycol reduced the growth velocity to approximately half that of the pure water system. Gradient data was found to have considerably more scatter than velocities obtained with a uniform temperature method. It was difficult to assess the effect of PVP, as velocities were obtained at a much higher driving force than with the pure system.

Film velocities were found to decrease with respect to time in systems with thermodynamic inhibitors subject to uniform constant temperatures. Figure 4.48 shows how film velocity decreased in water + EG ($w_{\mathrm{EG}} = 10\%$) + CH_4 system as time progressed, irrespective of the driving force used. The same holds true for the system water + NaCl ($w_{\mathrm{NaCl}} = 5.44\%$) + CH_4 (Figure 4.49).

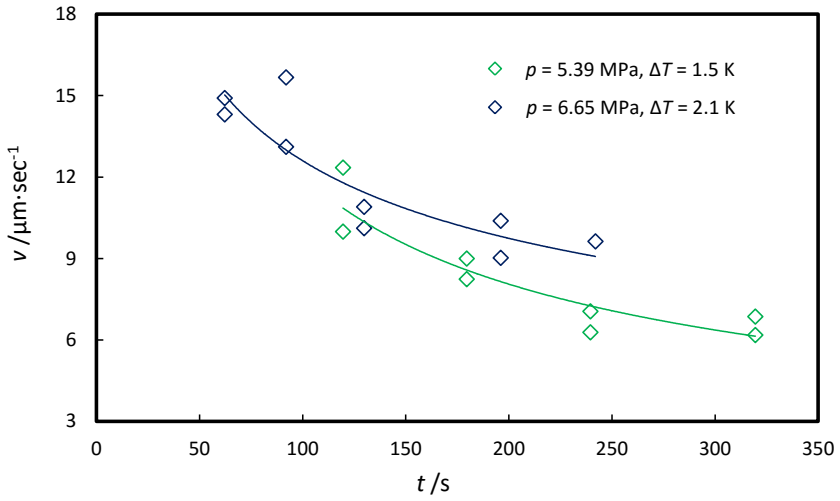

Figure 4.49 – Methane hydrate film velocity versus time for the system water + NaCl ($w_{\mathrm{NaCl}} = 5.44\%$) + CH_4, at uniform surface temperature. Continuous lines are drawn to increase the readability of the graph, but do not represent a modeling effort.

4.4.2 Hydrate halo growth

All of the systems studied in this work showed hydrate propagation onto the surface outside the original water boundary. Figure 4.1 shows halo formation for a pure water system; Figures 4.6, 4.9 and 4.10 show halos for systems with EG; Figures 4.12 and 4.16 to 4.18 for NaCl; Figures 4.19 to 4.22 for PVP; and Figures 4.32 and 4.34 to 4.36 for TBAB. As can be seen from these images, the crystal habit of the hydrate halo varied between pure and inhibited systems, and distinctly with each additive.

The pure system's halo was smooth (Figure 4.1) irrespective of driving force and temperature profile. The presence of EG produced a smooth crystal that propagated outside the original water boundary, but this halo changed abruptly to a faceted morphology (Figure 4.6) under uniform constant temperature. This abrupt change also occurred with EG droplets subject to a temperature gradient as the halo propagated toward the high driving force side (Figure 4.10). However, the EG halo on the low driving force side seemed to merge with the faceted crystal growing within the water droplet (Figure 4.10). Addition of NaCl produced a smooth halo for the most part (Figures 4.12 and 4.17), except at very low driving forces ($\Delta T_{\mathrm{sub}} \sim 0.5$ K)

where it seemed that the main crystal merged with the halo, both with faceted morphologies (Figure 4.17). For PVP droplets, the halo was almost translucent (Figure 4.21) and did not change with driving force or temperature profile (Figure 4.22)

Halo growth in the presence of TBAB was complicated and unpredictable. On one occasion, the halo seemed to grow rapidly (Figure 4.32 g to h) in a similar fashion to that of other inhibitors. On another instance, propagation outside of the original water boundary occurred from the main crystal growing at the periphery of the droplet and in a tri-dimensional fashion (Figure 4.35 g to h). On yet another occasion, halo growth was extremely slow and barely imperceptible (Figure 4.34).

Figure 4.50 shows the relationship between hydrate halo propagation rates and driving force (ΔT_{sub}) for pure water and inhibited systems. For the pure water system, the halo growth was observed in a few experiments and the propagation rate was measured to be approximately 8 μm·min^{-1} at ΔT_{sub} = 2 K. The halo propagation rate for the EG system appeared to increase dramatically with a small increase in subcooling; however, the scatter in the EG rates was considerable ($\delta = 100$ μm·min^{-1} at 4 K). For the system inhibited with TBAB, radically different halo growth rates were observed at the same ΔT_{sub}, ranging from 0.65 to 77 μm·min^{-1} at ΔT_{sub} = 7.1 K . For systems inhibited with NaCl, halo growth rates were observed to be on the same order of magnitude as that of the pure system, with the exception of two experiments where rates were above 20 μm·min^{-1}. Halo growth in the presence of PVP was observed to be < 20 μm·min^{-1} for 5.8 to 6.7 K ΔT_{sub}, and in the same order or magnitude of the pure system despite the fact that subcoolings were 5 K higher for the PVP system.

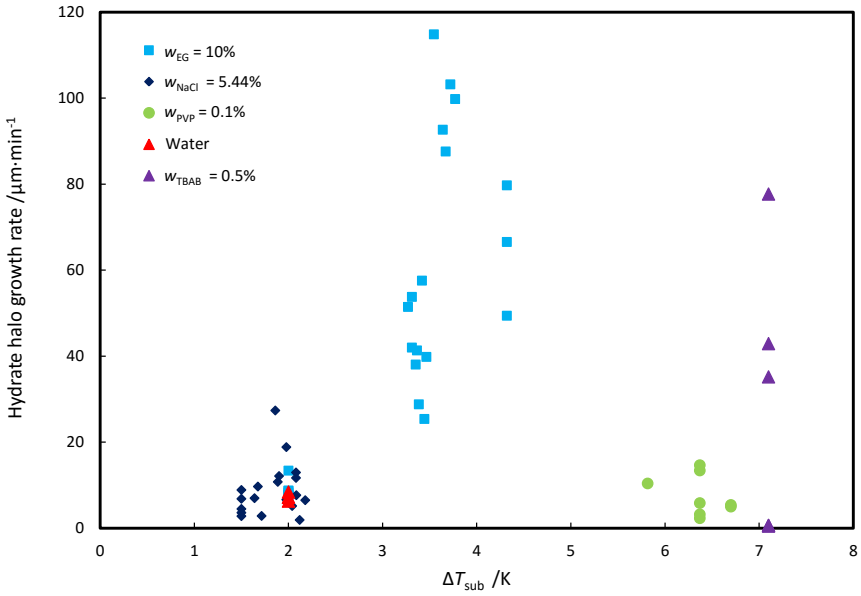

Figure 4.50 – Hydrate halo propagation velocity (outside of the original water boundary) versus subcooling. Data for pure water and in the presence of inhibitors are shown.

Chapter 5

Discussion

5.1 Morphology

5.1.1 Water + CH_4

Methane hydrate was formed from pure water using the same apparatus and the same driving forces as DuQuesnay *et al.* (2015). Methane hydrates formed in a pure system exhibited smooth granular morphology for $\Delta T_{\text{sub}} > 1.3$ K. The smoothness of the hydrate film increased with increasing driving force (Figure 4.4). This result is comparable with those reported in past studies (Beltran and Servio, 2010; Freer *et al.*, 2001; Li *et al.*, 2014; Servio and Englezos, 2003; Kitamura and Mori, 2013; Tanaka *et al.*, 2009).

Around $\Delta T_{\text{sub}} = 1.3$ K, a transition was observed in hydrate morphology from smooth tightly packed grains to large faceted or polygonal shape crystals (Figure 4.4). For $\Delta T_{\text{sub}} < 1.3$ K methane hydrates exhibited faceted morphology. A similar transition in hydrate morphology was observed by (Kitamura and Mori, 2013). This transition in hydrate film texture corresponds to the hydrate formation mechanism. The faceted morphology corresponds to step lateral crystal growth and the smooth tightly packed grain morphology corresponds to continuous growth. DuQuesnay *et al.* (2015) reported that for $\Delta T_{\text{sub}} > 1.3$ K continuous growth of the methane hydrate film occurred by secondary nucleation and attachment mechanism. For $\Delta T_{\text{sub}} > 1.3$ K the methane crystallization proceeded by continuous type 1 spherulitic (Gránásy *et al.*, 2005) growth (Figure 4.1).

The appearance of large single polyhedral crystals in the hydrate film (Fig-

ures 4.2 to 4.5) was not discussed in DuQuesnay *et al.* (2015). Li *et al.* (2014) reported similar single crystals in hydrate film for methane-ethane mixture hydrates. They hypothesized that these crystals originated from tiny crystals which were broken from the hydrate film. Smelik and King (1997) also reported the formation of single, translucent, methane hydrate crystals in the bulk liquid after complete coverage of the liquid-gas interface by hydrate film.

Initial growth points for large single crystals (Figure 4.3) were observed at the periphery of the droplet. These newly formed large crystals floated towards the center of the droplet, but did not attach to the main growth front initially. Instead, these almost translucent large crystals grew in the liquid phase ahead of the growth front. Perhaps the fact that these large single polyhedral crystals grew to a considerable size, can be seen as an indication of the absence of secondary nucleation that could disrupt their individual growth. Eventually these large crystals were incorporated to the growth front (Figure 4.3). Large crystals in the hydrate film exhibited single-crystal geometries corresponding to structure I, as reported by Smelik and King (1997).

5.1.2 Water + CH_4 + ethylene glycol ($w_{EG} = 10\%$)

Similar to the pure system, the morphology of methane hydrate formed from a mass fraction of 10% EG aqueous solution varied with the driving force. Methane hydrate with EG exhibited a uniform type 1 spherulitic morphology for $\Delta T_{sub} > 1.5$ K (Figures 4.6 to 4.11) and the hydrate film became smoother with increasing driving force. Similar to the pure system, around $\Delta T_{sub} = 1.5$ K, a transition in hydrate texture from uniform spherulitic morphology to large faceted or polygonal shaped crystals was observed. For $\Delta T_{sub} < 1.3$ K methane hydrate exhibited faceted morphology. The faceted crystal from the droplet propagated outside of the original water boundary (Figures 4.9 and 4.10). This might be due to an uninterrupted supply of aqueous solution through dark channels in hydrate film formed in the presence of EG. This faceted growth propagation outside the original water boundary was not observed with the pure system.

As observed for the pure system, the size of the hydrate crystals decreased with increasing ΔT_{sub} (Figures 4.8 to 4.11). In addition, the crystal size was bigger than that of simple methane hydrates at same degree of subcooling (Figures 4.4 and 4.10).

Dark channels were observed between grain boundaries across the hydrate

film. For the pure system, these channels were observed only at low driving forces (Figures 4.3 to 4.5). The change in crystal habit within the droplet is indicative of a change in growth mechanism in the presence of EG. It is possible that this change is due to reduced film growth velocities with EG (Figure 4.47). EG had a dramatic effect on halo propagation. Previous studies (Beltran and Servio, 2010; Esmail and Beltran, 2016) had reported smooth halos, but never the three-dimensional faceted habit exhibited here. The appearance of large single crystals in hydrate film was not affected by adding ethylene glycol.

5.1.3 Water + CH_4 + sodium chloride ($w_{NaCl} = 5.44\%$)

Methane hydrate formed in the presence of a mass fraction of 5.44% NaCl, exhibited a smooth granular hydrate morphology for $\Delta T_{sub} > 1.5$ K and faceted hydrate morphology below $\Delta T_{sub} < 0.7$ K (Figures 4.17 and 4.18). For $0.7 \leq \Delta T_{sub} \leq 1.5$ K a mixture of faceted and granular morphology was observed (Figure 4.17). Similar to the pure system, the size of the individual hydrate crystals decreased with increasing ΔT_{sub} (Figures 4.13 and 4.17).

A small increment in the size of individual hydrate crystals was observed as the hydrate film advanced away from the center of the droplet during uniform surface temperature experiments (Figures 4.14 and 4.15). This can be explained by the increase in NaCl concentration in the liquid phase caused by hydrate crystallization (Cha *et al.*, 2015; Lafond *et al.*, 2012). When the hydrate forms, NaCl is excluded from the hydrate phase. Thus, salt concentration is increased ahead of the growing front, as a result ΔT_{sub} was decreased (Nagashima *et al.*, 1999) and causes an increase in hydrate crystal size.

The same effect manifested somewhat differently for gradient experiments in the presence of NaCl, where a section of the aqueous solution droplet remained in the liquid state within the hydrate stable region (Figure 4.17). Furthermore, there was an unexpected change in crystal size towards the periphery of the droplet along an isotherm (red circles in Figure 4.16), which can also be attributed to the local change of ΔT_{sub}.

Compared at the same subcooling, hydrate crystals for the NaCl system were smaller than the hydrates formed with EG, yet larger than those of the pure system. In contrast, Sakemoto *et al.* (2009) observed that the morphology of cyclopentane hydrate with pure water and with NaCl solutions was qualitatively similar at the same ΔT_{sub}. Kishimoto *et al.* (2012) also showed that the morphology of the individual hydrate crystals was roughly similar at a given subcooling for any concentration of NaCl. It is possible that the tight

local temperature control of the apparatus used in this study allowed us to unmask the effect of adding NaCl to the system.

Similar to the hydrate formed from either pure water or in the presence of a mass fraction of 10% EG, the large single polyhedral crystals in the hydrate film were observed for the hydrate formed in the presence of a mass fraction of 5.44% NaCl. Thus, the presence of thermodynamic inhibitors did not appear to have an effect on large single crystal formation.

5.1.4 Water + CH_4 + polyvinylpyrrolidone ($w_{PVP} = 0.1\%$)

The hydrate film formed in the presence of a mass fraction of 0.1% PVP was very thin (based on translucency) and smooth (Figures 4.19 to 4.23) compared to hydrates formed from pure water or in the presence of EG, NaCl, or TBAB. This result is comparable with those reported in past studies for KHIs. Bruusgaard *et al.* (2009) observed that methane hydrate formed in the presence of poly(VP/VC) was thinner than the hydrate crust formed without inhibitors. Wu *et al.* (2013) reported a thinner hydrate formed from Luvicap + EG solution than that formed from water and a methane-propane mixed gas. Similar hydrate results were reported by Lee *et al.* (2014) for methane-propane clathrate in the presence of PVCap.

Clathrates formed from PVP aqueous solution exhibited spherulitic morphology composed of radiating micro beads (Figures 4.20 and 4.22). Surprisingly, no significant change in the size of individual hydrate crystals or the crystal habit was observed with increasing driving force.

The hydrate film formed with PVP appeared to thicken as time progressed. Addition of KHIs has been postulated to increase the porosity of the hydrate crust, thus allowing for guest transport and thickening of the clathrate (Sharifi and Englezos, 2014; Sharifi *et al.*, 2014b,a; Lee and Englezos, 2006; Kumar *et al.*, 2008; Cha *et al.*, 2013b).

5.1.5 Water + CH_4 + Tetra-n-butylammonium bromide ($w_{TBAB} = 0.5\%$)

At low pressure ($p = 4$ MPa)

For the system water + TBAB ($w_{TBAB} = 0.5\%$) + methane at $p = 4.0$ MPa, and the temperature from 273.7 to 277.7 K, individual, polygonal columnar

shaped crystals were formed on the surface of the droplet (Figures 4.24 to 4.28). The droplet surface was partially covered with these crystals. The number of crystals and their respective size decreased with decreasing driving force and increased with time. No hydrate growth was observed above 275.5 K at 4 MPa. The growth of individual hydrate crystals seemed to stop altogether around 10 h after of initial growth. There was no agglomeration observed. At this concentration the presence of TBAB in aqueous solution, worked as hydrate crystal growth inhibitor and antiagglomerant.

At high pressure (p = 6.6 MPa)

For the system water + TBAB (w_{TBAB} = 0.5%) + methane at p = 6.6 MPa, and temperatures from 273.7 to 277.7 K, the hydrate crust exhibited rugged and highly branched dendritic morphology (Figures 4.29 to 4.37). The formed hydrate crust in the presence of TBAB appeared to be thicker than the clathrate films of the pure system or the systems with THIs. Based on visual inspection under magnification, it appeared that most of the aqueous solution was converted to hydrate.

Crystal habit, growth mechanism and film velocity were unpredictable except for the fact that water seemed to be drawn towards the growing crystals. The results shown here suggest that pipeline plugging may progress rapidly and unpredictably under insufficient inhibition with TBAB.

5.2 Hydrate dissociation

Hydrates prepared from pure water or in the presence of low dosage hydrate inhibitors (PVP or TBAB), were dissociated by applying a temperature gradient across the sample (Section 3.3.3). Hydrates formed from the pure water dissociated at a faster rate compared to those in the presence of LDHIs. The hydrate-water interface stabilized within five minutes and there were no remnant crystals observed in the liquid phase (Figure 4.38).

Hydrates formed in the presence of either PVP and TBAB remained observable even after 5 h in the hydrate unstable region (Figures 4.39 and 4.40). Eventually these residual crystals in the liquid phase also dissociated. These results are comparable with those reported previously (Bruusgaard *et al.*, 2009). Sharifi *et al.* (2016); Daraboina *et al.* (2011b,c,a) and Makogon *et al.* (2000) have reported that hydrate formed in the presence of KHIs dissociated

at a higher temperature compared to the hydrate prepared in pure water, and multiple hydrate melting peaks were also observed.

In this study, even though the presence of PVP delayed the onset of dissociation, the H-L-V equilibrium temperature was found to be the same as for the pure system. Although PVP and TBAB inhibitors were found to inhibit hydrate growth they also seem to stabilize the hydrate, and as a result they inhibit hydrate dissociation. It is plausible that this delayed dissociation is due to binding of PVP and TBAB to the hydrate phase stabilize. The persistence of hydrates formed in the presence of PVP and TBAB, outside the hydrate stability zone, could have implications in flow assurance.

Hydrate formed in the presence of ethylene glycol dissociated irregularly with an applied temperature gradient (Figure 4.41). As discussed in Section 5.1.3, this could be due to a concentration gradient of inhibitor across the droplet. When uniform surface temperatures were used for dissociation, hydrate started to dissociate approximately 0.6 K below the expected H-L-V equilibrium temperature. Dissociation (Figure 4.42) followed the opposite path of hydrate formation (Figure 4.6).This might occur because when hydrate forms, the hydrate film advances from center to the periphery of the droplet. Therefore, the concentration of ethylene glycol increases towards the water droplet boundary which causes the dissociation at periphery first. Comparable results were observed for hydrate dissociation from systems containing NaCl (Figure 4.43). However, the NaCl system did not form gas bubbles upon dissociation. This might indicate that the presence of EG caused the excess methane to come out of solution, whereas NaCl had a stabilizing effect.

5.3 Phase equilibria

5.3.1 Pure system and system inhibited with LDHIs

The phase equilibrium results were obtained using controlled hydrate dissociation on a constant temperature gradient surface (described in DuQuesnay *et al.* (2015)) for low dose hydrate inhibitors and for the pure system are summarized in Figure 4.44. The measured H-L-V values for the systems water + CH_4, water + PVP (w_{PVP} = 0.1%) + CH_4, and water + TBAB (w_{TBAB} = 0.5%) + CH_4 agree within uncertainty with the regressed H-L-V data for system water + CH_4 compiled by Sloan Jr and Koh (2007). These results indicate that the presence of PVP and TBAB have no impact on methane hydrate phase equilibria at used concentrations.

5.3.2 Methane hydrate inhibited with THIs

The methane hydrate phase equilibrium results in the presence of THIs are summarized in Figure 4.45 and Figure 4.46. The CSMGem model prediction and the corresponding literature data are also shown in these figures. Both NaCl and ethylene glycol reduced the hydrate stability region because they decreased the water activity to an extent which reduces its ability to participate in hydrate formation. As a result lower temperature is required for hydrate formation at constant pressure. It can be observed that the experimentally measured data are precise (error bars corresponds to one standard deviation) and in good agreement (the maximum deviation ≤ 0.7 K) with the predicted data from CSMGem and comparable to those reported by Mohammadi and Richon (2010); Cha *et al.* (2015); Robinson (1986). However, the predicted data are steadily higher for NaCl and lower for EG than the experimentally measured data. The observed systematic deviation from the predicted data for EG is comparable to that reported by (Lafond *et al.*, 2012) for methane hydrate phase equilibrium data in the presence of a mass fraction of $\geq 10\%$ methanol. These results suggest that additional development in the model used in CSMGem may be needed to accurately capture hydrate equilibrium data in the presence of THIs.

5.4 Hydrate film velocities

The methane hydrate film growth rate on the surface of an aqueous solution droplet for the pure system and the systems inhibited with hydrate inhibitors are summarized in Figure 4.47. The growth rate mainly increases with increasing ΔT_{sub} in all the systems studied here.

For the system inhibited with either EG or NaCl, the hydrate film velocities appear to be comparable to those of the pure system when $\Delta T_{\text{sub}} < 2$ K. However, for $\Delta T_{\text{sub}} \geq 2$ K the presence of either EG or NaCl reduced the film velocities to approximately half that of the pure system. This result coincides qualitatively with those reported previously for CO_2 hydrate growth rate in the presence of salt (Uchida *et al.*, 2002; Peng *et al.*, 2009; Kishimoto *et al.*, 2012). Cha *et al.* (2013a) also reported a similar result for natural gas hydrate in the presence of EG.

In uniform surface temperature experiments with THIs, hydrate film velocities decreased as time progressed (Figures 4.48 and 4.49). Rejection of NaCl from the clathtrate crystal causes locally increased NaCl concentration ahead of

the growing front, reduced delta ΔT_{sub}, and ultimately local reduction in film velocity. The same effect occurred with system inhibited with ethylene glycol because EG was also excluded from the hydrate phase.

It was difficult to assess the effect of PVP on hydrate film velocity from our results, as velocities were obtained at much higher driving forces than with the pure system. However, the hydrate film velocities in the presence of PVP are lower than those reported by Kitamura and Mori (2013) for methane hydrate formed from pure water. Jensen *et al.* (2010) and Gordienko *et al.* (2010) reported on the intrinsic kinetics of methane and natural gas hydrate respectively with a mass fraction of 0.1% PVP. They both observed that the presence of PVP in aqueous solution showed reduced growth rates compared to that of the pure water system. Other researchers (Posteraro *et al.* (2015); Ivall *et al.* (2015); Daraboina *et al.* (2011a, 2013, 2011b,c); Lederhos *et al.* (1996); Sharifi and Englezos (2014) have reported that the presence of PVP decreased hydrate growth rates because the lactum rings of PVP are adsorbed on the hydrate crystals and sterically hinder the hydrate growth (Larsen *et al.*, 1998).

5.5 Propagation

All of the experiments (except hydrate formation from an aqueous solution containing 0.5% TBAB at 4 MPa) in this work showed hydrate propagation beyond the original aqueous solution droplet onto the sapphire surface. The crystal habit and growth rate of the hydrate halo varied between pure water and the inhibited systems, and distinctly with each additive.

Hydrate propagation outside the original droplet boundary has been shown to operate through water migration by capillary action, followed by hydrate formation (Esmail and Beltran, 2016). Mori and Mochizuki (1996, 1997) proposed a water capillary permeation model for the transport of water molecules in the formed hydrate layer, and later Davies *et al.* (2009) reported that the hydrate growth is controlled by the movement of water in the formed hydrate film. Austvik *et al.* (2000) also noted that polycrystalline gas hydrate films are generally porous. Therefore, it is plausible that the porous channels in the hydrate film could be the transport route for aqueous solution migration through the hydrate layer and to the sapphire surface.

The hydrate crust formed at low driving forces exhibited fewer channels than that of formed at high driving forces. As the channels are the porous routes

in hydrate film which are higher at high driving force because the hydrate forms smaller grains at high driving force as compared to low driving force. These channels consistently made contact with the sapphire surface at the periphery of the aqueous solution droplet. This might be the reason why more hydrate halo growth was observed towards the cold side than the hot side of the gradient experiments.

The porosity and permeability of the formed gas hydrate film varies between the pure and inhibited system, and noticeably with hydrate inhibitors. That could be the reason for the change in hydrate halo crystal habit and growth rates for the pure system and the inhibited systems. The pure system halo was smooth and did not change with the driving force. The dark channels that appeared in the hydrate film formed from an aqueous solution containing 10% EG were more distinguishable compared to those in the other systems studied in this work. As the hydrate grew, these channels could have allowed migration of more aqueous solution to the sapphire surface causing a change in halo crystal habit (Figures 4.9 and 4.10). Also with EG, the hydrate halo on the low driving force side seemed to merge with the faceted crystals growing within the water droplet. Perhaps this was also due to an uninterrupted supply of aqueous solution through dark channels. The NaCl system also showed that the main crystal merged with the halo when $\Delta T_{\text{sub}} < 0.5$ K (Figures 4.16 and 4.17); however, for $\Delta T_{\text{sub}} > 0.5$ K a smooth hydrate halo film developed. These results indicate that halo morphology is a product of a complex interaction between thermodynamic inhibitors and driving force, possibly due to the redistribution of solutes in the aqueous phase during hydrate formation.

The halo produced from the PVP aqueous solution was almost translucent irrespective of driving force and temperature profile (Figures 4.19 to 4.22). Propagation rates for PVP systems appeared to remain comparable to those of the pure water halo, even at higher driving forces (Figure 4.50). It is plausible to speculate that kinetic inhibitors do not affect halo morphology and propagation rates. More experiments with PVP would be required to confirm this.

Halo growth in the presence of TBAB was complicated and unpredictable between experiments carried out at the same temperatures and pressures (Figures 4.32 and 4.34 to 4.36). It is not clear what caused this erratic behavior.

Chapter 6

Conclusion

In this work the performance of hydrate inhibitors (EG, NaCl, PVP, and TBAB) on methane hydrate formation and decomposition was tested using a 3-in-1 approach to evaluate gas hydrate inhibitors. It successfully allowed to assess the effect of additives on hydrate morphology and growth rates with respect to temperature, and hydrate phase equilibrium temperature at experimental pressure. Methane hydrate formation was investigated on a constant temperature surface and constant temperature gradient surface experiments.

In morphology studies of the pure system and the systems inhibited with EG and NaCl separately, it was found that the size of individual hydrate crystals decreased with increasing subcooling. The occurrence of large single crystals in the hydrate film were observed in the pure system and the systems inhibited with EG and NaCl. For systems inhibited with PVP, no significant change in the size of individual hydrate crystals and crystal habit was observed within the ΔT_{sub} range $5.2 \leq \Delta T_{\text{sub}} \leq 6.8$ K. In the presence of TBAB, individual hydrate crystals were formed at low pressure ($p = 4$ MPa) and these hydrate crystals remained dispersed on the surface of the droplet. While at high pressure conditions ($p = 6.6$ MPa) massive hydrates were formed. Under insufficient inhibition with TBAB, the hydrate morphology and growth rate were unpredictable.

The presence of NaCl, EG and PVP significantly reduced the hydrate growth rate. During the methane hydrate growth process in the presence of THIs (NaCl, EG), it was found that the concentration of THIs in the liquid phase increased as a function of time.

All of the systems studied showed hydrate propagation onto the sapphire surface outside the original water boundary. The hydrate crystal growth behavior and the growth rate varied between pure and inhibited systems, and distinctly with each additive. It was hypothesized that the hydrate inhibitor may change the hydrate porosity which could facilitate the permeation of the aqueous solution through the hydrate layer. The latter may in turn explain the change of crystal habit of hydrate halos in the presence of THIs.

From the hydrate dissociation studies, it was found that the hydrates formed in the presence of PVP and TBAB were more stable than that of formed with pure water.

Overall, the obtained results were consistent and reproducible except the crystal growth behavior and growth rate for the system inhibited with TBAB at 6.6 MPa, and the temperature from 273.7 to 277.7 K. This technique should prove valuable especially in the analysis of potential inhibitors which are available in limited quantities.

6.1 Recommendations for future work

1. Hydrate formation in the presence of TBAB should be repeated with different concentrations and experimental conditions to find out the relationship between the degree of subcooling and the required TBAB concentration for inhibition of massive hydrate formation.

2. Hydrate formation in the presence of low dosage hydrate inhibitor should be repeated with saline solution because naturally occurring water typically contains dissolved salts, which have important applications in the prevention of hydrate formation in pipelines.

3. Hydrate formation in the presence of PVP should be repeated with different concentrations and experimental conditions to find out the governing reason and mechanism for catastrophic growth.

Bibliography

Anderson, B.J.; Tester, J.W.; Borghi, G.P. and Trout, B.L., 2005. Properties of inhibitors of methane hydrate formation via molecular dynamics simulations. *Journal of the American Chemical Society*, **127**: 17852–17862.

Austvik, T.; Li, X. and Gjertsen, L.H., 2000. Hydrate plug properties: Formation and removal of plugs. *Annals of the New York Academy of Sciences*, **912**: 294–303.

Beltran, J.G., 2009. *Equilibrium and morphology studies of clathrate hydrates*. Ph.D. thesis, McGill University.

Beltran, J.G. and Servio, P., 2010. Morphological Investigations of Methane-Hydrate Films Formed on a Glass Surface. *Crystal Growth & Design*, **10**: 4339–4347.

Bergeron, S.; Beltrán, J.G. and Servio, P., 2010. Reaction rate constant of methane clathrate formation. *Fuel*, **89**: 294–301.

Bishnoi, P.R., 2005. Gas Hydrate - My Personal Ecperinces and Challenges. In *Proceedings of the Fifth International Conference on Gas Hydrates*. pp. 1–18.

Bruusgaard, H.; Beltrán, J.G. and Servio, P., 2008. Vapor- liquid water- hydrate equilibrium data for the system N2+ CO2+ H2O. *Journal of Chemical & Engineering Data*, **53**: 2594–2597.

Bruusgaard, H.; Lessard, L.D. and Servio, P., 2009. Morphology study of structure I methane hydrate formation and decomposition of water droplets in the presence of biological and polymeric kinetic inhibitors. *Crystal Growth and Design*, **9**: 3014–3023.

Cha, M.; Hu, Y. and Sum, A.K., 2015. Methane hydrate phase equilibria for systems containing NaCl, KCl, and NH4 Cl. *Fluid Phase Equilibria*.

Cha, M.; Shin, K.; Kim, J.; Chang, D.; Seo, Y.; Lee, H. and Kang, S.P., 2013a. Thermodynamic and kinetic hydrate inhibition performance of aqueous ethylene glycol solutions for natural gas. *Chemical Engineering Science*, **99**: 184–190.

Cha, M.; Shin, K.; Seo, Y.; Shin, J.Y. and Kang, S.P., 2013b. Catastrophic growth of gas hydrates in the presence of kinetic hydrate inhibitors. *The Journal of Physical Chemistry A*, **117**: 13988–13995.

Chua, P.C. and Kelland, M.A., 2013. Study of the Gas Hydrate Anti-agglomerant Performance of a Series of n-Alkyl-tri (n-butyl) ammonium Bromides. *Energy & Fuels*, **27**: 1285–1292.

Chua, P.C.; Kelland, M.A. *et al.*, 2012. Tetra (iso-hexyl) ammonium bromide-the most powerful quaternary ammonium-based tetrahydrofuran crystal growth inhibitor and synergist with polyvinylcaprolactam kinetic gas hydrate inhibitor. *Energy & Fuels*, **26**: 1160–1168.

Daraboina, N.; Linga, P.; Ripmeester, J.; Walker, V.K. and Englezos, P., 2011a. Natural gas hydrate formation and decomposition in the presence of kinetic inhibitors. 2. Stirred reactor experiments. *Energy & Fuels*, **25**: 4384–4391.

Daraboina, N.; Moudrakovski, I.L.; Ripmeester, J.A.; Walker, V.K. and Englezos, P., 2013. Assessing the performance of commercial and biological gas hydrate inhibitors using nuclear magnetic resonance microscopy and a stirred autoclave. *Fuel*, **105**: 630–635.

Daraboina, N.; Ripmeester, J.; Walker, V.K. and Englezos, P., 2011b. Natural gas hydrate formation and decomposition in the presence of kinetic inhibitors. 1. High pressure calorimetry. *Energy & Fuels*, **25**: 4392–4397.

Daraboina, N.; Ripmeester, J.; Walker, V.K. and Englezos, P., 2011c. Natural gas hydrate formation and decomposition in the presence of kinetic inhibitors. 3. Structural and compositional changes. *Energy & Fuels*, **25**: 4398–4404.

Davenport, J.R.; Musa, O.M.; Paterson, M.J.; Piepenbrock, M.O.M.; Fucke, K. and Steed, J.W., 2011. A simple chemical model for clathrate hydrate inhibition by polyvinylcaprolactam. *Chem. Commun.*, **47**: 9891–9893.

Davies, S.R.; Lachance, J.W.; Sloan, E.D. and Koh, C.A., 2010. High-pressure differential scanning calorimetry measurements of the mass transfer resistance across a methane hydrate film as a function of time and subcooling. *Industrial & Engineering Chemistry Research*, **49**: 12319–12326.

Davies, S.R.; Sloan, E.D.; Sum, A.K. and Koh, C.A., 2009. In situ studies of the mass transfer mechanism across a methane hydrate film using high-resolution confocal Raman spectroscopy. *The Journal of Physical Chemistry C*, **114**: 1173–1180.

Del Villano, L. and Kelland, M.A., 2011. An investigation into the laboratory method for the evaluation of the performance of kinetic hydrate inhibitors using superheated gas hydrates. *Chemical Engineering Science*, **66**: 1973–1985.

DuQuesnay, J.R.; Posada, M.C.D. and Beltran, J.G., 2015. Novel gas hydrate reactor design: 3-in-1 assessment of phase equilibria, morphology and kinetics. *Fluid Phase Equilibria*.

Englezos, P.; Kalogerakis, N.; Dholabhai, P. and Bishnoi, P., 1987. Kinetics of formation of methane and ethane gas hydrates. *Chemical Engineering Science*, **42**: 2647–2658.

Englezos, P., 1993. Clathrate hydrates. *Industrial & Engineering Chemistry Research*, **32**: 1251–1274.

Esmail, S. and Beltran, J.G., 2016. Methane hydrate propagation on surfaces of varying wettability. *Journal of Natural Gas Science and Engineering*.

Florusse, L.J.; Peters, C.J.; Schoonman, J.; Hester, K.C.; Koh, C.A.; Dec, S.F.; Marsh, K.N. and Sloan, E.D., 2004. Stable low-pressure hydrogen clusters stored in a binary clathrate hydrate. *Science*, **306**: 469–471.

Freer, E.M.; Selim, M.S. and Sloan, E.D., 2001. Methane hydrate film growth kinetics. *Fluid Phase Equilibria*, **185**: 65–75.

Gordienko, R.; Ohno, H.; Singh, V.K.; Jia, Z.; Ripmeester, J.A. and Walker, V.K., 2010. Towards a green hydrate inhibitor: imaging antifreeze proteins on clathrates. *PLoS One*, **5**: e8953.

Gránásy, L.; Pusztai, T.; Tegze, G.; Warren, J.A. and Douglas, J.F., 2005. Growth and form of spherulites. *Physical Review E*, **72**: 011605.

Hashimoto, S.; Sugahara, T.; Moritoki, M.; Sato, H. and Ohgaki, K., 2008. Thermodynamic stability of hydrogen+ tetra-n-butyl ammonium bromide mixed gas hydrate in nonstoichiometric aqueous solutions. *Chemical Engineering Science*, **63**: 1092–1097.

Holder, G.D.; Corbin, G. and Papadopoulos, K.D., 1980. Thermodynamic and molecular properties of gas hydrates from mixtures containing methane, argon, and krypton. *Industrial and Engineering Chemistry Fundamentals*, **19**: 282–286.

Holder, G.D.; Zetts, S.P. and Pradhan, N., 1988. Phase behavior in systems containing clathrate hydrates. *Reviews in Chemical Engineering*, **5**: 1–70.

Huo, Z.; Freer, E.; Lamar, M.; Sannigrahi, B.; Knauss, D. and Sloan, E., 2001. Hydrate plug prevention by anti-agglomeration. *Chemical Engineering Science*, **56**: 4979–4991.

Ivall, J.; Pasieka, J.; Posteraro, D. and Servio, P., 2015. Profiling the Concentration of the Kinetic Inhibitor Polyvinylpyrrolidone throughout the Methane Hydrate Formation Process. *Energy & Fuels*, **29**: 2329–2335.

Jager, M.; Peters, C. and Sloan, E., 2002. Experimental determination of methane hydrate stability in methanol and electrolyte solutions. *Fluid Phase Equilibria*, **193**: 17–28.

Jensen, L.; Ramløv, H.; Thomsen, K. and von Solms, N., 2010. Inhibition of methane hydrate formation by ice-structuring proteins. *Industrial & Engineering Chemistry Research*, **49**: 1486–1492.

Kelland, M.A., 2006. History of the development of low dosage hydrate inhibitors. *Energy & Fuels*, **20**: 825–847.

Kelland, M.A.; Svartaas, T.M.; Øvsthus, J. and Namba, T., 2000. A new class of kinetic hydrate inhibitor. *Annals of the New York Academy of Sciences*, **912**: 281–293.

Kelland, M.A.; Svartaas, T.M.; Ovsthus, J.; Tomita, T. and Mizuta, K., 2006. Studies on some alkylamide surfactant gas hydrate antiagglomerants. *Chemical Engineering Science*, **61**: 4290–4298.

Kishimoto, M.; Iijima, S. and Ohmura, R., 2012. Crystal growth of clathrate hydrate at the interface between seawater and hydrophobic-guest liquid: effect of elevated salt concentration. *Industrial & Engineering Chemistry Research*, **51**: 5224–5229.

Kitamura, M. and Mori, Y.H., 2013. Clathrate-hydrate film growth along water/methane phase boundaries-an observational study. *Crystal Research and Technology*, **48**: 511–519.

Koh, C.A., 2002. Towards a fundamental understanding of natural gas hydrates. *Chemical Society Reviews*, **31**: 157–167.

Koh, C.A. and Sloan, E.D., 2007. Natural gas hydrates: Recent advances and challenges in energy and environmental applications. *AIChE journal*, **53**: 1636–1643.

Koh, C.A.; Sloan, E.D.; Sum, A.K. and Wu, D.T., 2011. Fundamentals and applications of gas hydrates. *Annual review of chemical and biomolecular engineering*, **2**: 237–257.

Kumar, R.; Lee, J.D.; Song, M. and Englezos, P., 2008. Kinetic inhibitor effects on methane/propane clathrate hydrate-crystal growth at the gas/water and water/n-heptane interfaces. *Journal of Crystal Growth*, **310**: 1154–1166.

Lafond, P.G.; Olcott, K.A.; Sloan, E.D.; Koh, C.A. and Sum, A.K., 2012. Measurements of methane hydrate equilibrium in systems inhibited with NaCl and methanol. *The Journal of Chemical Thermodynamics*, **48**: 1–6.

Larsen, R.; Knight, C.A. and Sloan, E.D., 1998. Clathrate hydrate growth and inhibition. *Fluid Phase Equilibria*, **150**: 353–360.

Lederhos, J.; Long, J.; Sum, A.; Christiansen, R. and Sloan, E., 1996. Effective kinetic inhibitors for natural gas hydrates. *Chemical Engineering Science*, **51**: 1221–1229.

Lee, J.D. and Englezos, P., 2006. Unusual kinetic inhibitor effects on gas hydrate formation. *Chemical Engineering Science*, **61**: 1368–1376.

Lee, S.Y.; Kim, H.C. and Lee, J.D., 2014. Morphology study of methane–propane clathrate hydrates on the bubble surface in the presence of SDS or PVCap. *Journal of Crystal Growth*, **402**: 249–259.

Li, S.L.; Sun, C.Y.; Liu, B.; Feng, X.J.; Li, F.G.; Chen, L.T. and Chen, G.J., 2013. Initial thickness measurements and insights into crystal growth of methane hydrate film. *AIChE Journal*, **59**: 2145–2154.

Li, S.L.; Sun, C.Y.; Liu, B.; Li, Z.Y.; Chen, G.J. and Sum, A.K., 2014. New Observations and Insights into the Morphology and Growth Kinetics of Hydrate Films. *Scientific reports*, **4**.

Li, S.L.; Wang, Y.F.; Sun, C.Y.; Chen, G.J.; Liu, B.; Li, Z.Y. and Ma, Q.L., 2015. Factors controlling hydrate film growth at water/oil interfaces. *Chemical Engineering Science*.

Luna-Ortiz, E.; Healey, M.; Anderson, R. and Sørhaug, E., 2014. Crystal Growth Inhibition Studies for the Qualification of a Kinetic Hydrate Inhibitor under Flowing and Shut-In Conditions. *Energy & Fuels*, **28**: 2902–2913.

Makogon, Y.; Holditch, S. and Makogon, T., 2007. Natural gas-hydrates A potential energy source for the twenty firstst Century. *Journal of Petroleum Science and Engineering*, **56**: 14–31.

Makogon, Y.; Makogon, T. and Holditch, S., 2000. Kinetics and mechanisms of gas hydrate formation and dissociation with inhibitors. *Annals of the New York Academy of Sciences*, **912**: 777–796.

Makogon, Y.F., 2010. Natural gas hydrates–A promising source of energy. *Journal of Natural Gas Science and Engineering*, **2**: 49–59.

Mochizuki, T. and Mori, Y.H., 2006. Clathrate-hydrate film growth along water/hydrate-former phase boundaries-numerical heat-transfer study. *Journal of Crystal Growth*, **290**: 642–652.

Mohammadi, A.H. and Richon, D., 2009a. Methane hydrate phase equilibrium in the presence of salt (NaCl, KCl, or CaCl 2)+ ethylene glycol or salt (NaCl, KCl, or CaCl 2)+ methanol aqueous solution: Experimental determination of dissociation condition. *The Journal of Chemical Thermodynamics*, **41**: 1374–1377.

Mohammadi, A.H. and Richon, D., 2009b. Phase equilibria of methane hydrates in the presence of methanol and/or ethylene glycol aqueous solutions. *Industrial & Engineering Chemistry Research*, **49**: 925–928.

Mohammadi, A.H. and Richon, D., 2010. Gas hydrate phase equilibrium in the presence of ethylene glycol or methanol aqueous solution. *Industrial & Engineering Chemistry Research*, **49**: 8865–8869.

Mori, Y. and Mochizuki, T., 1996. Modeling of Mass Transport across a Hydrate Layer Intervening between Liquid Water and Guest Fluid Phases. In *2nd International Symposium on Gas Hydrates*. pp. 267–274.

Mori, Y.H. and Mochizuki, T., 1997. Mass transport across clathrate hydrate films a capillary permeation model. *Chemical Engineering Science*, **52**: 3613–3616.

Mullin, J., 1961. Crystallization, 1961. *Butterworths*, **1**: 92–93.

Nagashima, K.; Yamamoto, Y.; Komai, T.; HOSHINO, H. and OHGA, K., 1999. Interferometric Observation of Salt Concentration Distribution in Liquid Phase Around THF Clathrate Hydrate During Directional Growth. *The Japan Institute of Energy*, **78**: 325–331.

Østergaard, K.K.; Masoudi, R.; Tohidi, B.; Danesh, A. and Todd, A.C., 2005. A general correlation for predicting the suppression of hydrate dissociation temperature in the presence of thermodynamic inhibitors. *Journal of Petroleum Science and Engineering*, **48**: 70–80.

Ota, M.; Saito, T.; Aida, T.; Watanabe, M.; Sato, Y.; Smith, R.L. and Inomata, H., 2007. Macro and microscopic CH4–CO2 replacement in CH4 hydrate under pressurized CO2. *AIChE Journal*, **53**: 2715–2721.

Peng, B.; Sun, C.; Chen, G.; Yang, L.; Zhou, W. and Pang, W., 2009. Hydrate film growth at the interface between gaseous CO2 and sodium chloride solution. *Science in China Series B: Chemistry*, **52**: 676–682.

Peng, B.; Dandekar, A.; Sun, C.; Luo, H.; Ma, Q.; Pang, W. and Chen, G., 2007. Hydrate film growth on the surface of a gas bubble suspended in water. *The Journal of Physical Chemistry B*, **111**: 12485–12493.

Perfeldt, C.M.; Chua, P.C.; Daraboina, N.; Friis, D.; Kristiansen, E.; Ramløv, H.; Woodley, J.M.; Kelland, M.A. and von Solms, N., 2014. Inhibition of Gas Hydrate Nucleation and Growth: Efficacy of an Antifreeze Protein from the longhorn beetle Rhagium mordax. *Energy & Fuels*, **28**: 3666–3672.

Posteraro, D.; Ivall, J.; Maric, M. and Servio, P., 2015. New insights into the effect of polyvinylpyrrolidone (PVP) concentration on methane hydrate growth. 2. Liquid phase methane mole fraction. *Chemical Engineering Science*, **126**: 91–98.

Robinson, D. B.; Ng, H.J.J., 1986. *Can. Pet. Tech.*, **25**: 26. Quoted in (Sloan and Koh, 2007).

Sabase, Y. and Nagashima, K., 2009. Growth mode transition of tetrahydrofuran clathrate hydrates in the guest/host concentration boundary layer. *The Journal of Physical Chemistry B*, **113**: 15304–15311.

Sakemoto, R.; Sakamoto, H.; Shiraiwa, K.; Ohmura, R. and Uchida, T., 2009. Clathrate hydrate crystal growth at the seawater/hydrophobic- guest- liquid interface. *Crystal Growth & Design*, **10**: 1296–1300.

Sangwai, J.S. and Oellrich, L., 2014. Phase equilibrium of semiclathrate hydrates of methane in aqueous solutions of tetra-n-butyl ammonium bromide (TBAB) and TBAB–NaCl. *Fluid Phase Equilibria*, **367**: 95–102.

Servio, P. and Englezos, P., 2003. Morphology of methane and carbon dioxide hydrates formed from water droplets. *AIChE journal*, **49**: 269–276.

Sharifi, H. and Englezos, P., 2014. Accelerated Hydrate Crystal Growth in the Presence of Low Dosage Additives Known as Kinetic Hydrate Inhibitors. *Journal of Chemical & Engineering Data*, **60**: 336–342.

Sharifi, H.; Ripmeester, J. and Englezos, P., 2016. Recalcitrance of gas hydrate crystals formed in the presence of kinetic hydrate inhibitors. *Journal of Natural Gas Science and Engineering*.

Sharifi, H.; Ripmeester, J.; Walker, V.K. and Englezos, P., 2014a. Kinetic inhibition of natural gas hydrates in saline solutions and heptane. *Fuel*, **117**: 109–117.

Sharifi, H.; Walker, V.K.; Ripmeester, J. and Englezos, P., 2014b. Insights into the behavior of biological clathrate hydrate inhibitors in aqueous saline solutions. *Crystal Growth & Design*, **14**: 2923–2930.

Sloan, E.D., 2003. Fundamental principles and applications of natural gas hydrates. *Nature*, **426**: 353–363.

Sloan, E.D.; Koh, C.A. and Sum, A., 2010. *Natural gas hydrates in flow assurance*. Gulf Professional Publishing.

Sloan, E. and Koh, C., 2007. CSMGem a phase-equilibrium calculation program package accompanying the following book. In *Clathrate Hydrates of Natural Gases*. CRC Press Florida.

Sloan Jr, E.D. and Koh, C., 2007. *Clathrate hydrates of natural gases*. CRC press.

Smelik, E.A. and King, H., 1997. Crystal-growth studies of natural gas clathrate hydrates using a pressurized optical cell. *American Mineralogist*, **82**: 88–98.

Sum, A.K.; Koh, C.A. and Sloan, E.D., 2009. Clathrate hydrates: from laboratory science to engineering practice. *Industrial & Engineering Chemistry Research*, **48**: 7457–7465.

Sun, C.; Peng, B.; Dandekar, A.; Ma, Q. and Chen, G., 2010. Studies on hydrate film growth. *Annual Reports Section" C"(Physical Chemistry)*, **106**: 77–100.

Tanaka, R.; Sakemoto, R. and Ohmura, R., 2009. Crystal growth of clathrate hydrates formed at the interface of liquid water and gaseous methane, ethane, or propane: variations in crystal morphology. *Crystal Growth and Design*, **9**: 2529–2536.

Taylor, C.J.; Miller, K.T.; Koh, C.A. and Sloan Jr, E.D., 2007. Macroscopic investigation of hydrate film growth at the hydrocarbon/water interface. *Chemical Engineering Science*, **62**: 6524–6533.

Tohidi, B.; Anderson, R.; Mozaffar, H. and Tohidi, F., 2015. The return of kinetic hydrate inhibitors. *Energy & Fuels*, **29**: 8254–8260.

Uchida, T.; Ikeda, I.Y.; Takeya, S.; Ebinuma, T.; Nagao, J. and Narita, H., 2002. CO 2 hydrate film formation at the boundary between CO 2 and water: effects of temperature, pressure and additives on the formation rate. *Journal of crystal growth*, **237**: 383–387.

Urdahl, O.; Lund, A.; Mørk, P. and Nilsen, T.N., 1995. Inhibition of gas hydrate formation by means of chemical additivesI. Development of an experimental set-up for characterization of gas hydrate inhibitor efficiency with respect to flow properties and deposition. *Chemical engineering science*, **50**: 863–870.

Van der Waals, J. and Platteeuw, J., 1959. Clathrate solutions. *Advances in Chemical Physics, Volume 2*: 1–57.

Walker, V.K.; Zeng, H.; Ohno, H.; Daraboina, N.; Sharifi, H.; Bagherzadeh, S.A.; Alavi, S. and Englezos, P., 2015. Antifreeze proteins as gas hydrate inhibitors. *Canadian Journal of Chemistry*, **93**: 839–849.

Wu, R.; Aman, Z.M.; May, E.F.; Kozielski, K.A.; Hartley, P.G.; Maeda, N. and Sum, A.K., 2014. The Effect of a Kinetic Hydrate Inhibitor PVCap on Cyclopentane Hydrate Cohesion Forces and Growth. *Energy & Fuels*.

Wu, R.; Kozielski, K.A.; Hartley, P.G.; May, E.F.; Boxall, J. and Maeda, N., 2013. Methane–propane mixed gas hydrate film growth on the surface of water and Luvicap EG solutions. *Energy & Fuels*, **27**: 2548–2554.

Zerpa, L.E.; Salager, J.L.; Koh, C.A.; Sloan, E.D. and Sum, A.K., 2010. Surface chemistry and gas hydrates in flow assurance. *Industrial & Engineering Chemistry Research*, **50**: 188–197.

Zerpa, L.E.; Sloan, E.D.; Sum, A.K. and Koh, C.A., 2012. Overview of CSMHyK: A transient hydrate formation model. *Journal of Petroleum Science and Engineering*, **98**: 122–129.